Appendix A. Calculation of the wave resistance by CFD

This Appendix presents the wave resistance calculations used in the analysis of the resistance experiments described in Chapter 3. This calculation was performed with a CFD tool called *SHIPFLOW*, which is introduced in Section A.1. Section A.2 contains the calculations for the three sets of resistance experiments.

A.1 A short introduction to the CFD tool SHIPFLOW

The flow around a body can be described mathematically as a function of fluid pressure and the three components of velocity. A set of governing equations of motions can be created, like the Navier-Stokes equations for turbulent flow, and solved in association with specific boundary conditions. These equations are often complex to solve and rely on the use of Computational Fluid Dynamics (CFD). SHIPFLOW is a CFD tool specifically developed to solve marine related problems (SHIPFLOW, 1999).

To investigate the flow around a ship or ship model, SHIPFLOW splits the flow into three regions, shown in Figure A.1; the region of potential flow, which neglects viscous effects and is associated with the wavemaking pattern, the region of boundary-layer flow and the region where the complete Navier-Stokes equations are solved.

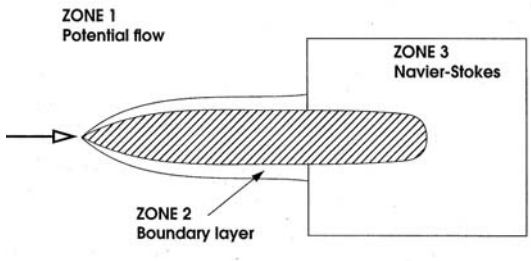

Figure A.1. The different flow regions assumed by SHIPFLOW (From SHIPFLOW, 1999)

The following potential flow techniques are used in Zone 1 to predict pressures, velocities and streamlines. By assuming non-viscous (ideal) and irrotational flow the governing equations produced are the linear, partial differential Laplace equations based on mass continuity. The non-linear free-surface boundary conditions are linearised and solved by using an iterative process until satisfactory convergence is reached.

In Zone 2 the development of the boundary layer is investigated using momentum integral equations for the thin viscous layer along the hull. By ignoring cross flow in the boundary layer, which is created due to a pressure gradient in the vertical direction of the ship hull the results are ordinary differential equations which are solved by Runge-Kutta techniques. This prediction cannot be used at the stern of a ship where a thick viscous region occurs due to convergence of the streamlines.

Towards the stern of the vessel, Reynolds-averaged Navier-Stokes (RANS) equations along with mass continuity equations describe the flow in Zone 3. The solution of the complex Navier-Stokes equations requires a lot of computational time and is therefore restricted to the stern of the vessel only, where a denser panelisation is created. The unsteadiness of the turbulent region is averaged out and instantaneous values of pressure and velocity are separated into a mean with fluctuations by the introduction of Reynolds stresses. In order to solve the closure problem (cf. Chapter 4), the turbulent flow a κ-ε model is used in which the kinetic energy, κ and the rate of dissipation, ε are modelled.

SHIPFLOW uses the zonal approach in order to reduce computational time. The programming is split into six modules and SHIPFLOW considers each module at a time. The method is unidirectional, in other words the results of the last module do not affect, for example, the second module. These six modules are listed below, in the order in which SHIPFLOW assesses them.

XFLOW

Defines the general physical properties of the surroundings, for example the fluid, characteristics, initial ship position, ship speed, etc..

XMESH

Using the information from XFLOW, XMESH generates the panelisation of the free surface and the vessel for use by the third module XPAN. The model can be viewed in the post processor.

XPAN

XPAN computes the potential flow around the model (i.e. Zone 1) and free-surface, which are made up of quadrilateral panels each containing Rankine sources. XPAN can operate under linear or non-linear free-surface boundary conditions. Results obtained from XPAN are displayed by the post processor and listed in output files. The results include

wavemaking coefficient (C_W), wave pattern, potential streamlines, pressure and velocity contours.

XBOUND

XBOUND is concerned with the thin turbulent boundary layer surrounding the hull (i.e. Zone 2). Using momentum integral equations SHIPFLOW provides the frictional resistance coefficient (C_F), boundary layer thickness δ, as well as other parameters associated with the boundary layer.

XGRID

XGRID generates the grid towards the stern of the vessel used to represent Zone 3 where the Navier-Stokes equations describe the fluid flow.

XVISC

The final module of SHIPFLOW solves the Reynolds-averaged Navier-Stokes equations. XVISC provides the viscous pressure resistance coefficient (C_{VP}) and therefore the total resistance C_T can be estimated. XVISC can also be used to investigate the wake and values such as axial, radial and tangential velocities at various planes towards the stern are obtained.

A.2 Calculation of the frictional resistance of the models used in the resistance experiments using the CFD program SHIPFLOW

A.2.1 The 2.55m long plate

The 2.55m long plate was the first model to be calculated with SHIPFLOW within the Department of Marine Technology at the University of Newcastle-upon-Tyne. It was used as a case-study for panel optimisation and several mesh configurations were studied in order to find the best results.

The computations of C_W were checked against a semi-numerical calculation carried out by the Author using Haskind's best-known form of Michell's integral and an alternative numerical computation of Michell's integral using a source-distribution method, which was carried out by Prof. Gören at Istanbul Technical University.

It was found that the linear computation method of SHIPFLOW gave better agreement with the numerical computation of Michell's integral, than the non-linear computation method, which is expected since Michell's integral is linear. It was also found that a higher number of panels also gave better agreement, and the best panelisations generated by SHIPFLOW matched on average with the numerical calculations of Michell's integral within 0.5%. Figure A.2 depicts the wave resistance coefficients versus Froude number for different panelisations and computation methods. More information regarding the computations and details of the different panelisations shown in Figure A.2, is given in Candries et al. (1998).

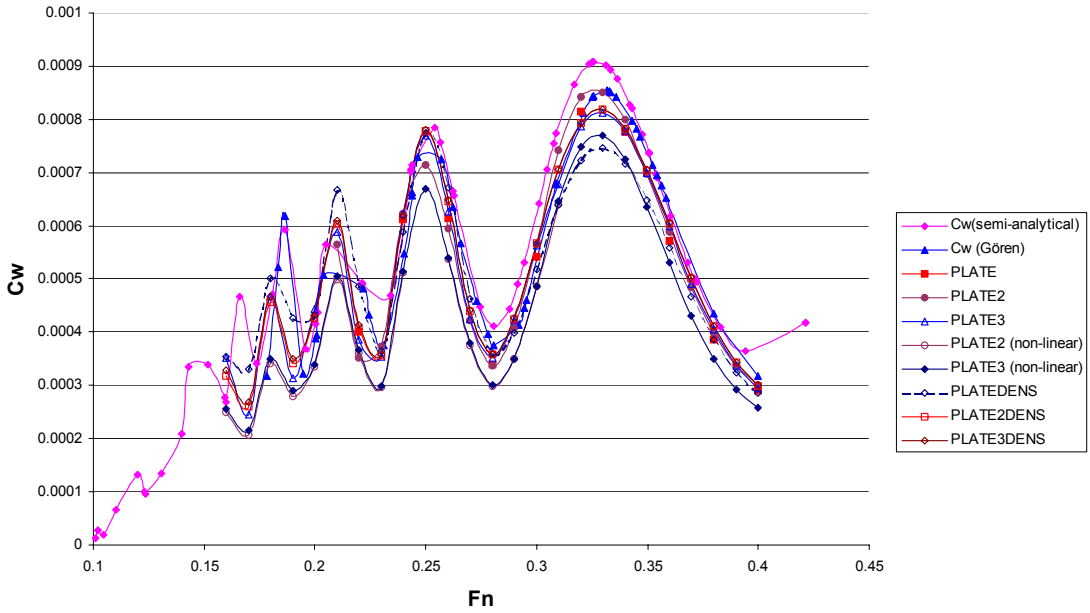

Figure A.2. Wave resistance coefficients as calculated by different methods versus Froude number.

A.2.2 The 6.3m long plate

The software SHIPFLOW was used to complement the physical experiments described in Section 3.4 with three objectives in mind: firstly, to obtain a prediction of the wave resistance, secondly to establish how well the computed total resistance of the smooth aluminium surface agreed with the measured data, and thirdly, to compare the computed wave elevations with the wave elevation readings from the video recordings.

Table A-1 presents the geometrical particulars, non-dimensionalised by the length, of the actual plate and the mesh generated by the CFD code, and demonstrates very good agreement.

Table A-1. Geometrical particulars of the physical plate and the CFD mesh

	T = 1m	T = 1.2m	CFD, T = 1m	CFD, T =1.2m
B	0.026984	0.026984	0.026984	0.026984
T	0.158730	0.190476	0.158729	0.190475
WPA	0.019485	0.019485	0.019472	0.019472
S	0.337054	0.399446	0.317641	0.381171
∇	0.003093	0.003711	0.003093	0.003711

Figure A.3 shows the frictional, wave and total resistance coefficients as computed by SHIPFLOW, together with the total resistance as measured from the experiments and the Schoenherr and ITTC ship-model correlation lines. The well-known equations for the ITTC and Schoenherr lines are respectively:

$$C_F = 0.075/(\log(Re)-2)^2$$

$$0.242/C_F^{0.5} = \log(ReC_F)$$

Figure A.3 shows that there is excellent agreement between the computed frictional resistance of the plate and the Schoenherr line. Moreover, the total resistance computed by the CFD code agrees excellently with the total resistance measured from the experiments.

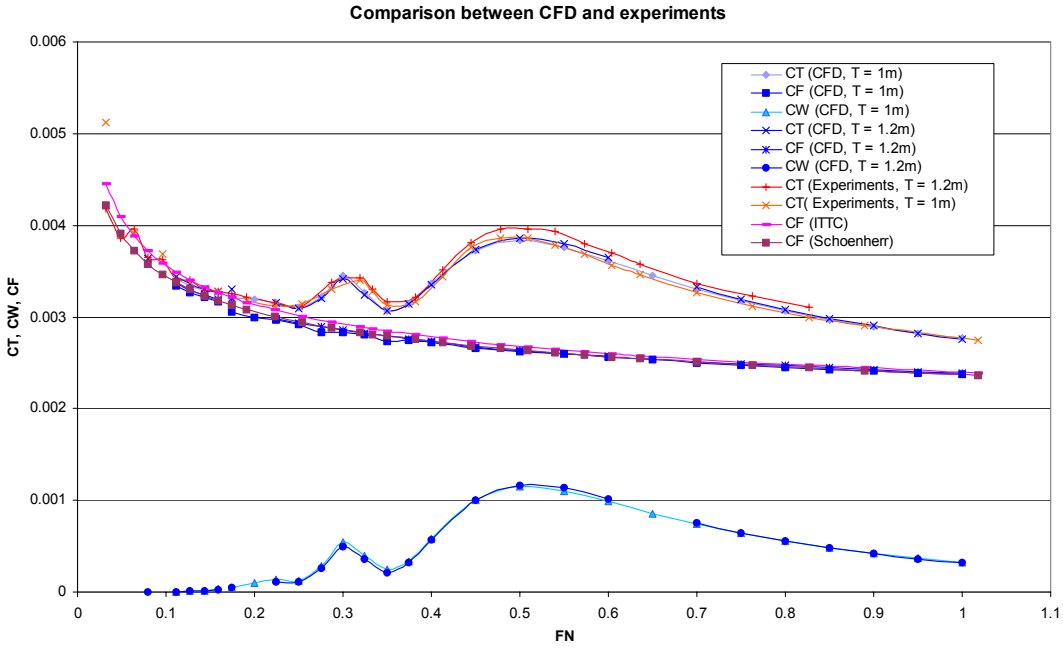

Figure A.3. Comparison of the resistance between the experiments and the CFD computations.

During the experiments, the wave profiles at different speeds were captured by a video camera attached to the carriage. A number of sample profiles at four different Froude Numbers as measured from the video recordings is shown in Figure A.4.

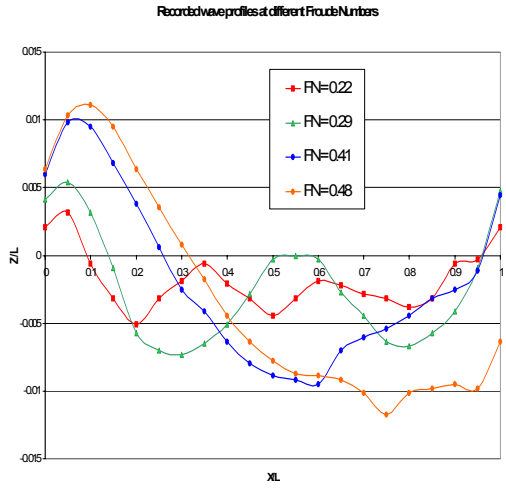

Figure A.4. Experiments: Wave profiles at different Fn as measured from the video tape.

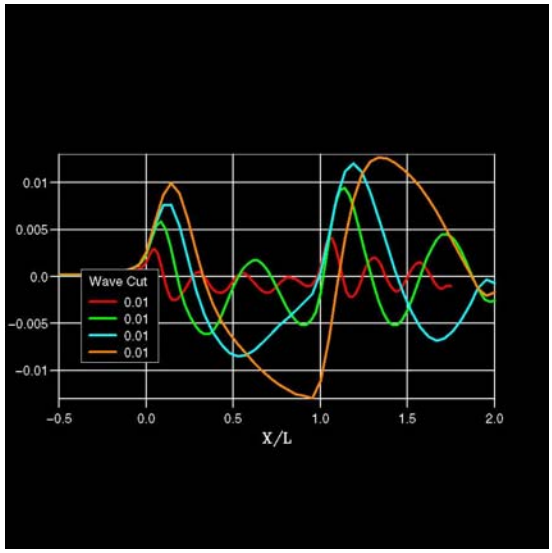

Figure A.5. CFD: Wavecuts at Y/L = 0.014, 8.82 cm from the centre line. Fn = 0.2, 0.3, 0.4 and 0.5 respectively.

Figure A.5 shows the wavecuts for four different Froude Numbers as computed by SHIPFLOW, at a transversal position very close to the side of the plate. The agreement with Figure A.4 over the length of the plate (between x/L = 0 and 1) is fairly good and demonstrates the confidence that can be drawn from the CFD computations.

A.2.3 The 2.72m long wave-piercing catamaran model

The software SHIPFLOW was used to complement the physical experiments. The objective was twofold: firstly, to establish how well the computed total resistance agreed with the measured data and secondly, to use the CFD prediction of the wave resistance to calculate the differences in viscous resistance between the different surfaces.

SHIPFLOW computes the total resistance as (Shipflow, 1999):

$$C_T = C_F + C_{PV} + C_W = C_V + C_W = (1+k)C_{F,ITTC} + C_W$$

where:

C_F is computed with a boundary-layer momentum integral method along the streamlines of the hull in XBOUND

C_{PV} is the pressure resistance coefficient of viscous origin, also computed with a boundary-layer momentum integral method along the streamlines of the hull in XVISC

C_V is the viscous resistance coefficient, equal to $C_F + C_{PV}$

C_W is the wave resistance coefficient, computed with a potential flow method

k $= (C_F + C_{PV})/C_{F,ITTC} - 1$

As mentioned before in Section 3.2, the basic assumption in the following analysis is that the wave making resistance is considered independent of the surface conditions. Hence the direct influence of the surface conditions on the viscous resistance will be quantified by subtracting C_W from C_T. As will be seen, C_{PV} is computed as being two orders of magnitude smaller than C_W and C_F. Thus, any effect of the surface conditions on C_{PV} will be so small that it is acceptable to say that the differences in viscous resistance will be equal to the differences in frictional resistance. This is useful to bear in mind when comparing the results with the other experiments or with literature in fluid mechanics.

SHIPFLOW requires the input of offset co-ordinates, but since the plans of neither the model nor the full-scale vessel were available, the only way of obtaining data was by directly measuring them. Because of time and space restrictions, this was only done for the demi-hull.

By using foam blocks, the model was levelled horizontally with the waterline as shown in Figure A.6. Consequently, 5 draught lines were marked onto the hull with the height gauge.

Starting from the stern, vertical stations, regularly spaced at 10cm, were marked, were delineated by using cords, as shown in Figure A.7. Subsequently, the height gauge and a caliper were used to measure the transverse and vertical co-ordinates for a ‘sufficient’ number of points at each station. The number of points of a station is considered ‘sufficient’ if the local curvature of the surface can accurately be described by a spline interpolation through these points.

In this way, 33 stations described by 458 points in total made up the offsets of the demihull of the model. Figure A.8 shows the offset file and Figure A.9 shows the mesh generated by SHIPFLOW from the offset file. Including the free surface, the mesh would typically consist of 1342 panels.

Figure A.6. Photograph of the levelled model and the marking method of the draught lines.

Figure A.7. The method of marking equally spaced stations with cords and measuring vertical and transverse co-ordinates of points with the height gauge and caliper.

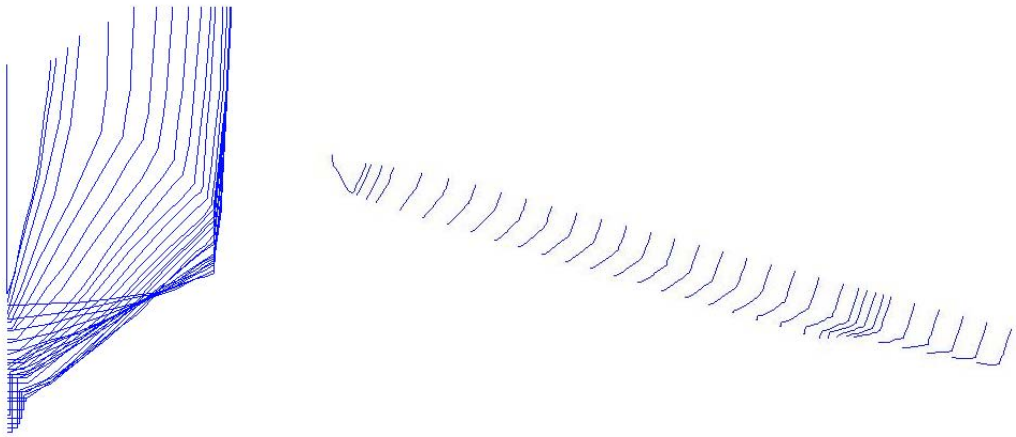

Figure A.8. Graphical views of the offset file.

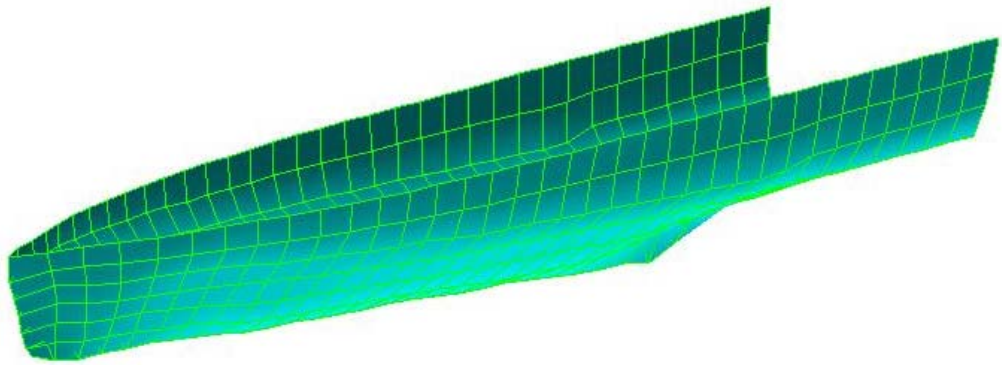

Figure A.9. View of the mesh generated by SHIPFLOW for the computations.

Table A-2 presents the geometrical particulars of the model, in column 1 and non-dimensionalised by the length in column 2 and of the mesh generated by SHIPFLOW, and demonstrates good agreement.

Table A-2. Geometrical particulars of the physical demihull and the CFD mesh

	Model	Non-dimensional	CFD
L	2.717m	1	1
B	15.5cm	0.057048	0.05706
T	11.8cm	0.04343	0.04343
S	1.318m^2	0.17854	0.17854
∇	47.394kg	0.00236295	0.00236405

The SHIPFLOW computations were carried out for 21 different speeds. A typical command file is shown below:

```
xflow
  titl( titl="M1441"  )
  prog( xmesh, xpan, xbound)
  hull( catamaran)
  offs( file = "off_m1441_1", lpp=2.717, ysign=1.0)
  vshi( fn = [0.115994], rn = [1428142])
end


xmesh
   body( grno = 1, offsetgroup = "hull",
         station = 36, point = 7,
```

```
         ytra = 0.3625 )
   body( grno = 2, offsetgroup = "hull",
         station = 36, point = 7,
         ymir,
         ytra = 0.3625 )
   free( grno = 3,
         y2side = 0.0,
         nbd4 = 1, ibd4 = [2],
         point = 4,
         stau = 10, stam = 20, stad = 20 )
   free( grno = 4,
         nbd2 = 1, ibd2 = [1],
         point =16, str1 = 1, df1 = 0.02,
         stau = 10, stam = 20, stad = 20  )
   tran( grno = 5,
         nbd1 = 2, ibd1 = [1,2],
         point = 5, stad = 20 )
end
xpan
   cont( eqav = 1.0e-3, free)
   iter( maxit = 20 )
   wsca( scale = 1.0 )
end
xbound
  trac( grou=1, stre=10, stat=25, ista=10,
      s1=0.05, sn=1.0, p1=0.05, pn=0.95 )
  trac( grou=2, stre=10, stat=25, ista=16,
      s1=0.05, sn=1.0, p1=0.05, pn=0.95 )
  limi( grou=1, stre=10, stat=10, ista=1, s1=0.1, sn=0.15 )
  limi( grou=1, stre=10, stat=10, ista=1, s1=0.5, sn=0.55 )
  limi( grou=1, stre=10, stat=10, ista=1, s1=0.9, sn=0.95 )
  limi( grou=2, stre=10, stat=10, ista=1, s1=0.1, sn=0.15 )
  limi( grou=2, stre=10, stat=10, ista=1, s1=0.5, sn=0.55 )
  limi( grou=2, stre=10, stat=10, ista=1, s1=0.9, sn=0.95 )
  inic( sgro=1, t11=[5.0e-4] )
  inic( sgro=2, t11=[5.0e-4] )
end
```

Figure A.10 shows the frictional, wave and total resistance coefficients as computed by SHIPFLOW, together with the total resistance coefficients as measured from the experiments. The total resistance coefficients computed by SHIPFLOW shown in Figure A.10 is the direct sum of the wave and frictional resistance coefficient and omits the viscous pressure resistance coefficient, C_{PV}. C_{PV} can only be computed by SHIPFLOW for monohull ships (by including the RANS-computations, XGRID and XVISC, in the command file) and should be added to the values plotted here. C_{PV} was calculated for a number of speeds for the demihull in isolation and found to be one to two orders of magnitude smaller than C_F and C_W, justifying its omission in computing C_T. For instance, at V = 0.154m/s, C_T will be equal to 0.020467 instead of 0.020373, which is less than 0.5% larger. At V = 0.354m/s, C_{PV} = 0.0001016 and its addition would make C_T 1.4% larger.

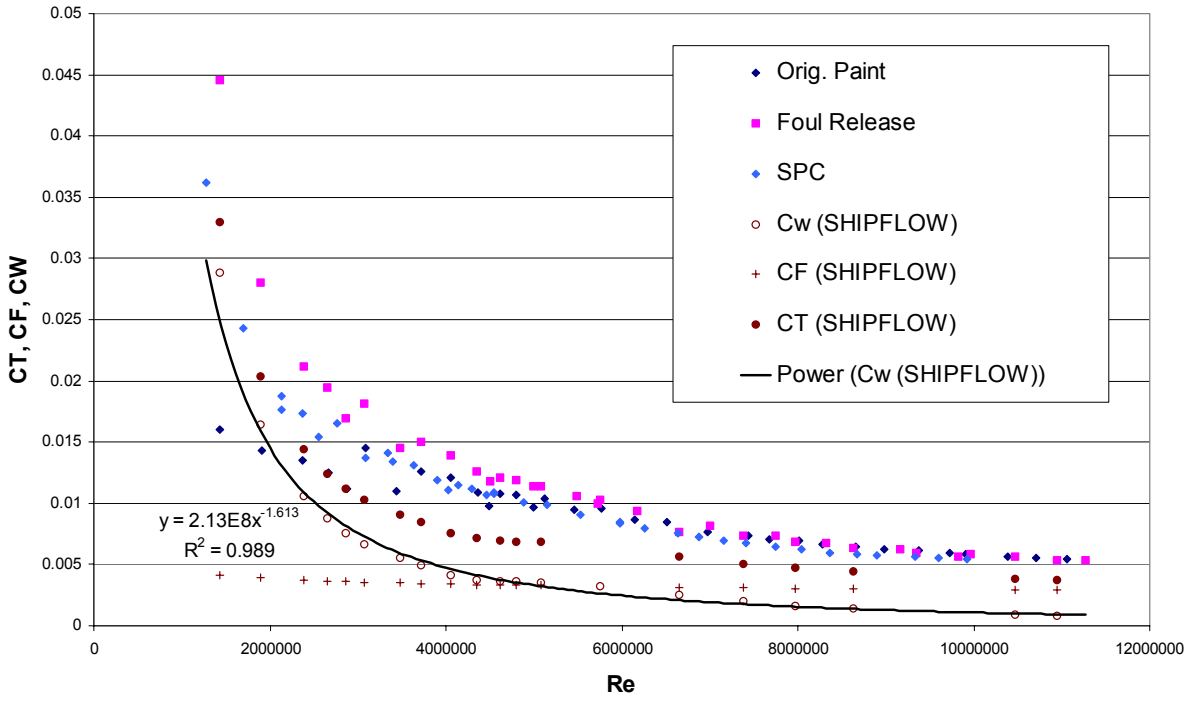

Figure A.10. Wave, frictional and total resistance coefficients computed by SHIPFLOW and the measured total resistance coefficients of the three tested surfaces.

Figure A.10 also shows that the wave resistance coefficient computed by Shipflow corresponds well to the equation: $C_W = 2.13 \cdot 10^{8} \cdot Re^{-1.613}$. This equation was used to subtract the wave resistance coefficient from the total measured resistance coefficient to obtain the frictional resistance coefficient of the three different surfaces. At a Reynolds number of $5 \cdot 10^{6}$, the wave resistance makes up less than 30% of the total resistance.

Figure A.11 compares the running trim against Froude number from the measurements and from the computations by SHIPFLOW and shows considerable differences at higher Froude numbers.

Figure A.12 compares the sinkage (in mm) at the centre of gravity measured from the measurements with the results from SHIPFLOW plotted against Froude number. The agreement in Figure A.12 between SHIPFLOW and the present experiments is fairly good.

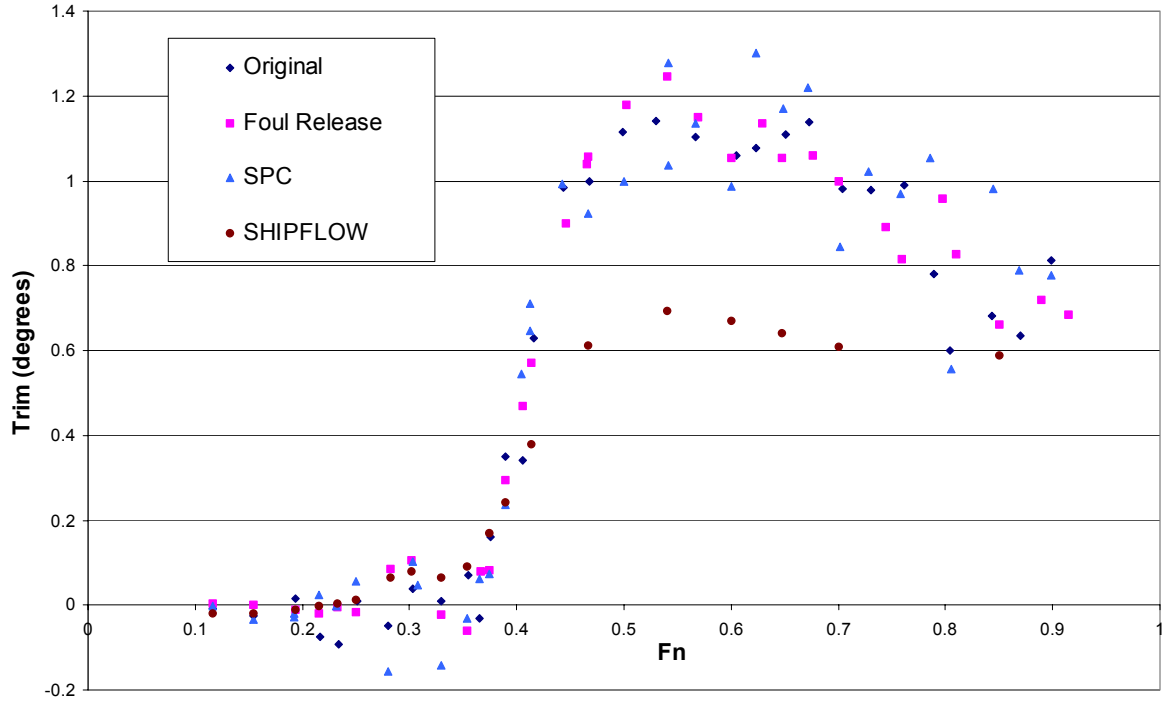

Figure A.11. Running trim in degrees against Froude number for the measurements and for the computations.

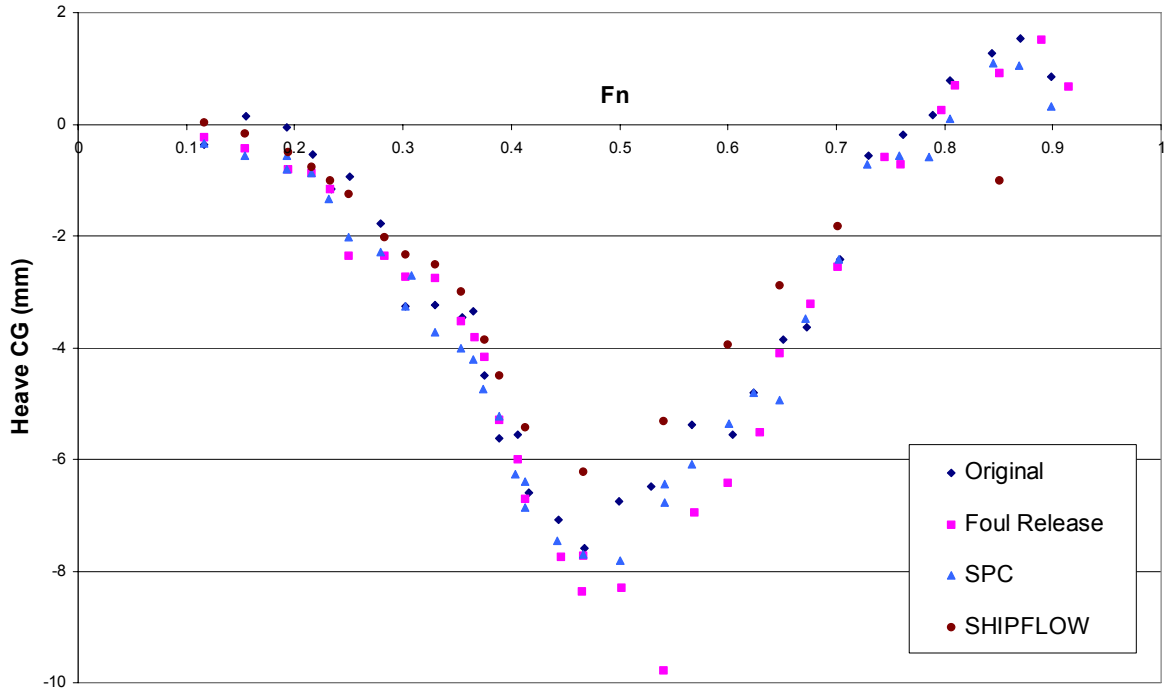

Figure A.12. Sinkage versus Froude number for the measurements and for the computations.

An investigation has also been carried out with SHIPFLOW to investigate the variation in draught. Figure A.13 shows the variation in the computed total (= C_W + C_F) and frictional

resistance coefficients for 4 draughts: level, 4mm deeper, 15mm deeper and 15 mm higher. The change in draught only changes the wave resistance visibly, the frictional resistance does not alter significantly. Since the estimated variation in draught for the different test series was expected to be less than 2mm, the influence is considered negligible. Figure A.14 shows the variation in the running trim for the four different draughts, which is only significant above Fn = 0.5. Figure A.15 shows the variation in the sinkage at the centre of gravity for the four different draughts. Only for the smaller draught (15mm higher) there is a very significant difference due to the more important change in hull geometry, cf. Figure A.9.

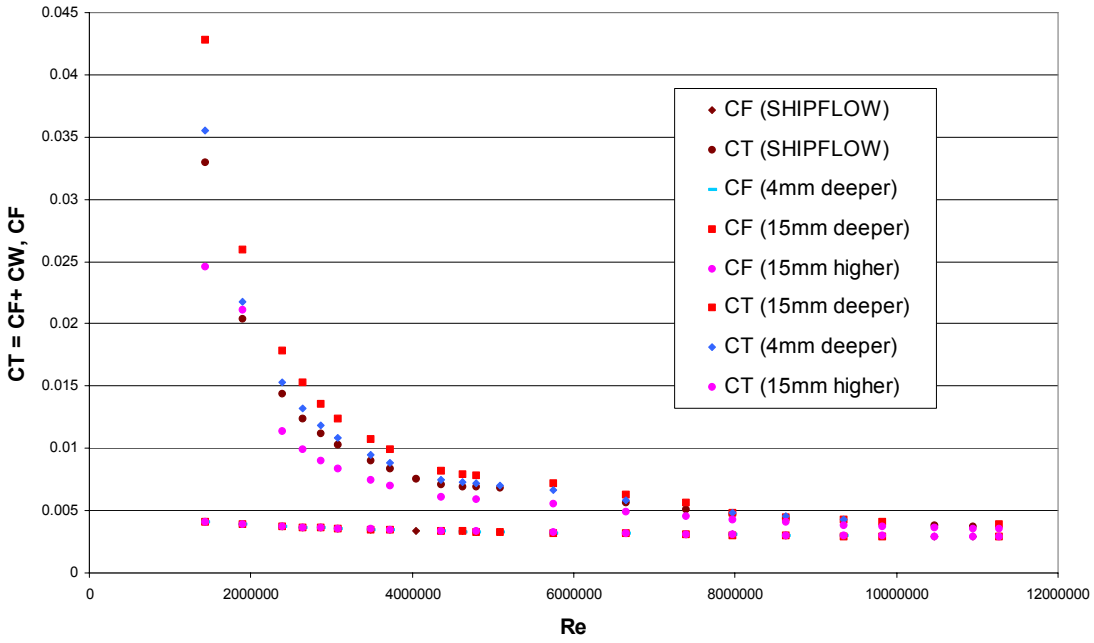

Figure A.13. Influence of different draughts on the computed total resistance and frictional resistance coefficients.

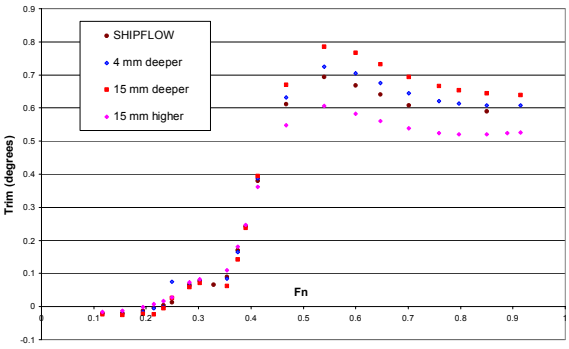

Figure A.14. Influence of different draughts on the running trim.

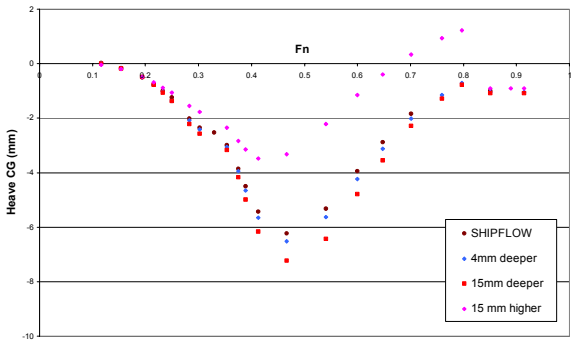

Figure A.15. Influence of different draughts on the sinkage at the centre of gravity.

Appendix B. Principles and errors of LDV measurements

This Appendix describes the general principles of the Laser Doppler Velocimetry equipment used for the boundary-layer experiments described in Chapter 5. In Section C.1, the various components of LDV are discussed. The parameters and conditions that deserve particular consideration for accurate flow measurement are also given. Three reviews on LDV that were consulted are Buchave et al. (1979), Adrian (1996) and Fingerson and Menon (1998). In Section C.2, some of the common errors encountered in LDV measurements are discussed. Procedures required to correct or minimise these errors are also outlined.

B.1 Principles of Laser Doppler Velocimetry

B.1.1 Laser Source

Laser light has two very important characteristics: it is monochromatic and coherent. The fact that a laser beam is monochromatic means that its energy is concentrated in an extremely narrow bandwidth, and the fact that it is coherent means that all emitted radiation has the same phase, both in space and in time. A laser beam is also highly collimated and has a plane of minimal cross section. The light intensity over this cross section has a Gaussian distribution. The beam diameter is defined as the distance between points in the cross section where the light intensity has dropped to e^{-2} of the maximum value. The beam diameter is an important parameter because it influences the measuring volume dimensions. Other important parameters in selecting a laser source for application are the power requirements, the cost and the light frequency. The light frequency is particularly important because it affects the fringe spacing, the photo-detector quantum efficiency and scattering from particles. The amount of power scattered from particles defines the signal level and the signal-to-noise ratio (SNR).

B.1.2 Transmitting Optics and Measuring Volume

The transmitting optics consists of a beam splitter, a Bragg cell and a convergent lens or mirror. Additionally, it may also contain extras like a beam expander. For a dual beam system, an intense, highly collimated light beam from the laser is divided into coherent beams

of equal power by the beam splitter. The Doppler frequency is not dependent on the direction of the velocity. A positive and a negative velocity of the same magnitude will result in the same Doppler shift. To remove this directional ambiguity, laser beams are frequency-shifted by Bragg cells. The two coherent beams are transmitted through a focussing lens and directed into the flow. Ideally, the two beams should intersect at the focal point of the lens. In the plane of intersection, the two beams give rise to an interference pattern known as 'fringes'. The spatial region from which measurements are obtained is essentially the intersection of these beams and this region is referred to as the measuring volume. The measuring volume is defined by the locus of e^{-2} intensity points and is ellipsoidal in shape. The dimensions of the control volume depend on the wavelength λ of the laser beam and the optic parameters. The number of fringes and the fringe spacing within the measuring volume depend on the optical parameters and the size of the measuring volume.

For the present experiments, a two-component four-beam set-up was used, i.e. two perpendicular dual beams of different wavelength (green and blue colour) in order to measure both the streamwise and the wall-normal velocity component.

B.1.3 The Receiving Optics and Photo-detectors

When a scattering particle passes through the measuring volume, it scatters or reflects the incident light. The scattered light is collected by a set of receiving lenses and focused onto a photo-detector. The photo-detector uses the 'photoelectric effect', which is the absorption of photons and emission of electrons to convert the optical signal into an electrical signal for processing. Various types of photo-detectors exist; the present system uses a photo-multiplier.

B.1.4 Signal Processing Systems

The selection of a signal processor for fluid flow measurements depends on the type of signal generated, for example, high or low particle density and also on the flow information desired. The appearance of the photo-detector output signal depends on the collected light

intensity, on the number of particles crossing the measuring volume at any one time and also on the scattering characteristics of the particles. At extremely low particle density, the signal consists of a train of pulses corresponding to individual collected particles. In this case, special techniques are required to recover the Doppler frequency (Tachie, 2000). On the other hand, if the particle density is extremely high so that many particles are present in the measuring volume at any time, the Doppler signal is continuous but its phase and amplitude would vary randomly. This randomness introduces an additional error in the Doppler frequency measurement, called 'ambiguity noise'. If the particle density is sufficiently large to provide a quasi-continuous signal but low enough for the measuring volume to contain at most a single scattering particle at any time, the signal received by the photo-detector will consist of a series of 'bursts' corresponding to a particle crossing. Each burst can be viewed as an amplitude-modulated sinusoidal function of frequency f_D. The amplitude modulation depends on the light intensity variation within the measuring volume, while differences between bursts reflect differences between particle sizes and crossing paths. A particle passing through the measuring volume will cross a certain number of fringes per unit time. Using a suitable signal processor, the signals are processed for the determination of the Doppler frequency. If the frequency f_D of fringe crossing is known, the velocity of the particle is given by

$$U = C \cdot f_D \qquad \text{(A. 1)}$$

whereby C is a calibration factor which depends on the optical parameters. Equation A.1 shows a linear velocity-frequency relationship.

B.1.5 Seeding

Scattering particles are the basic source of the Doppler signal. For liquid flows, the particles may typically be 0.5 to 50μm in diameter. According to Adrian (1996), the scattering particles have more influence on the quality of the signal than any other component of the system. For example, the signal strength can be increased by 10^2 to 10^4 by increasing the particle diameter from several tenths of a micron to several microns. Improvements of these orders of magnitude are difficult, expensive, or perhaps, impossible to achieve by increasing the laser power or otherwise improving the optical system.

The velocity measured by the LDA system is that of the scattering particle. Therefore only if the scattering particles faithfully follow any changes of the flow velocity can one

expect the measurements to yield velocity data that accurately represent the flow velocity. If the scattering particles are too large or if their density is too high then, as a result of inertia, they may not respond to velocity changes sufficiently rapidly. The aerodynamic size of a scattering particle, which is a measure of its ability to faithfully follow the flow, is one of the most important properties of an individual scattering particle. The signal-to-noise-ratio (SNR) that it produces is also important. A high SNR requires that the particle effectively scatters the incident light. The concentration and uniformity of the particle population also play important roles. Ideally, particles that have the same density as the fluid, large effective area in regard to scattering power, very uniform properties from one particle to the other, easily controlled concentration, and low expense are desirable. For liquid flows, the velocities are usually small and the primary limitation on particle size comes from the settling velocity rather than the ability to follow the flow. In water flows, naturally occurring hydrosols are convenient and often yield satisfactory results. In the present experiments extra 'seeding' was put in the flow by adding silver coated (soda lime borosilicate) glass spheres with a mean particle size of 16.3μm (ranging from 8.4-24.8μm).

An ideal system considers a single particle in the measuring volume at any one time. In densely seeded flows, with the receiving optics configured in backscatter mode, validation of the Doppler signal from multiple particles within the measuring volume may contaminate the accuracy of flow measurements. This is particularly true if the measuring volume is long. If the particle concentration is low, the streamwise and vertical velocity fluctuations would be independent of the spanwise extent of the LDA measuring volume. Another positive side of a relatively low data rate is that it is unlikely to measure multiple particles in one time window.

B.2 Errors in LDV measurements

B.2.1 Velocity bias

The LDV measurements in this work were carried out in burst mode, which operates on signals generated by single particles passing through the measuring volume and measures the velocity of the particle while it is in the measuring volume. At relatively high velocities, more particles are measured per unit time than at low velocity. The arrival rate of the particle is generally not statistically independent of the flow velocity which drives them to the measuring volume (Edwards, 1987). If the flow statistics are calculated by simply summing the velocities of all the measured particles and dividing by the number of particles, i.e. arithmetic or particle averaging, the statistics may be seriously biased because there is a greater likelihood of high velocity particles passing through the measurement volume during a given sampling period.

In turbulent flows, velocity bias occurs when the particle measurement rate is correlated to the magnitude of the instantaneous velocity vector at a point in the flow field (McLaughlin and Tiderman, 1973). Many corrections and sampling strategies have been proposed over the years to eliminate velocity bias. According to McLaughlin and Tiderman (1973), velocity bias towards higher velocities is minimised by using naturally and uniformly occurring seeding. The use of additional seeding, as done presently, may explain the velocity bias towards higher velocities for some of the near-wall measurements. Attempts have also been made by a number of researchers to experimentally verify some of these analytical studies, but the results obtained are inconclusive as to the magnitude and even the existence of velocity bias (Tachie, 2000). These experimental results notwithstanding, many LDV users routinely correct for velocity bias by using different sampling techniques. Tachie (2000) made a study on the influence of three different sampling techniques (arithmetic or particle averaging, transit time weighting and inter-arrival time weighting) in a turbulent channel flow but found no significant differences between the three techniques. The present experiments were transit time weighted in order to correct for velocity bias.

B.2.2 The effect of multiple particles in the measuring volume

In practice more than one particle may be present in the measuring volume so the photo-detector usually receives light scattered from particles distributed throughout the illuminating beams. In densely seeded flows or in a long measuring volume, the probability of the presence of multiple particles within the measuring volume is high. When multiple particles are present in the measuring volume, the Doppler signal on the U and V channel may be validated simultaneously but may not come from the same particle. This may cause the Reynolds shear stress to be underestimated. Tachie (2000) mentions that the spanwise extent of the measuring volume is recommended to be less than 15 viscous units, which is much smaller than in the present experiments. However, in view of the good agreement between the Hama method and the Reynolds shear stress method used in this work, the effect of multiple particles in the measuring volume is considered negligible.

B.2.3 Velocity gradient bias

Due to the finite size of the measuring volume, LDV data are not really point measurements but are measurements integrated in space over the measuring volume. Finite volume size may cause large velocity gradients and may also present difficulty in accurately locating the wall (y = 0). If there is a non-negligible mean velocity gradient in the measuring volume, the resulting probability function will be broadened and skewed. As a result, time-averaged turbulence properties, especially in the vicinity of the wall, will show a dependence of the measuring volume size and require volume correction. Durst et al. (1995, 1998) discussed the effects of finite measuring volume and developed correction formulae to correct for velocity gradient bias. Schultz (1998, 2000) found that the application of these formulae to the mean velocity and other turbulence quantities (except u'_{RMS}) was negligible. Durst et al. (1998) mention that the effect on the streamwise turbulence intensity is negligible for $y^+ > 15$. Therefore, the correction formulae were not applied in this work.

B.2.4 Non-orthogonality

It is a common practice in LDV experiments to tilt the probe towards the wall in order to obtain velocity data closer to the wall (e.g. Schultz, 1998; Swain and Schultz, 1999;

Schultz, 2000; Tachie, 2000). When the probe is tilted towards the wall, the measured vertical component will be tilted relative to the normal of the wall. This may contaminate the velocity data, especially if the angle of tilt is large. Tachie (2000) carried out a systematic study of the tilt angle on turbulent channel flow measurements and found no significant effect for tilt angles $\leq 5°$.

B.2.5 Others: validation bias, fringe bias and errors due to noise

Fringe bias is due to the fact that scattering particles passing through the measuring volume at large angles may not be measured since several fringe crossing are needed to validate a measurement. In this work, the fringe bias was considered insignificant, as the beams were shifted well above the burst frequency representative of twice the free-stream velocity

Validation bias results from filtering too close to the signal frequency and any processor biases. In general these are difficult to estimate and vary from system to system. No corrections were made to account for validation bias.

Electronic noise resulting from signal processing equipment as well as light scattered from small impurities on the solid wall and test windows may give an erroneous contribution to LDV measurements. Errors due to noise have been treated by Durst et al. (1998) who showed that the effect of electronic noise is negligible for $y^+ \geq 2$.

Appendix C. Uncertainty analysis

This Appendix contains a detailed uncertainty analysis of the experimental boundary-layer measurements carried out in the Emerson and CEHIPAR Cavitation Tunnels which have been described in Chapter 5.

C.1 Uncertainty analysis of the boundary-layer experiments carried out in the Emerson Cavitation Tunnel

Precision uncertainty estimates for the velocity measurements were made using repeatability tests. Ten replicate profiles were taken on both the STEEL and the SPC surface. The SPC surface was selected for the uncertainty analysis over a rough surface, because the measurements over this surface proceeded with more difficulty than over the other surfaces. Specifically, it was more difficult to get readings close to the wall of the SPC surface; the current through the anodes would often exceed its maximum allowed value and readings could sometimes not start until up to 0.5mm from the wall. Sometimes, it would occur that readings close to the wall were obtained, but that the average values would be too high and would not fall below a certain minimum for U. This would indicate that probably only faster particles were picked up and the minimum value of U depended on the initial value of the current through the anode. The closer the current was to its maximum allowed value, the more realistic the readings. Recalibration of the equipment, which occurs every 15 minutes, would consequently often have a significant effect on the readings, causing a clear shift in the velocity profile. This problem occurred a couple of times for each of the different surfaces, but more often with the SPC surface. Some positions seemed more prone to this problem than other positions. When the recalibration would cause a major shift in the velocity profile and thus jeopardise the Clauser and Hama methods to determine U_τ, the measurement would be repeated until the recalibration no longer occurred or until the shift in the velocity profile was not so drastic as to cause problems with the further analysis. STEEL4pos5, for example, required four repeats before satisfactory measurements were obtained (STEEL45pos5).

The ten replicate profiles were carried out at position 3, 1.607m from the leading edge at a speed of 3m/s. Figure C.1 and Figure C.2 show the average data rate (in Hz) and the average number of collected validated data for both the surfaces respectively; both were slightly lower near the wall for the SPC but they approach the same level as the STEEL

surface in the outer layer. The total number of collected data in the outer layer is on average lower than 4096 because this value was not reached all the time throughout the uncertainty analysis.

The standard deviation for each of the measurement quantities was calculated for both the STEEL surface sample and the SPC surface sample. In order to estimate the 95% confidence limits for a statistic calculated from a single profile, the standard deviation was multiplied by the two-tailed t value for 9 degrees of freedom and $\alpha = 0.05$ as given by Coleman and Steele (1999), $t = 2.262$.

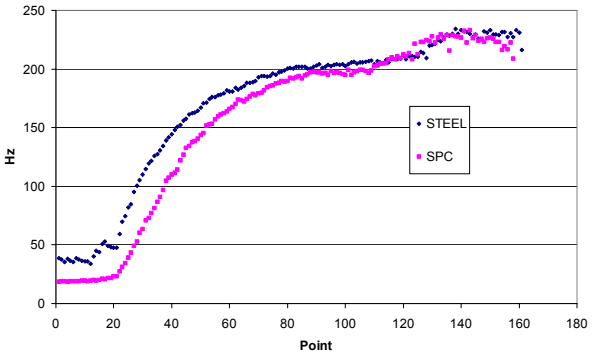

Figure C.1. Average data rate

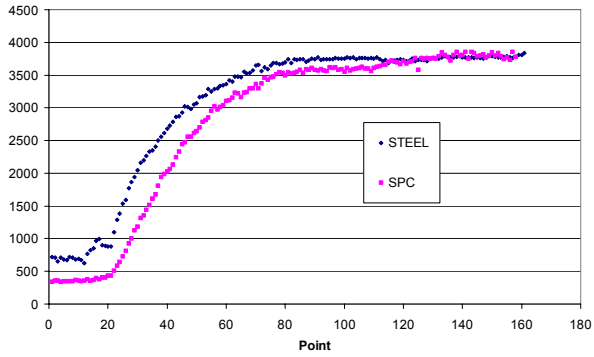

Figure C.2. Average number of collected validated data

Figure C.3 and Figure C.4 show the resulting average precision uncertainties in the mean velocities U and V, the turbulence intensities u'_{RMS} and v'_{RMS} and the Reynolds stress $-\overline{u'v'}$ for the STEEL and SPC surface respectively. The figures show that three regions can be distinguished as far as different levels of average uncertainty estimates are concerned.

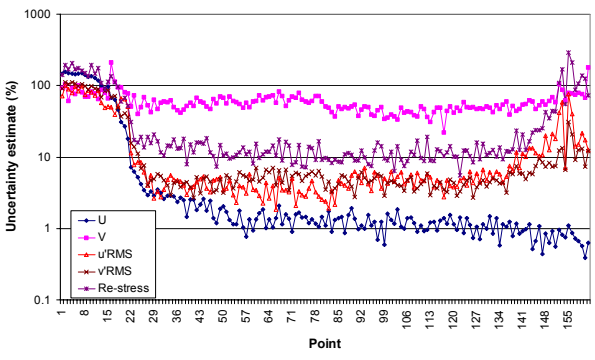

Figure C.3. Uncertainty estimates for the STEEL sample

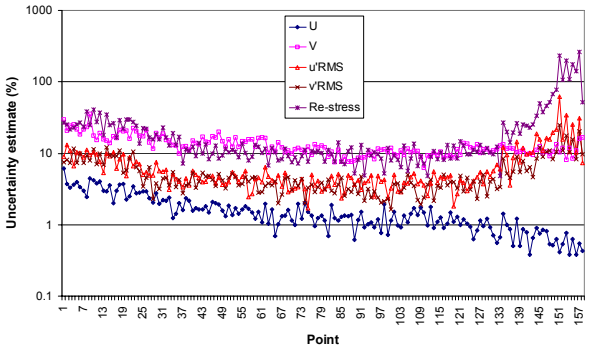

Figure C.4. Uncertainty estimates for the SPC sample

A first region, taken as $y^+ < 50$, corresponds more or less to the viscous sublayer, a second region largely corresponds to the velocity defect law region, and a third region is taken as $y/\delta > 0.8$. Table C-1 shows the average uncertainty estimates for each of the measured quantities over the different regions.

Table C-1. Uncertainty estimates for the measured quantities

	Region	U	V	u'_{RMS}	v'_{RMS}	Re-stress
STEEL	$y^+<50$	±97.8%	±86.9%	±66.0%	±76.6%	±126.0%
	middle	±1.5%	±52.4%	±4.7%	±4.8%	±12.1%
	$y/\delta > 0.8$	±0.7%	±54.9%	±23.3%	±11.1%	±90.4%
SPC	$y^+<50$	±3.4%	±20.5%	±8.8%	±8.6%	±27.1%
	middle	±1.4%	±12.1%	±4.5%	±3.8%	±11.2%
	$y/\delta > 0.8$	±0.6%	±11.1%	±18.3%	±10.9%	±87.9%

The paradoxical results, i.e. larger uncertainty estimates for the measured quantities over the smooth STEEL surface, can be explained by the data collection method. For the SPC surface, the tunnel speed was increased from 0 to 3m/s and the data collection was started. The tunnel velocity was never changed except at the end of the day. The ten measurements were acquired over three days. In contrast, the tunnel velocity was briefly sped up or slowed down after *each* measurement over the STEEL surface. This procedure had profound consequences for all measured quantities near the wall (and, apparently, for V over the whole boundary layer). In effect, it was observed that the test specimen curved slightly under the suction induced at higher speeds, so that when the tunnel speed was decreased again, the effective origin of the wall would not be exactly the same as before. The effect of the measurement procedure is illustrated in Figure C.5 and Figure C.6, which show the U-profiles for the STEEL and SPC surface respectively. Consequently, the uncertainty estimates over the inner layer were much larger for the STEEL surface than for the SPC surface. However, the average uncertainty estimates over the other two regions ($y^+ > 50$) corresponded well for both surfaces (except for V).

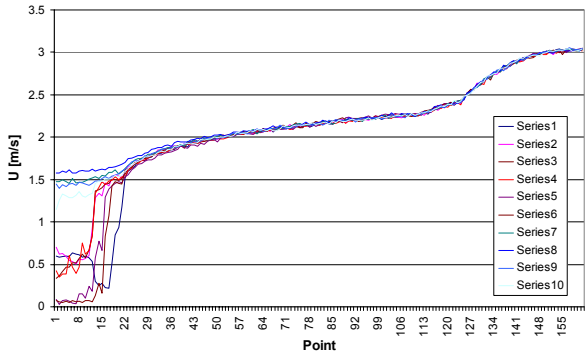

Figure C.5. U-profiles for the STEEL uncertainty sample

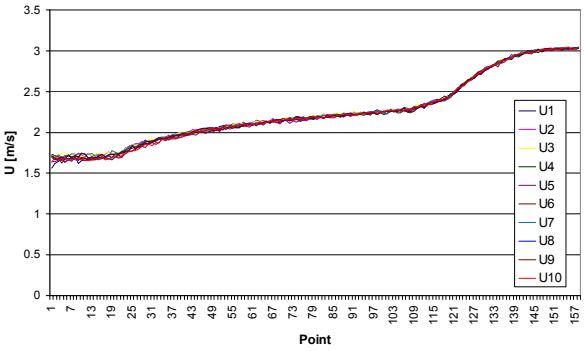

Figure C.6. U-profiles for the SPC uncertainty sample

Figure C.6 also shows that the near-wall data obtained for the SPC surface were biased, as mentioned above.

LDV measurements are susceptible to a variety of bias errors, including fringe bias, validation bias, velocity and velocity gradient bias. These were considered in Appendix B.2.

The analysis was carried out ten times for each replicate measured profile in order to determine the uncertainty on the various parameters. Table C-2 and Table C-3 present the uncertainties on the parameters with $\alpha = 0.05$ ($t = 2.262$) at a 95% confidence level.

Table C-2. Uncertainty estimates for the boundary-layer parameters for STEEL

	Average	S (StDev)	2.26S (%)
Ue	3.05	0.01	0.72
Reθ	11969.66	410.13	7.75
δ	35.20	0.97	6.21
δ1	4.60	0.13	6.62
θ	3.56	0.09	5.65
H	1.29	0.02	3.17
Tu	0.0195	0.0014	15.69
Reδ1	15481.76	655.08	9.57
ε	0.07	0.07	230.64
Uτ (Clauser)	0.1103	0.0002	0.50
cf	0.00262	0.00002	1.43
Uτ (stress)	0.1114	0.0010	2.02
cf	0.00268	0.00005	4.45
Uτ (Hama)	0.1102	0.0004	0.79
cf	0.00262	0.00003	2.36
Π	0.45	0.003	1.59

Table C-3. Uncertainty estimates for the boundary-layer parameters for the rough surfaces

	Average	S (StDev)	2.26S (%)
Ue	3.03	0.01	0.80
Reθ	12300.27	521.99	9.60
δ	33.85	0.85	5.68
δ1	4.22	0.11	5.83
θ	3.35	0.08	5.54
H	1.26	0.003	0.58
Tu	0.0209	0.0013	13.56
Reδ1	15482.27	674.83	9.86
ε	0.57	0.13	50.13
Uτ (stress)	0.1169	0.0006	1.15
cf	0.00298	0.00003	2.43
ΔU+	1.22	0.12	22.68
Uτ (Hama)	0.1231	0.0007	1.33
cf	0.00331	0.00005	3.08
Π	0.33	0.03	18.28
ΔU+	2.67	0.17	14.74

The uncertainty estimates on the spectral measurements of the SPC surface sample have been calculated in a similar manner. Figure C.7 shows the collected streamwise velocity spectra at $y/\delta = 0.05$ for the ten replicate measurements.

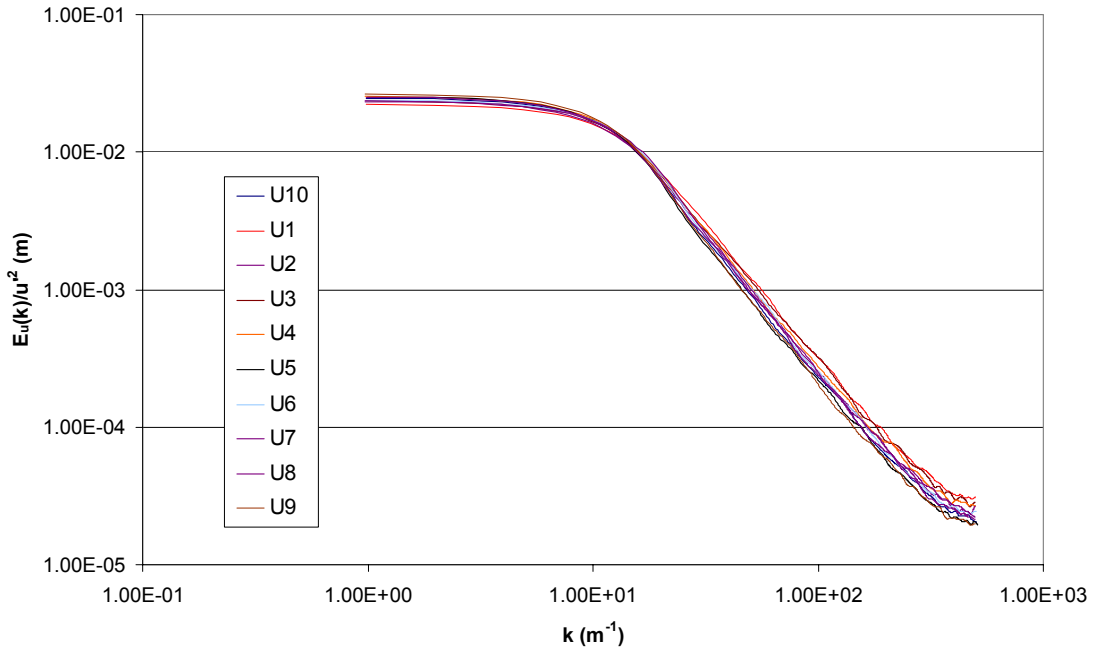

Figure C.7. Comparative spectra $E_u(k)/u'^2$ for the SPC uncertainty sample at 3pos3 and at $y/\delta = 0.05$.

Figure C.8 shows the relative uncertainties for the streamwise and wall-normal spectra at y/δ = 0.05 and 0.8 for each of the 512 spectral samples. Except for the lowest wavenumbers, the relative uncertainties of the spectra crudely are between 30 and 40%. The uncertainties on the integral length scales can be read off at spectral sample number 1 and are higher for the wall-normal (ca. 31%) than for the streamwise integral length scales. These uncertainties are also listed in Table C-4 along with the uncertainties on the wavenumbers (which do not change with spectral sample number).

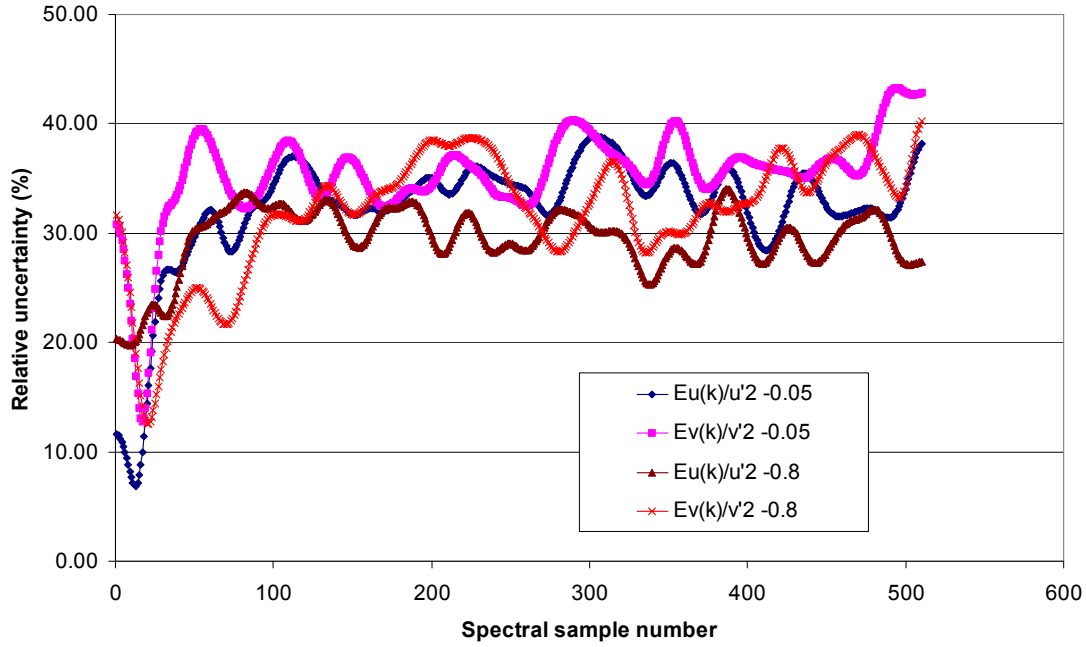

Figure C.8. Relative uncertainties of the different spectra according to spectral sample number.

Table C-4. Uncertainty estimates for the integral length scales and wavenumbers.

	Average	S (StDev)	2.26S (%)
Lu-0.05	9.68E-04	4.99E-05	11.66
Lv-0.05	4.23E-05	5.77E-06	30.86
Lu-0.8	1.04E-03	9.30E-05	20.30
Lv-0.8	4.41E-05	6.16E-06	31.59
k-u,0.05			1.84
k-v,0.05			13.83
k-u,0.8			1.18
k-v,0.8			11.70

The uncertainty on derived parameters was calculated by the uncertainty propagation method as specified in Coleman and Steele (1999, Chapter 4). For example, the uncertainty (in %) on U_e/U_τ was calculated as the square root of sum of the uncertainties in U_e and U_τ (as obtained with the Hama method) squared. For the STEEL surface, the uncertainty was thus

determined at 1.07%. However, U_e/U_τ is also equal to $\sqrt{2/c_f}$ so that one could argue that the uncertainty in c_f is equal to $(1.07)^2 = 1.14\%$ based on the uncertainty propagation method, rather than the 2.36% given in Table C-2, which is based on replicate analysis. However, since the uncertainties from the replicate analysis are directly determined from measurements, they were preferred to the uncertainties determined by uncertainty propagation and they have been used throughout for the parameters listed in Table C-2 and Table C-3.

C.2 Detailed uncertainty analysis of the boundary-layer experiments carried out in the CEHIPAR Cavitation Tunnel

As in Section C.1, uncertainty estimates for the velocity measurements were made using repeatability tests. Ten replicate profiles were taken on the CFR surface. The CFR surface was selected for the uncertainty analysis because the measurements over this surface proceeded with more difficulty than over the CSPC surface. It was more difficult to get meaningful readings close to the wall. Particularly at the speed and velocity combination chosen for the uncertainty analysis, it would occur that readings close to the wall were obtained, but that large negative U values were picked up. The first meaningful U data obtained were often relatively high and quite far from the wall ($y^+ > 50$).

The time available for the uncertainty analysis was very limited, so it was decided to take only half of the number of data points usually taken for the measurements, by using double spacing for the selected regions. Evidently, this has large repercussions on the uncertainty of the boundary-layer parameters, particularly δ, δ_1, θ and H, but also for the skin friction characteristics which were determined with less accuracy than for the actual measurements. It is felt that the number of points selected for the measurements is a minimum, and that the number of points chosen for the uncertainty analysis is too low, jeopardizing accuracy. Logarithmic spacing as used by Schultz (1998) could further restrict the number of points necessary for accurate determination of the skin-friction parameters but would leave a fairly large uncertainty on δ.

The ten replicate profiles were carried out at position 3, 1.607m from the leading edge at a water tunnel speed of 5m/s. Replicates 4, 7 and 8 were incomplete because the computer crashed. Figure C.9 and Figure C.10 show the average data rate (in Hz) and the average number of collected validated data.

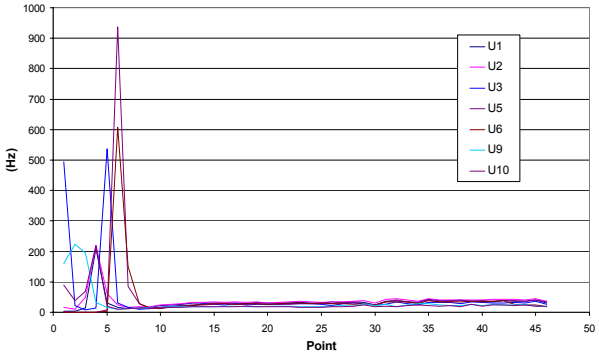

Figure C.9. Average data rate

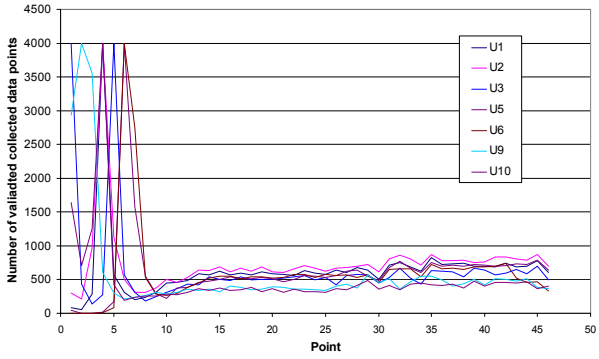

Figure C.10. Average number of collected validated data

The standard deviation for each of the measurement parameters was calculated over the sample. In order to estimate the 95% confidence limits for a statistic calculated from a single profile, the standard deviation was multiplied by the two-tailed t value for 7 degrees of freedom and $\alpha = 0.05$ as given by Coleman and Steele (1999), $t = 2.575$.

Figure C.11 shows the resulting average precision uncertainties in the mean velocities U and V, the turbulence intensities u'_{RMS} and v'_{RMS} and the Reynolds stress $-\overline{u'v'}$. The figure shows that two regions can be distinguished as far as different levels of average uncertainty estimates are concerned (except for V where the average uncertainty is fairly constant throughout).

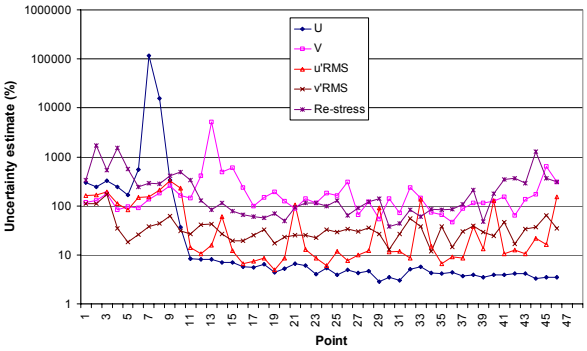

Figure C.11. Uncertainty estimates for the measured quantities

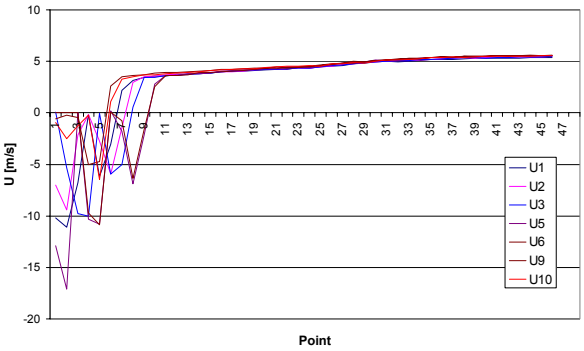

Figure C.12. U-profiles for the uncertainty sample

A first region is related to the erroneous in- and near-wall measurements which have been neglected for the analysis. It is felt that generally the first measurements were taken in the wall, where large negative U velocities were erroneously picked up, as shown in Figure C.12. This bias would persist for the very first near-wall measurements so that the first retained measurements were generally outside the buffer layer ($y^+ > 30$). This was actually not typical for the overall measurements, but did occur to a less pronounced extent over the CFR surface.

The uncertainty in the second region, which was retained for the calculation of the boundary-layer parameters, indicate that the uncertainty levels for U, V, u'_{RMS}, v'_{RMS} and $-\overline{u'v'}$ are 4.7, 26.6, 29.4, 29.9 and 144.2% respectively.

The analysis methods were carried out ten times for each replicate measured profile in order to determine the uncertainty on the various parameters. Table C-5 presents the uncertainties on the parameters with $\alpha = 0.05$ using the t-value of 2.447 for 95% confidence and 6 degrees of freedom.

Table C-5. Uncertainty estimates for the boundary-layer parameters

	Average	S (StDev)	2.45S (%)
Ue	5.51	0.07	2.90
Reθ	23906.32	1036.91	10.61
δ	42.20	3.06	17.71
δ1	4.38	0.26	14.36
θ	3.40	0.18	12.72
H	1.29	0.048	9.19
Tu	0.0508	0.0057	27.60
Reδ1	30744.90	1429.25	11.38
ε	-0.22	0.29	-321.96
Uτ (Clauser)	0.1707	0.0090	12.91
cf	0.00193	0.00020	25.74
ΔU+	-3.36	1.68	-122.28
Uτ (stress)	0.2003	0.0035	4.32
cf	0.00264	0.00005	4.76
ΔU+	1.16	0.26	55.54
Uτ (Hama)	0.1943	0.0031	3.96
cf	0.00249	0.00007	6.67
Π	0.23	0.03	34.70
ΔU+	0.51	0.32	155.69

The uncertainty on derived parameters was calculated by the uncertainty propagation method as specified in Coleman and Steele (1999, Chapter 4). For example, the uncertainty (in %) on U_e/U_τ was calculated as the square root of sum of the uncertainties in U_e and U_τ (as obtained with the Hama method) squared. The uncertainty was thus determined at 4.9%.

Appendix D. Boundary-layer plots

This Appendix contains plots of the boundary-layer data measured in the Emerson Cavitation Tunnel and described in Section 5.2. Section D.1 presents the mean velocity profiles in inner coordinates, Section D.2 the turbulence intensity profiles, Section D.3 the Reynolds stress profiles and Section D.4 presents plots of the velocity spectra.

D.1 Mean velocity profiles in inner coordinates

Uncertainty in these figures over the middle region (cf. Appendix C.1) for U^+: ±1.72% for the STEEL surface, ±1.94% for the rough surfaces.

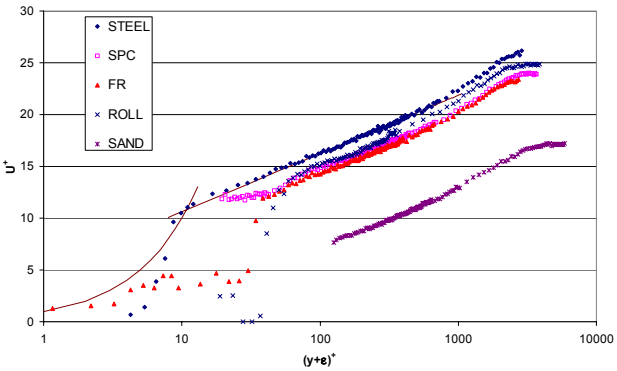

Figure D.1. Comparative velocity profile at 2pos1.

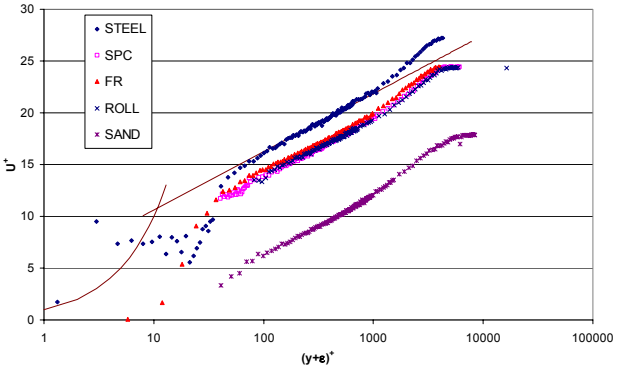

Figure D.2. Comparative velocity profile at 3pos1.

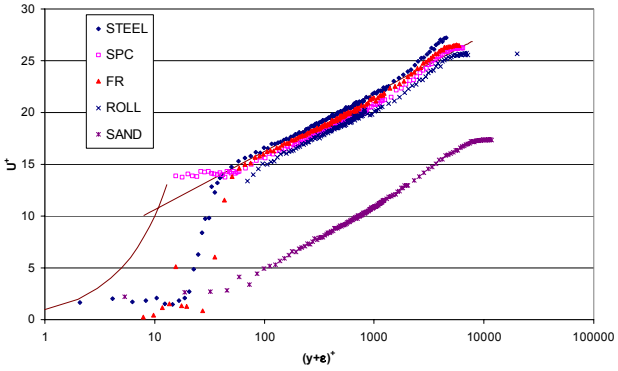

Figure D.3. Comparative velocity profile at 4pos1.

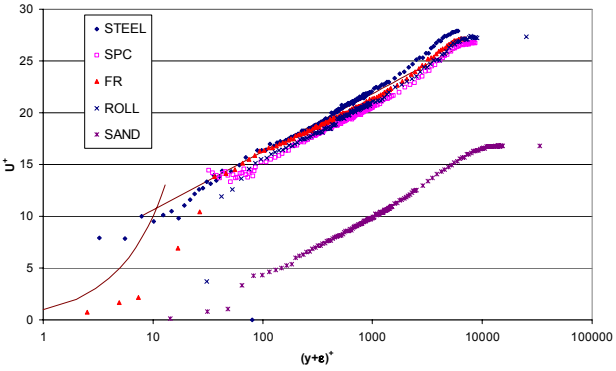

Figure D.4. Comparative velocity profile at 5pos1.

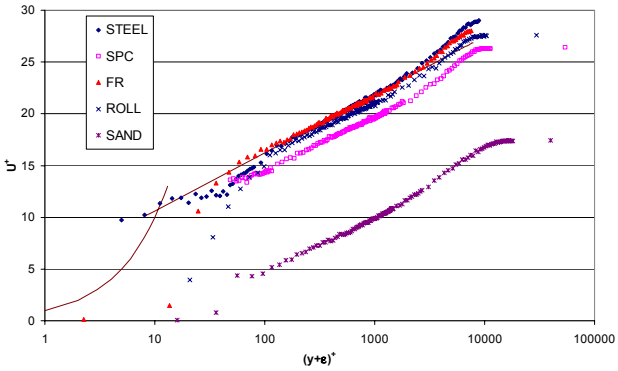

Figure D.5. Comparative velocity profile at 6pos1.

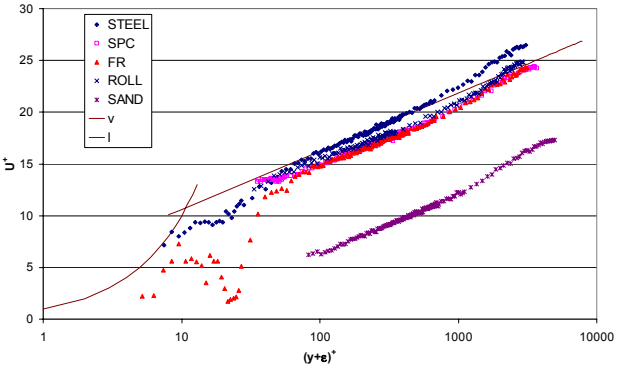

Figure D.6. Comparative velocity profile at 2pos3.

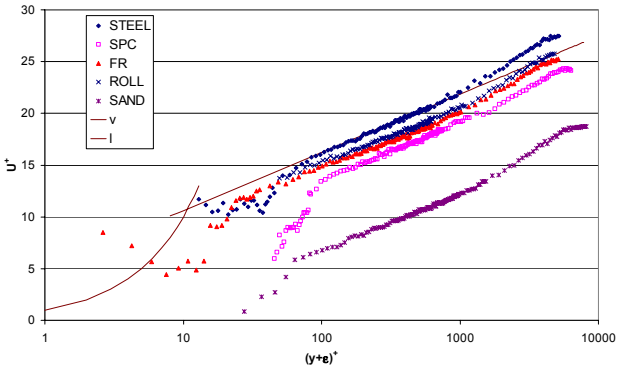

Figure D.7. Comparative velocity profile at 3pos3.

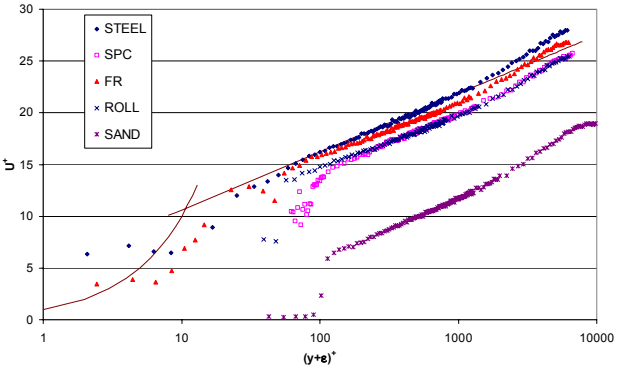

Figure D.8. Comparative velocity profile at 4pos3.

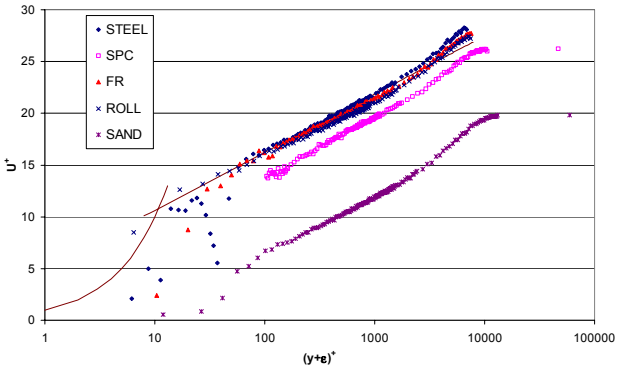

Figure D.9. Comparative velocity profile at 5pos3.

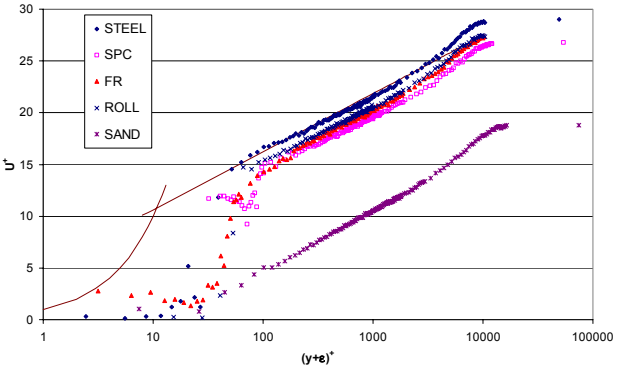

Figure D.10. Comparative velocity profile at 6pos3.

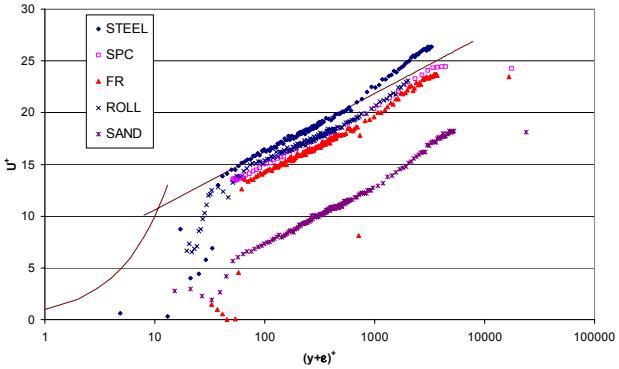

Figure D.11. Comparative velocity profile at 2pos5.

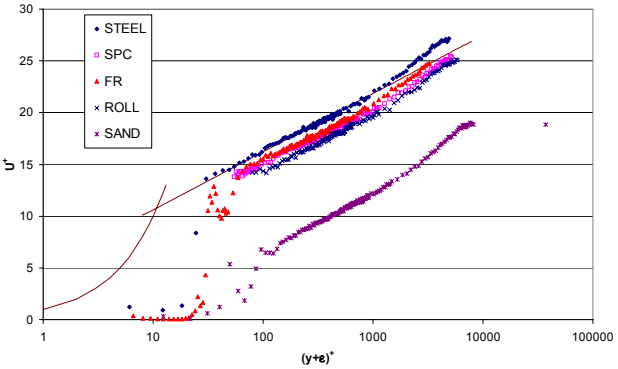

Figure D.12. Comparative velocity profile at 3pos5.

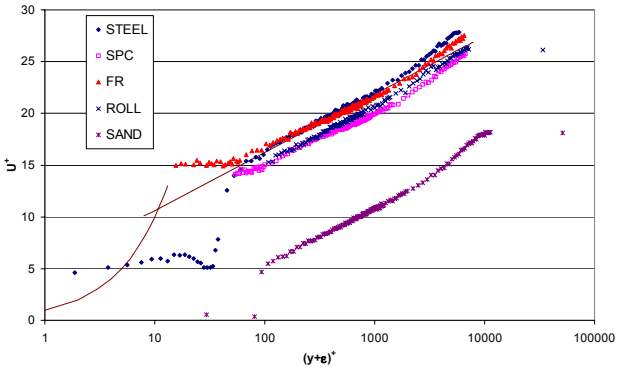

Figure D.13. Comparative velocity profile at 4pos5.

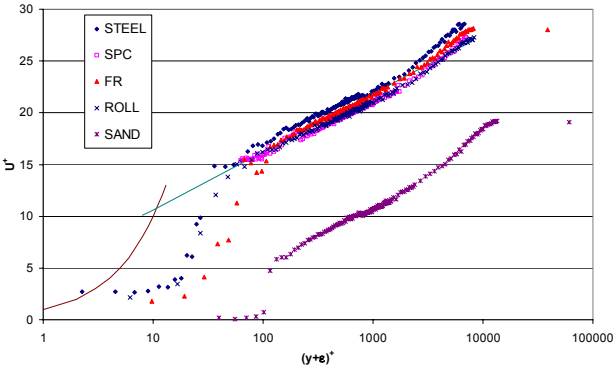

Figure D.14. Comparative velocity profile at 5pos5.

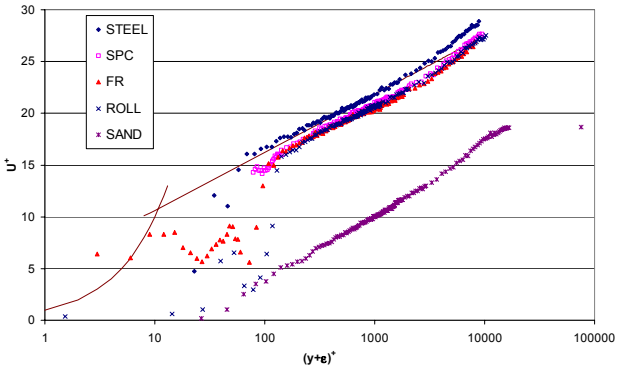

Figure D.15. Comparative velocity profile at 6pos5.

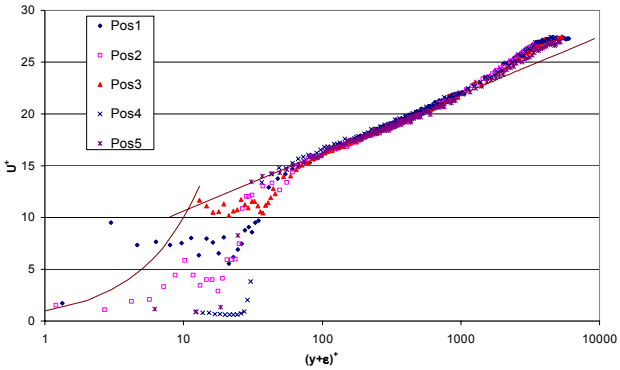

Figure D.16. STEEL profiles at 3m/s.

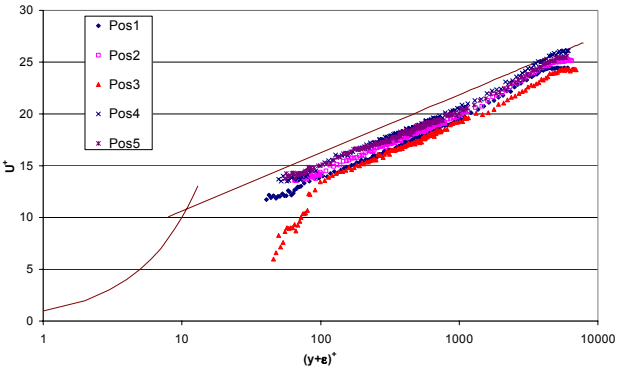

Figure D.17. SPC profiles at 3m/s.

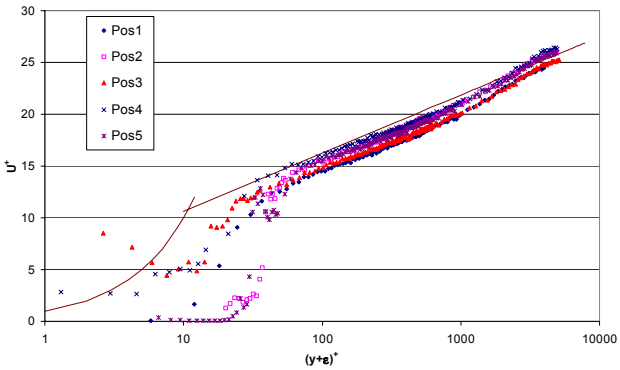

Figure D.18. FR profiles at 3m/s.

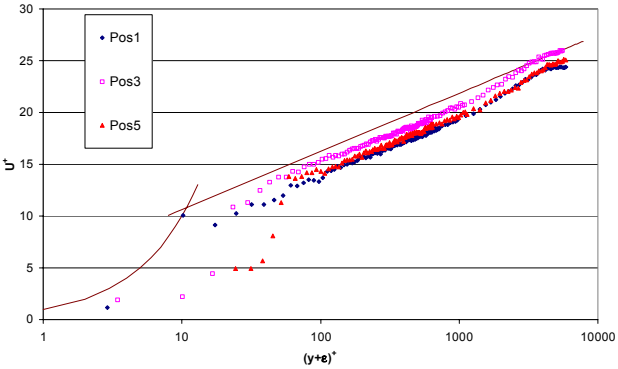

Figure D.19. ROLL profiles at 3m/s.

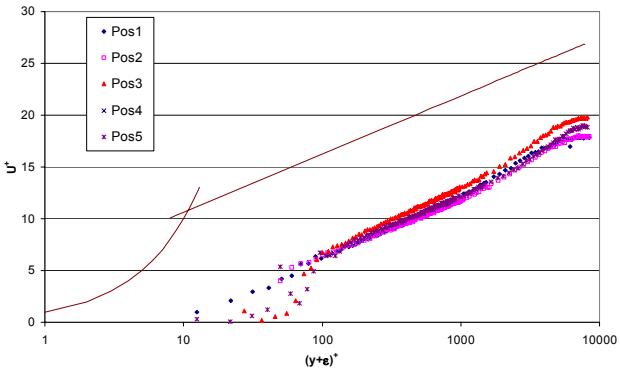

Figure D.20. SAND profiles at 3m/s.

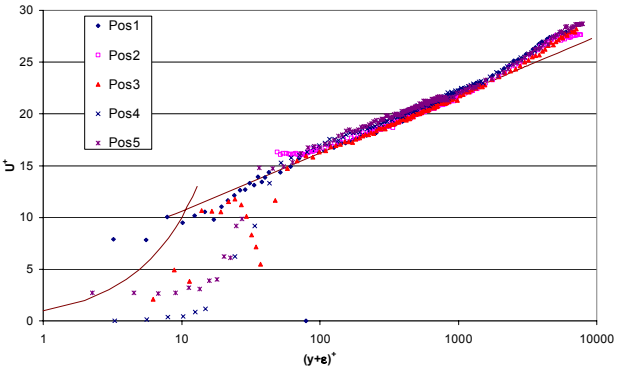

Figure D.21. STEEL profiles at 5m/s.

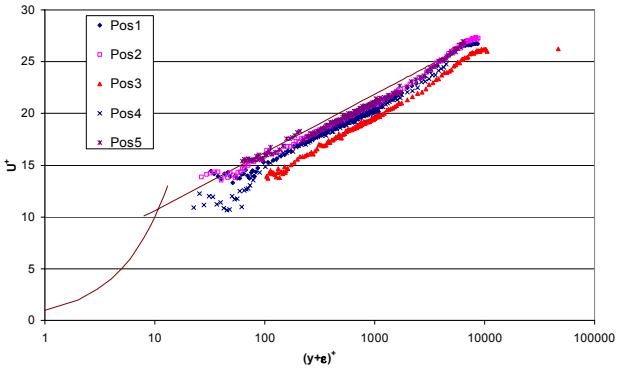

Figure D.22. SPC profiles at 5m/s.

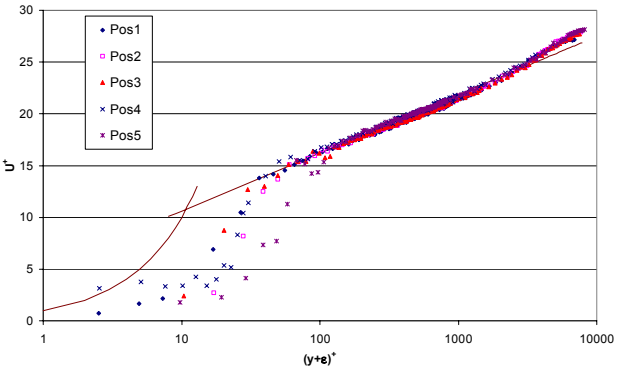

Figure D.23. FR profiles at 5m/s.

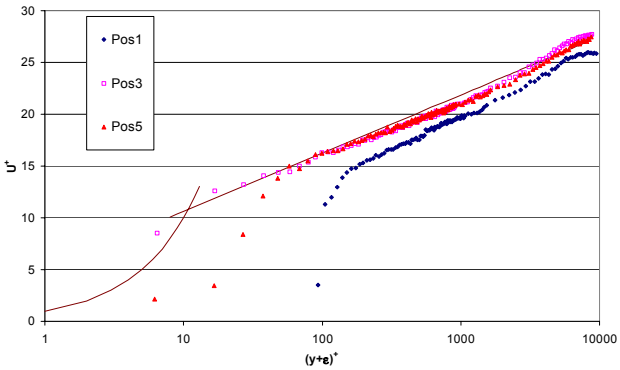

Figure D.24. ROLL profiles at 5m/s.

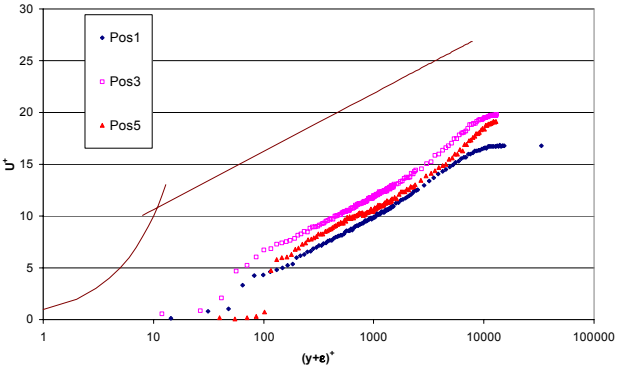

Figure D.25. SAND profiles at 5m/s.

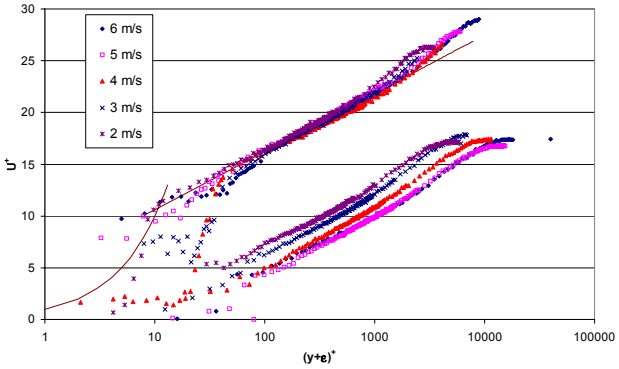

Figure D.26. STEEL and SAND profiles at position 1.

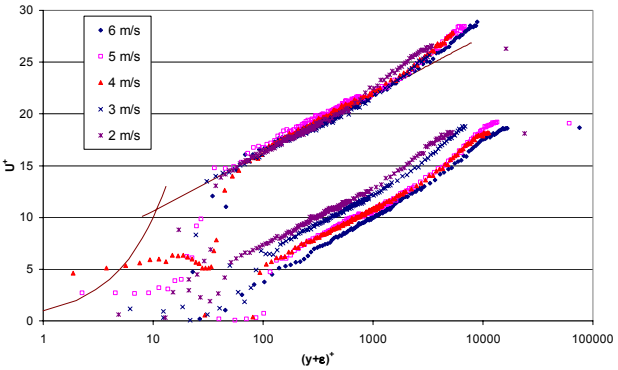

Figure D.27. STEEL and SAND profiles at position 5.

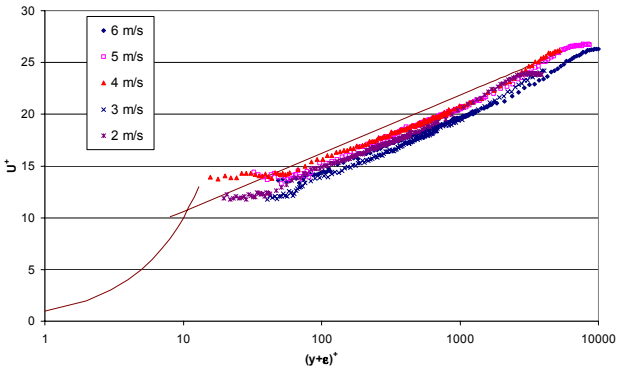

Figure D.28. SPC profiles at position 1.

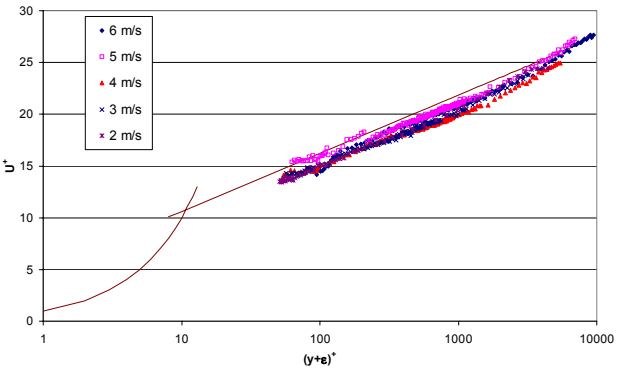

Figure D.29. SPC profiles at position 5.

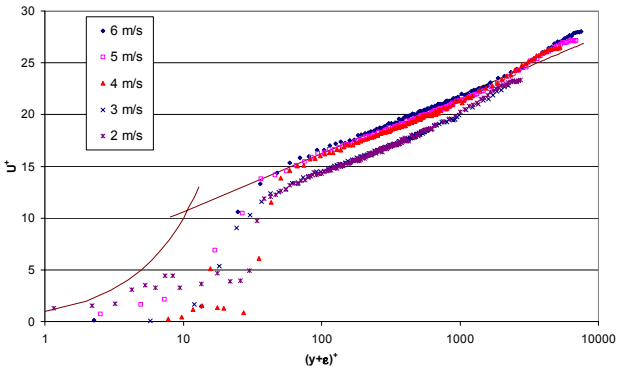

Figure D.30. FR profiles at position 1.

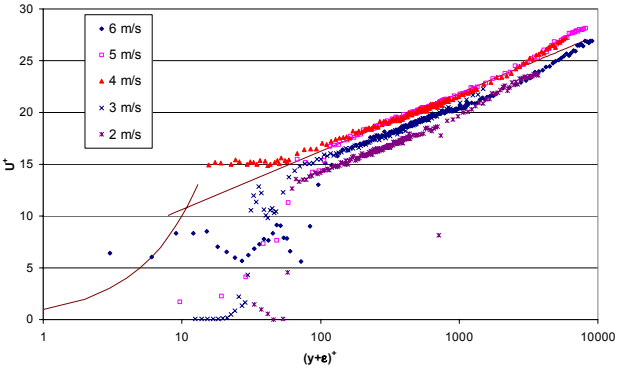

Figure D.31. FR profiles at position 5.

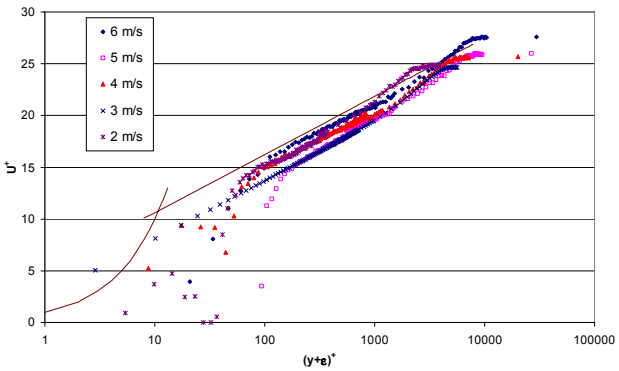

Figure D.32. ROLL profiles at position 1.

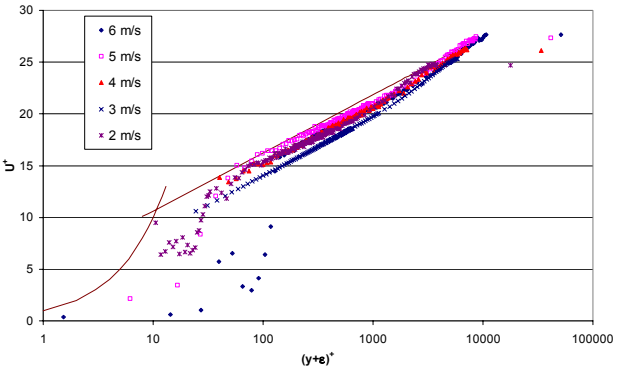

Figure D.33. ROLL profiles at position 5.

D.2 Turbulence intensity profiles

Uncertainty in these figures over the middle region (cf. Appendix C.1) for $u'_{RMS}{}^{+}$: ±4.54% for the STEEL surface, ±4.66% for the rough surfaces, uncertainty in $v'_{RMS}{}^{+}$: ±3.84% for the STEEL surface, ±4.0% for the rough surfaces.

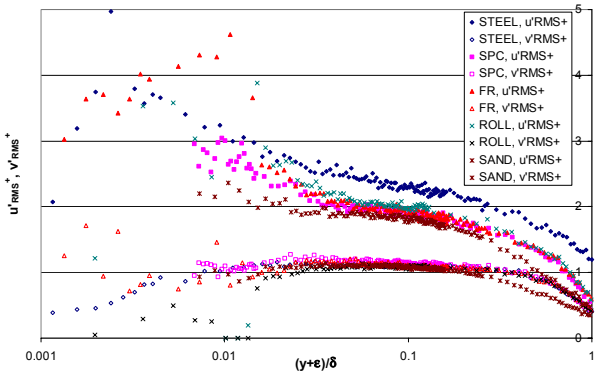

Figure D.34. Turbulence intensities at 2pos1.

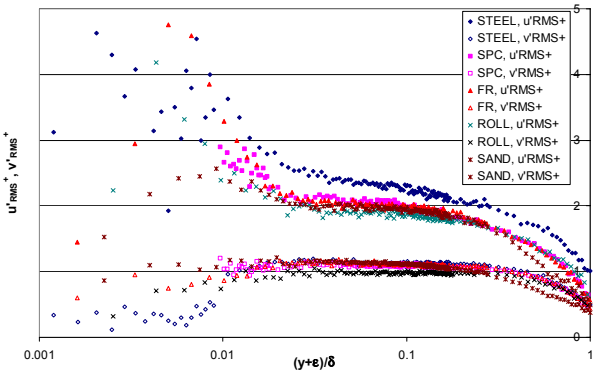

Figure D.35. Turbulence intensities at 3pos1.

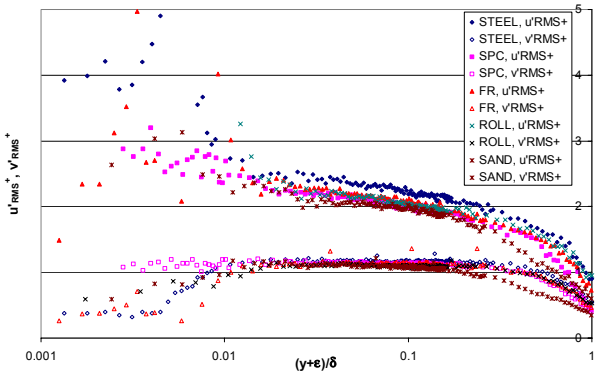

Figure D.36. Turbulence intensities at 4pos1.

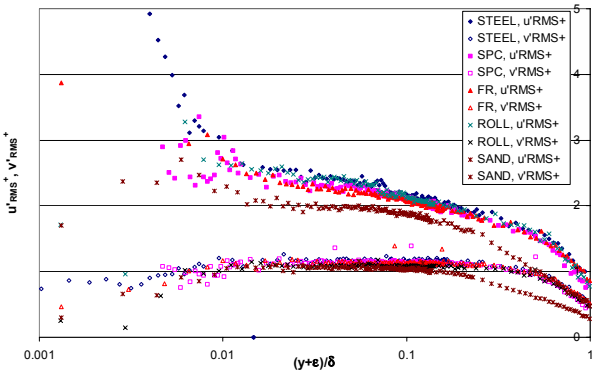

Figure D.37. Turbulence intensities at 5pos1.

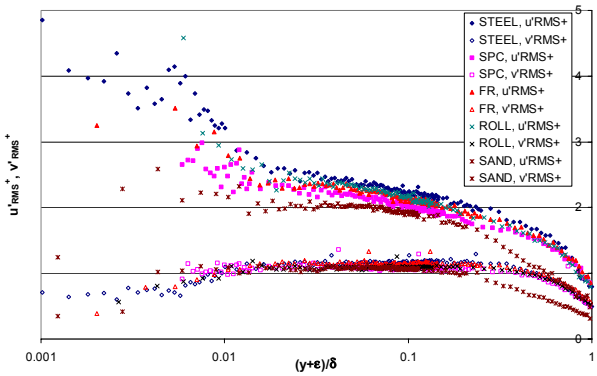

Figure D.38. Turbulence intensities at 6pos1.

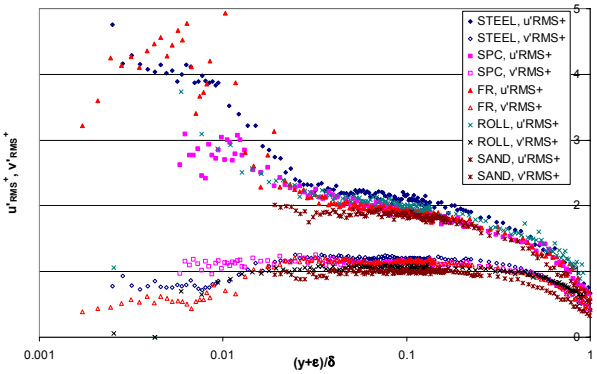

Figure D.39. Turbulence intensities at 2pos3.

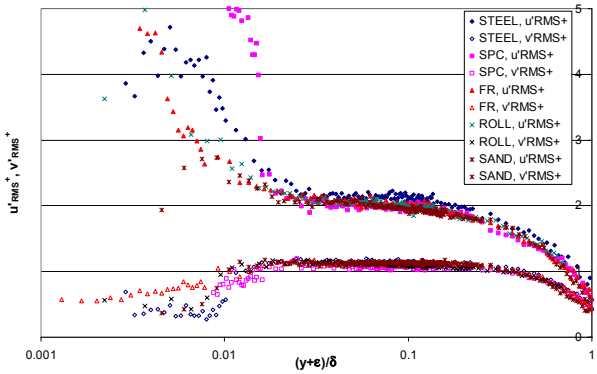

Figure D.40. Turbulence intensities at 3pos3.

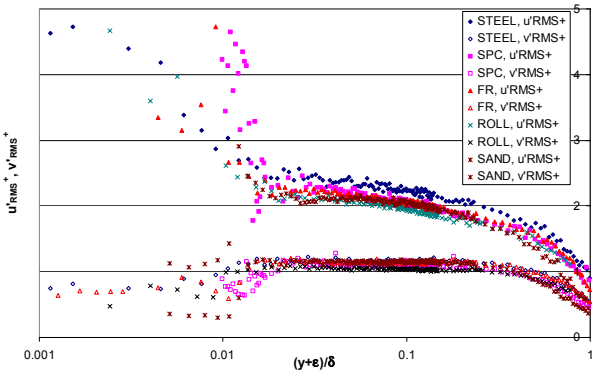

Figure D.41. Turbulence intensities at 4pos3.

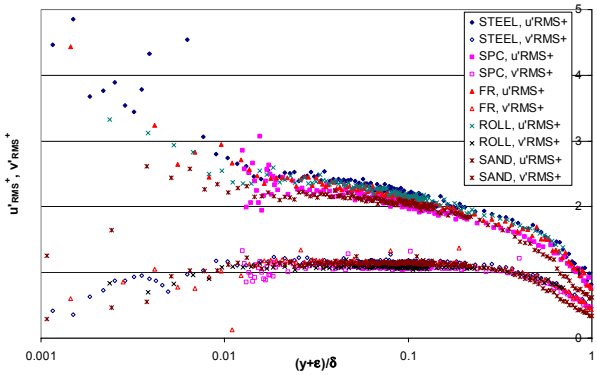

Figure D.42. Turbulence intensities at 5pos3.

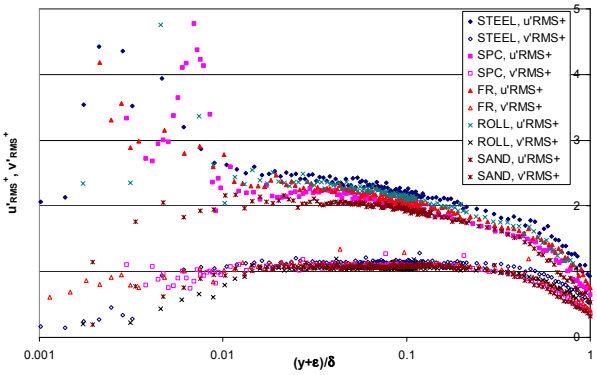

Figure D.43. Turbulence intensities at 6pos3.

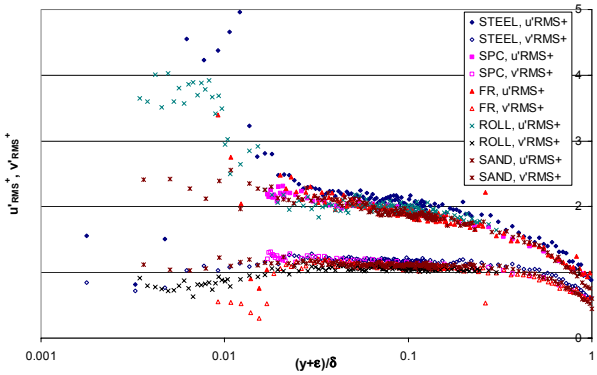

Figure D.44. Turbulence intensities at 2pos5.

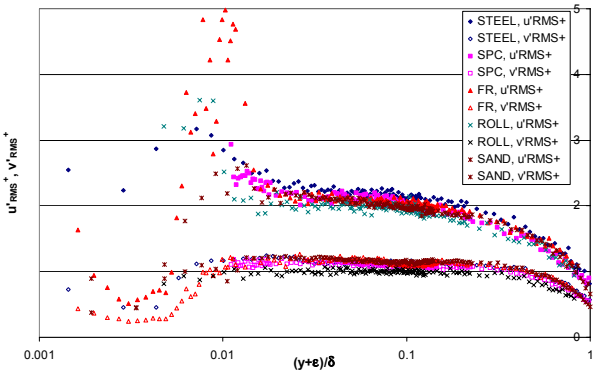

Figure D.45. Turbulence intensities at 3pos5.

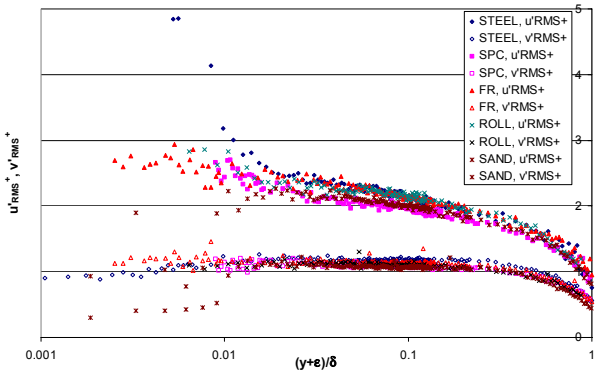

Figure D.46. Turbulence intensities at 4pos5.

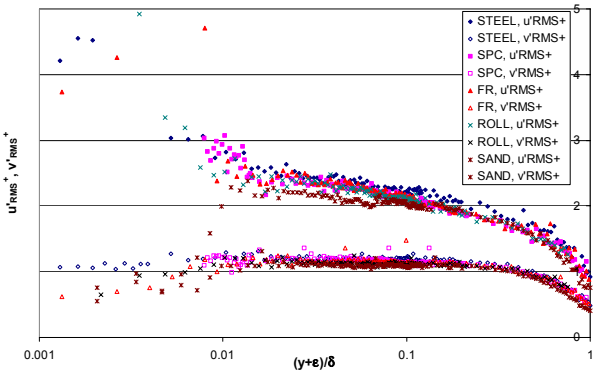

Figure D.47. Turbulence intensities at 5pos5.

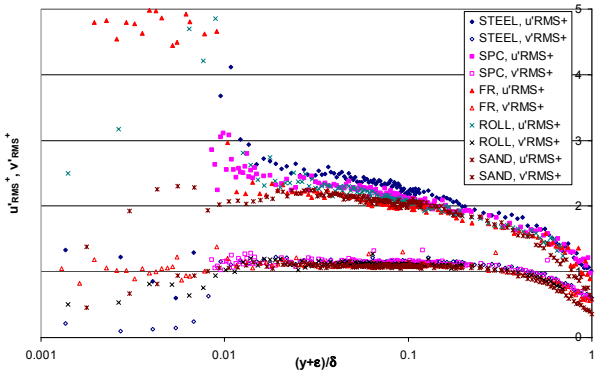

Figure D.48. Turbulence intensities at 6pos5.

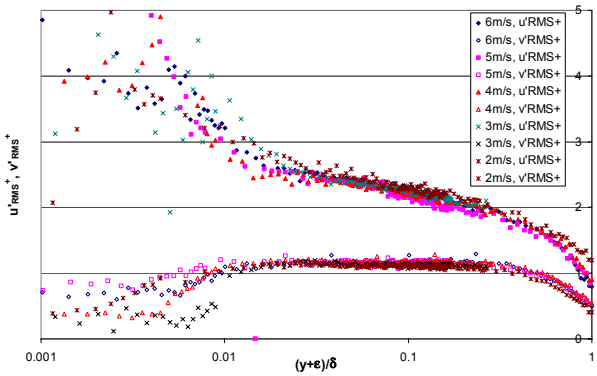

Figure D.49. STEEL turbulence intensities at position 1.

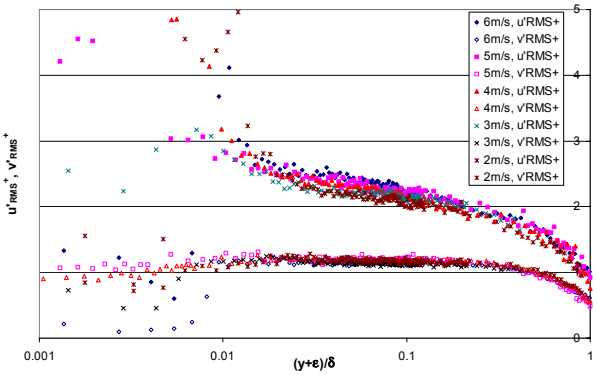

Figure D.50. STEEL turbulence intensities at position 5.

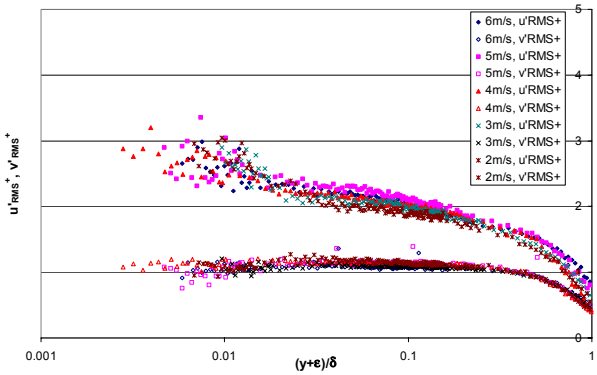

Figure D.51. SPC turbulence intensities at position 1.

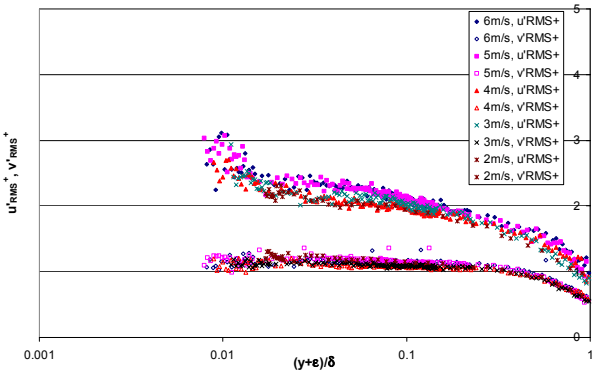

Figure D.52. SPC turbulence intensities at position 5.

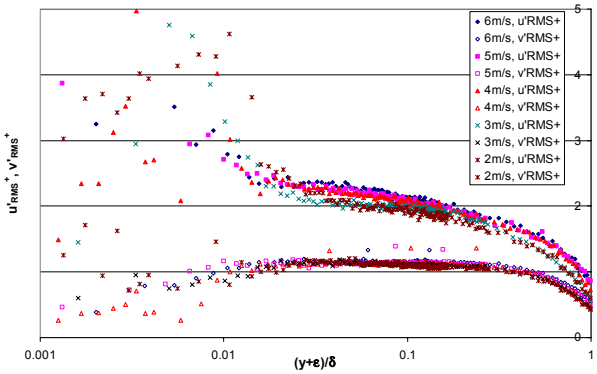

Figure D.53. FR turbulence intensities at position 1.

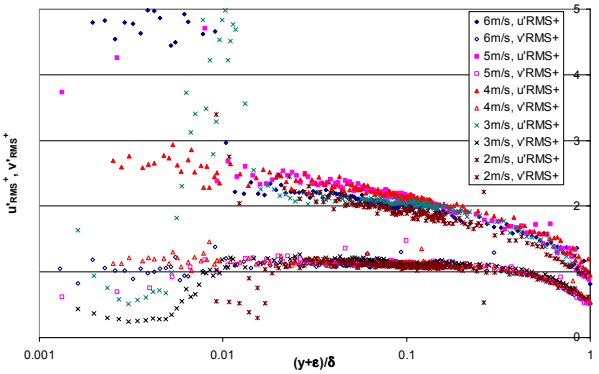

Figure D.54. FR turbulence intensities at position 5.

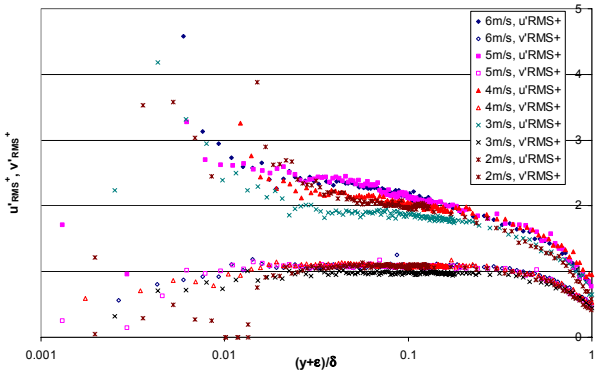

Figure D.55. ROLL turbulence intensities at position 1.

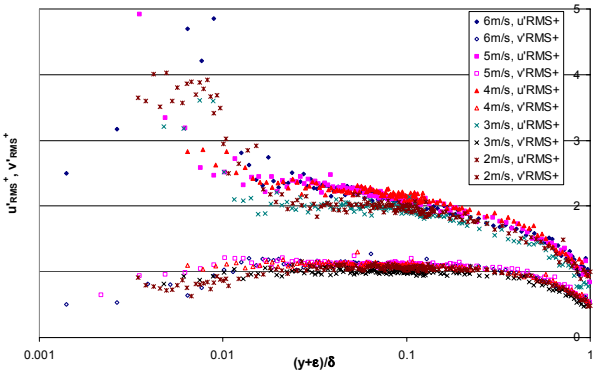

Figure D.56. ROLL turbulence intensities at position 5.

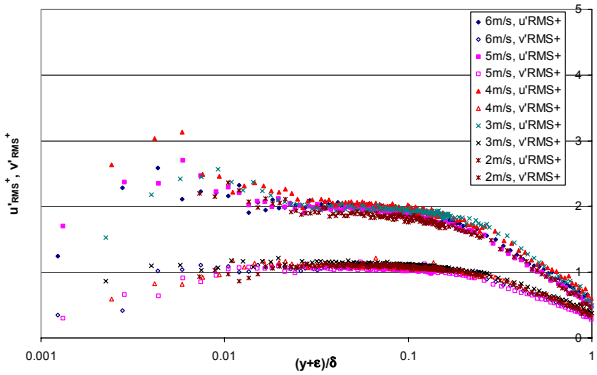

Figure D.57. SAND turbulence intensities at position 1.

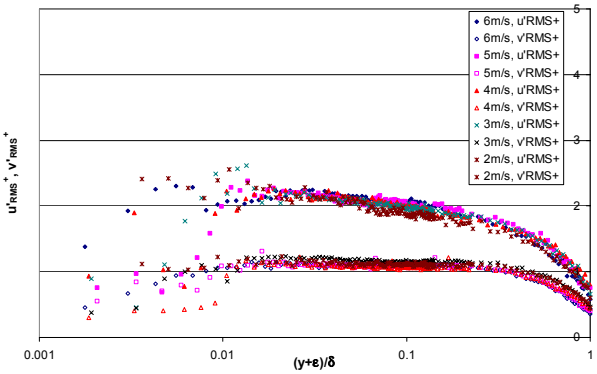

Figure D.58. SAND turbulence intensities at position 5.

D.3 Reynolds stress profiles

Uncertainty in these figures over the middle region (cf. Appendix C.1) for $-u'v'^{+}$: ±12.14% for the STEEL surface, ±11.25% for the rough surfaces.

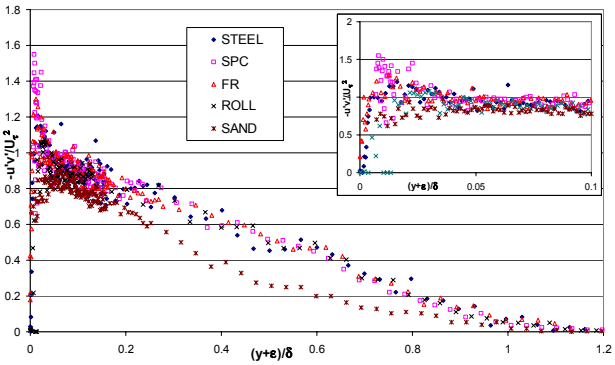

Figure D.59. Reynolds stress profiles at 2POS1.

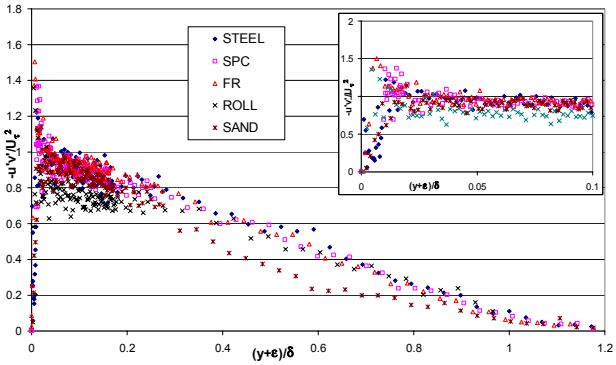

Figure D.60. Reynolds stress profiles at 3POS1.

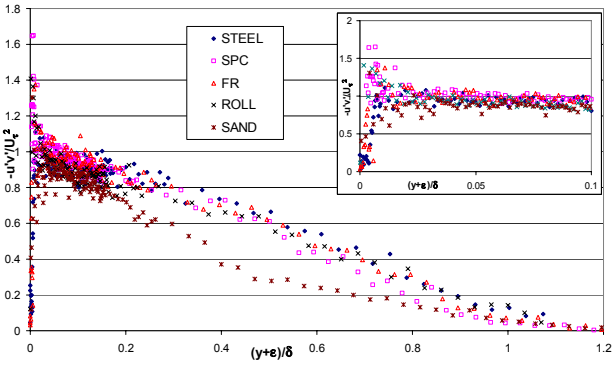

Figure D.61. Reynolds stress profiles at 4POS1.

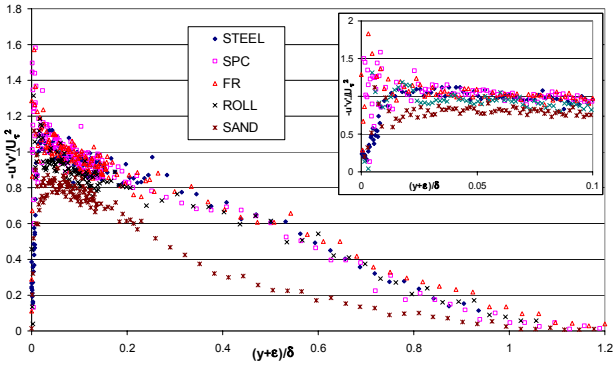

Figure D.62. Reynolds stress profiles at 5POS1.

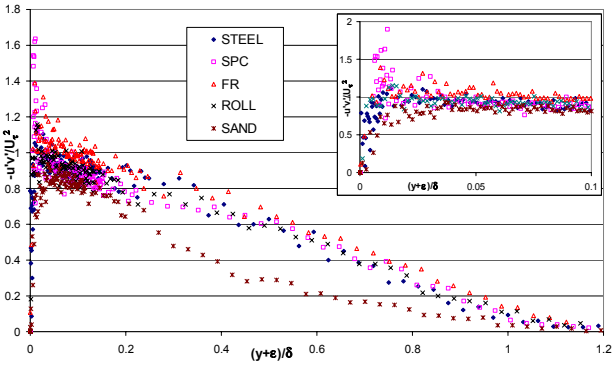

Figure D.63. Reynolds stress profiles at 6POS1.

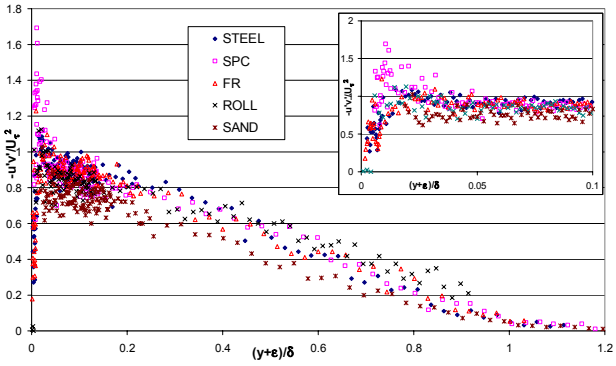

Figure D.64. Reynolds stress profiles at 2POS3.

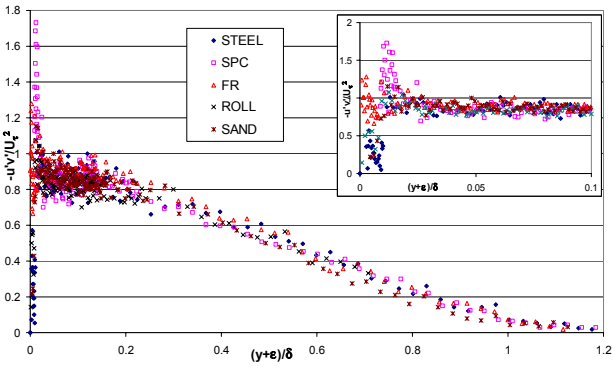

Figure D.65. Reynolds stress profiles at 3POS3.

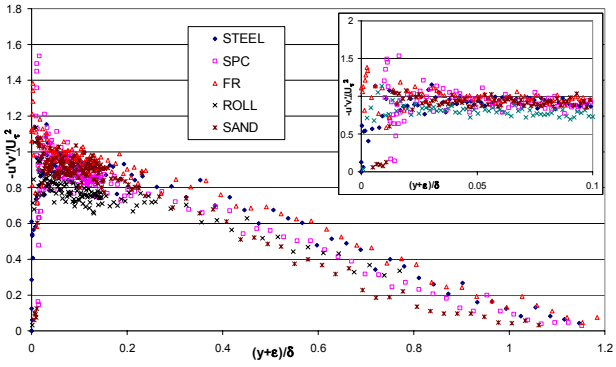

Figure D.66. Reynolds stress profiles at 4POS3.

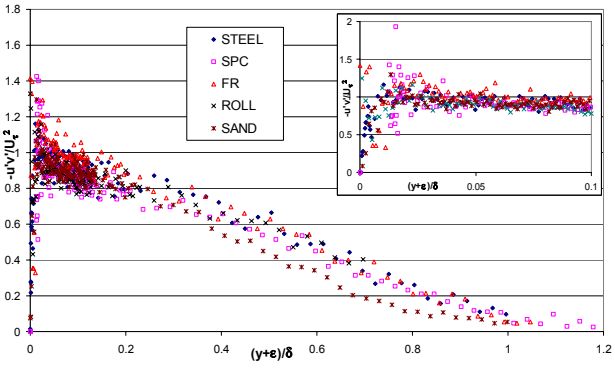

Figure D.67. Reynolds stress profiles at 5POS3.

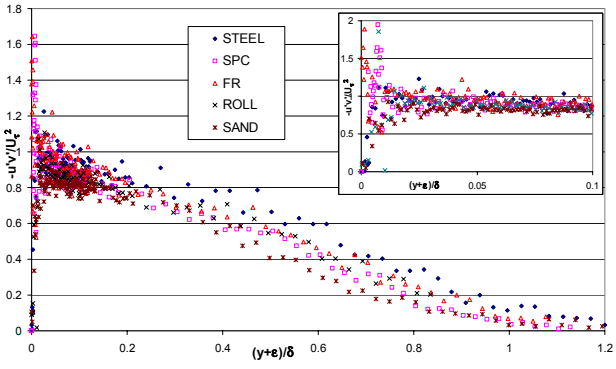

Figure D.68. Reynolds stress profiles at 6POS3.

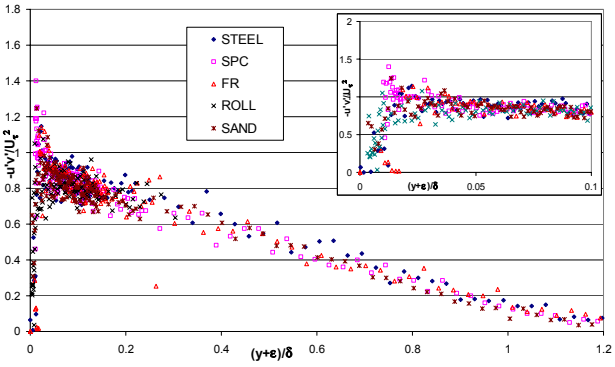

Figure D.69. Reynolds stress profiles at 2POS5.

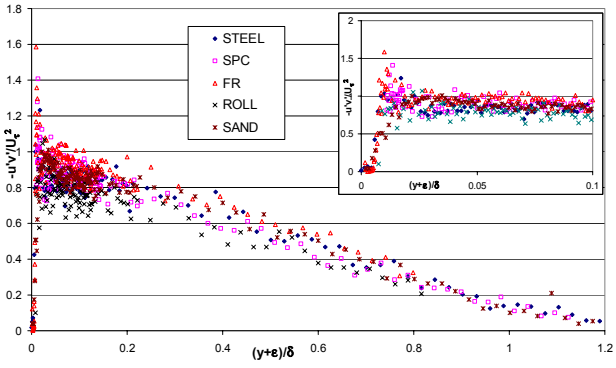

Figure D.70. Reynolds stress profiles at 3POS5.

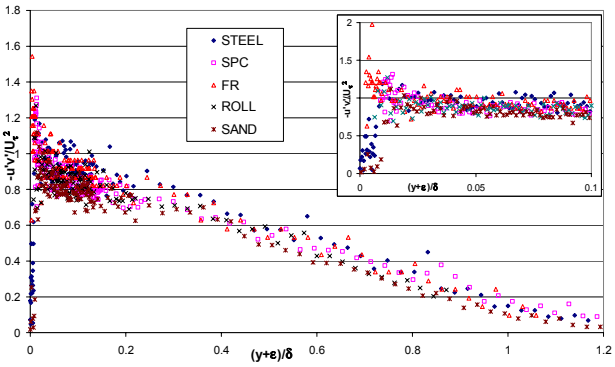

Figure D.71. Reynolds stress profiles at 4POS5.

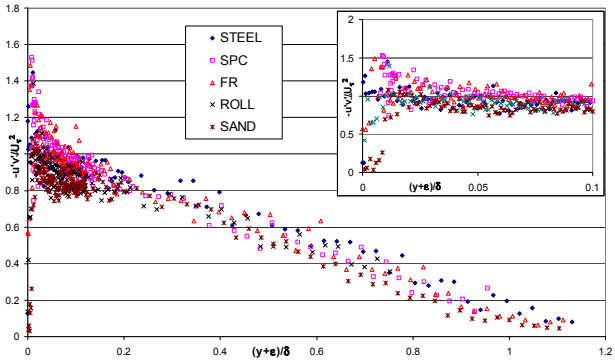

Figure D.72. Reynolds stress profiles at 5POS5.

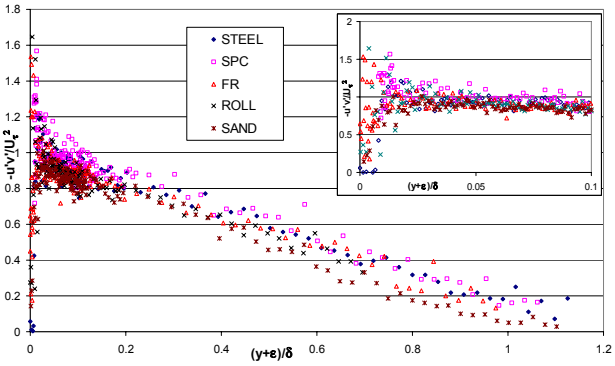

Figure D.73. Reynolds stress profiles at 6POS5.

D.4 Spectra

Uncertainties at $y/\delta = 0.05$ for $E_u(k)/u'^2$: ±32.26%, for $E_v(k)/v'^2$: ±35.37%, and at $y/\delta = 0.8$ for $E_u(k)/u'^2$: ±29.57%, for $E_v(k)/v'^2$: ±31.92% (cf. Appendix C.1).

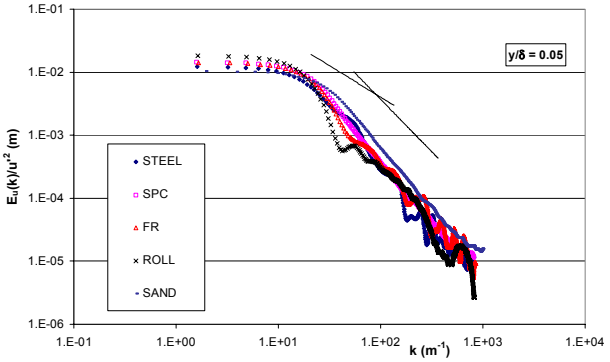

Figure D.74. Comparative spectra $E_u(k)/u'^2$ for 2pos1 at $y/\delta = 0.05$

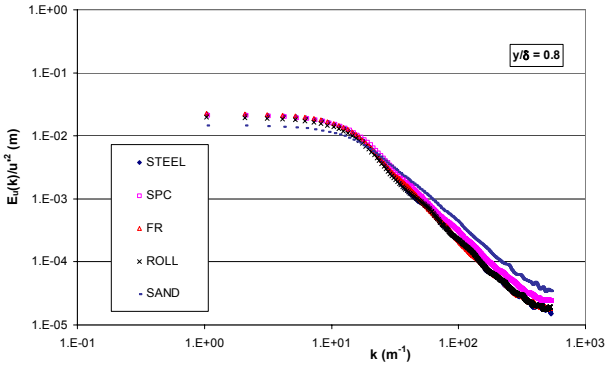

Figure D.75. Comparative spectra $E_u(k)/u'^2$ for 2pos1 at $y/\delta = 0.8$

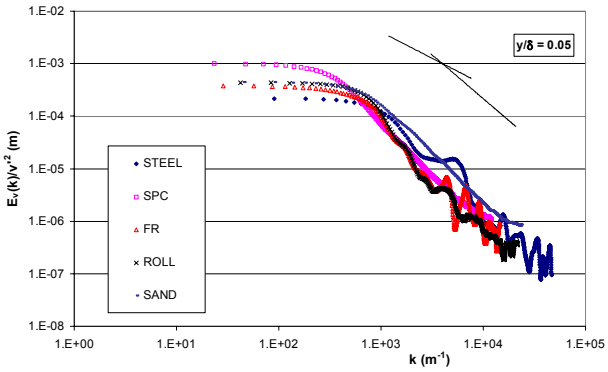

Figure D.76. Comparative spectra $E_v(k)/v'^2$ for 2pos1 at $y/\delta = 0.05$

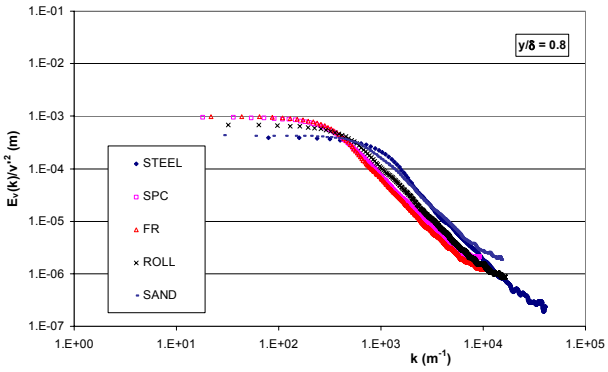

Figure D.77. Comparative spectra $E_v(k)/v'^2$ for 2pos1 at $y/\delta = 0.8$

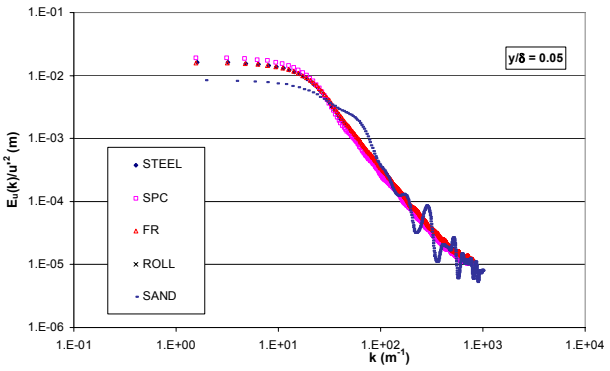

Figure D.78. Comparative spectra $E_u(k)/u'^2$ for 2pos3 at $y/\delta = 0.05$

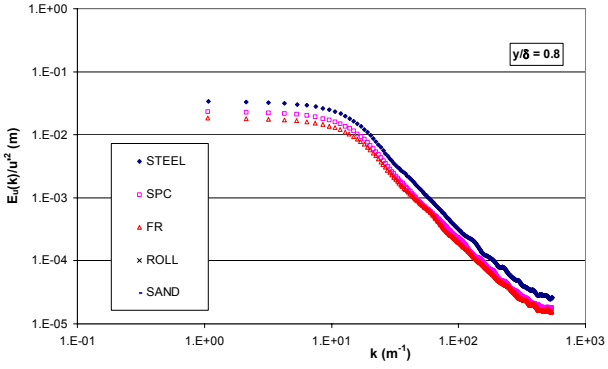

Figure D.79. Comparative spectra $E_u(k)/u'^2$ for 2pos3 at $y/\delta = 0.8$

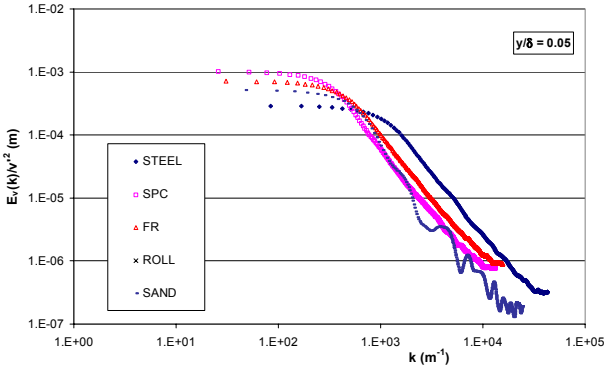

Figure D.80. Comparative spectra $E_v(k)/v'^2$ for 2pos3 at y/δ = 0.05

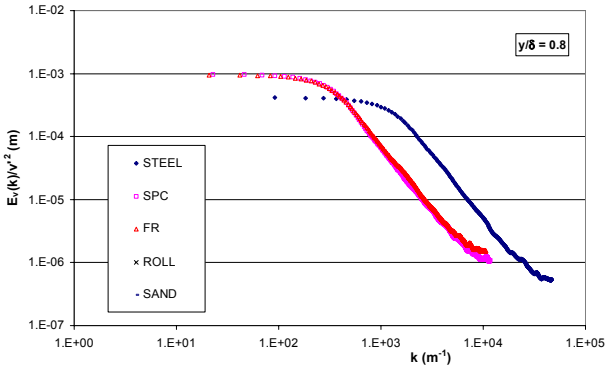

Figure D.81. Comparative spectra $E_v(k)/v'^2$ for 2pos3 at y/δ = 0.8

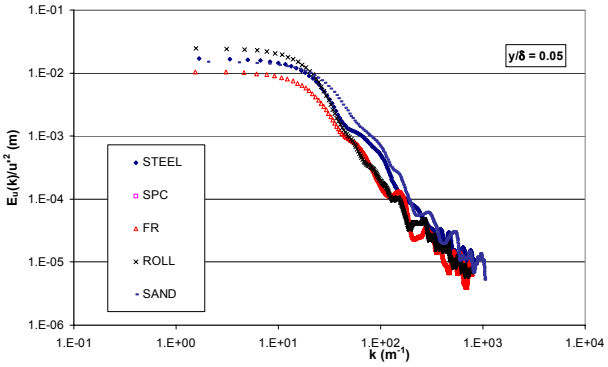

Figure D.82. Comparative spectra $E_u(k)/u'^2$ for 2pos5 at y/δ = 0.05

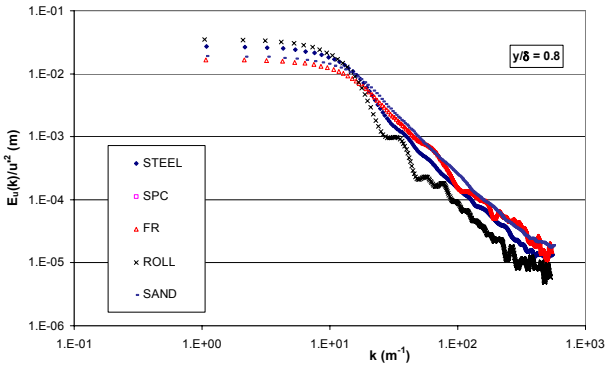

Figure D.83. Comparative spectra $E_u(k)/u'^2$ for 2pos5 at y/δ = 0.8

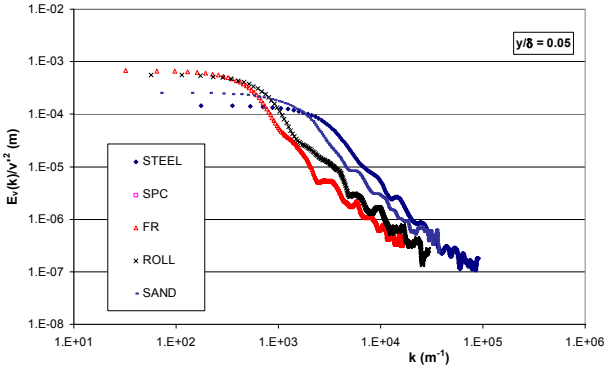

Figure D.84. Comparative spectra $E_v(k)/v'^2$ for 2pos5 at y/δ = 0.05

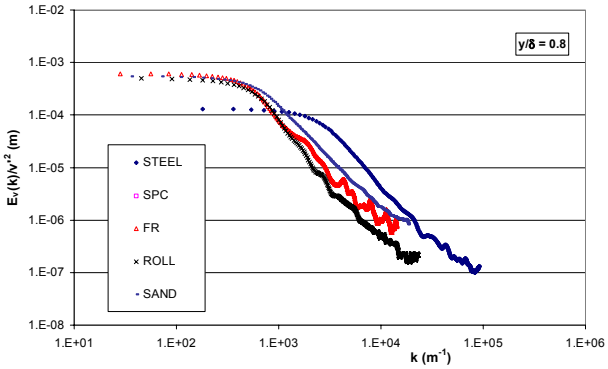

Figure D.85. Comparative spectra $E_v(k)/v'^2$ for 2pos5 at y/δ = 0.8

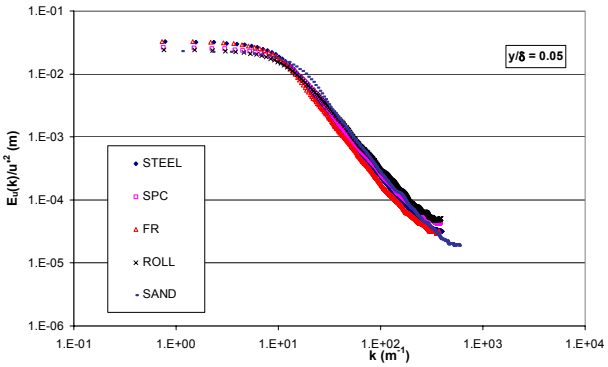

Figure D.86. Comparative spectra $E_u(k)/u'^2$ for 4pos1 at y/δ = 0.05

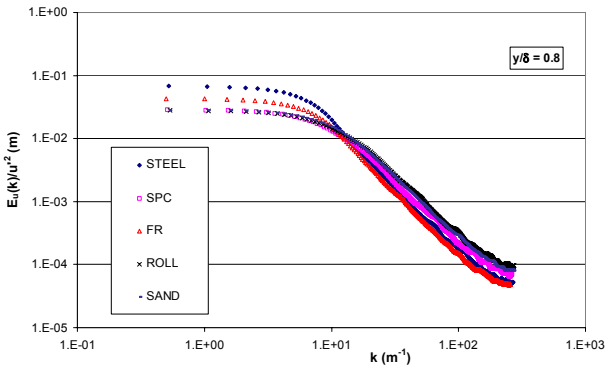

Figure D.87. Comparative spectra $E_u(k)/u'^2$ for 4pos1 at y/δ = 0.8

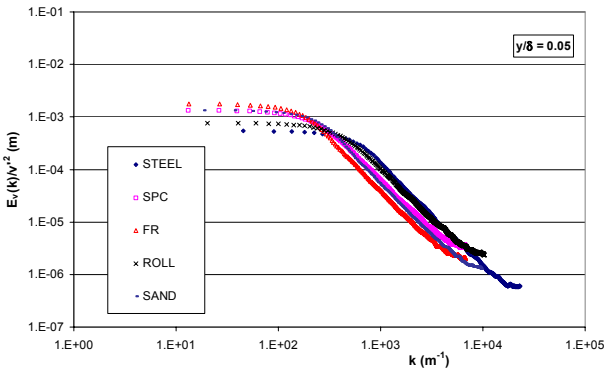

Figure D.88. Comparative spectra $E_v(k)/v'^2$ for 4pos1 at y/δ = 0.05

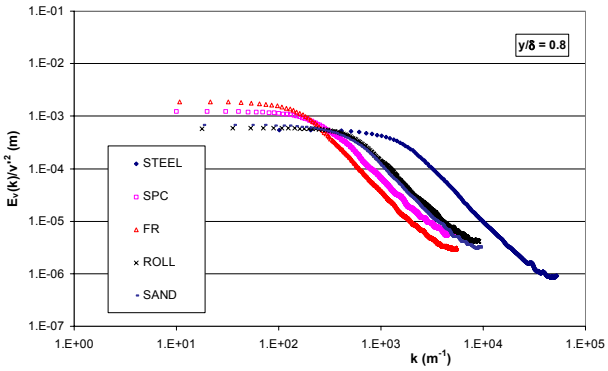

Figure D.89. Comparative spectra $E_v(k)/v'^2$ for 4pos1 at y/δ = 0.8

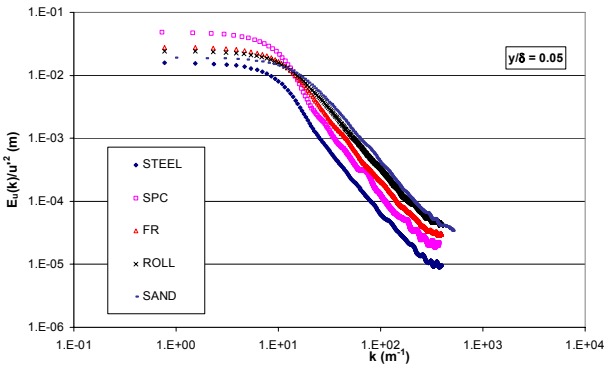

Figure D.90. Comparative spectra $E_u(k)/u'^2$ for 4pos3 at y/δ = 0.05

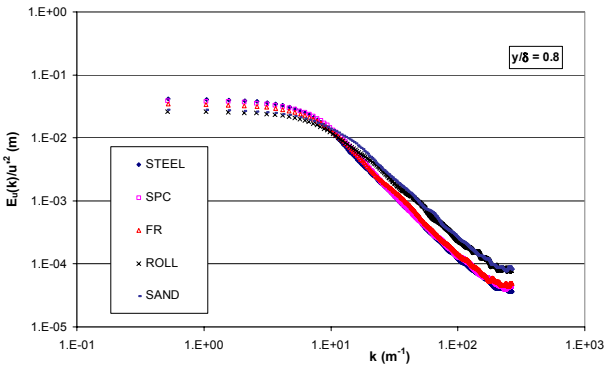

Figure D.91. Comparative spectra $E_u(k)/u'^2$ for 4pos3 at y/δ = 0.8

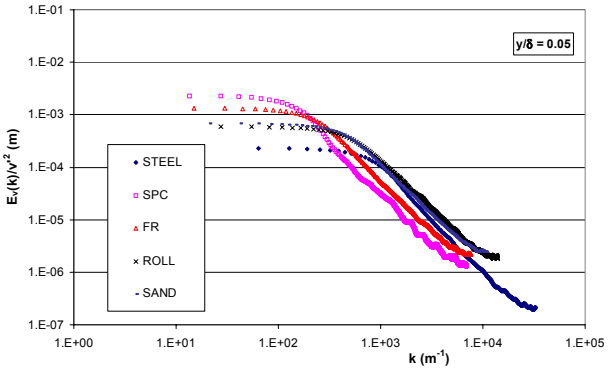

Figure D.92. Comparative spectra $E_v(k)/v'^2$ for 4pos3 at y/δ = 0.05

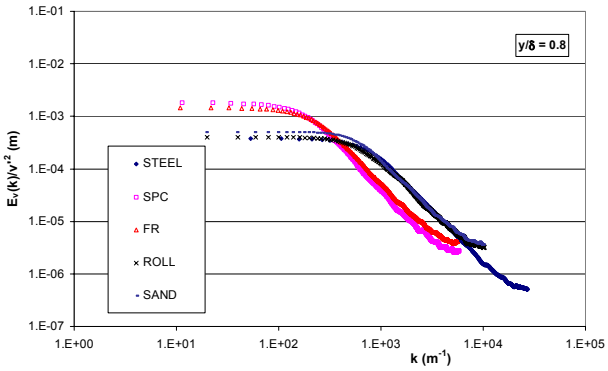

Figure D.93. Comparative spectra $E_v(k)/v'^2$ for 4pos3 at y/δ = 0.8

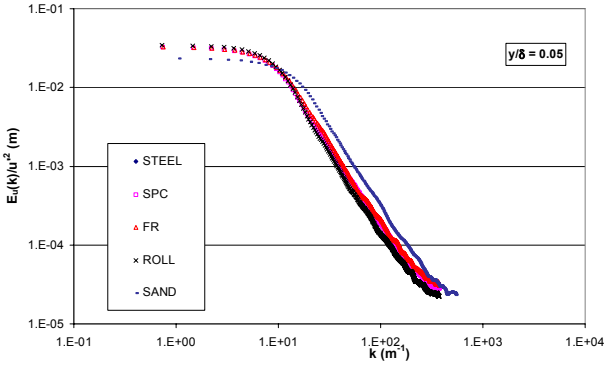

Figure D.94. Comparative spectra $E_u(k)/u'^2$ for 4pos5 at y/δ = 0.05

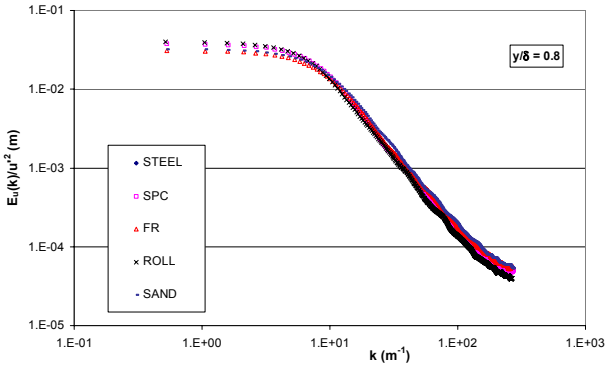

Figure D.95. Comparative spectra $E_u(k)/u'^2$ for 4pos5 at y/δ = 0.8

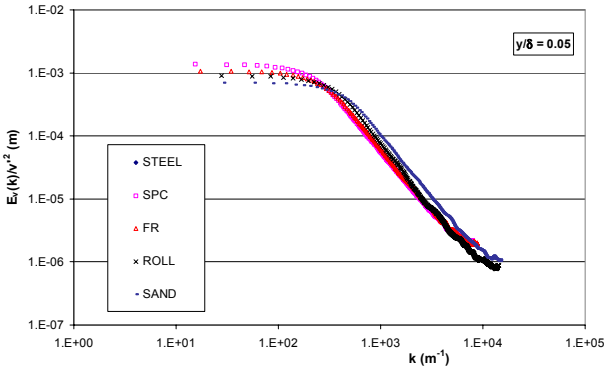

Figure D.96. Comparative spectra $E_v(k)/v'^2$ for 4pos5 at y/δ = 0.05

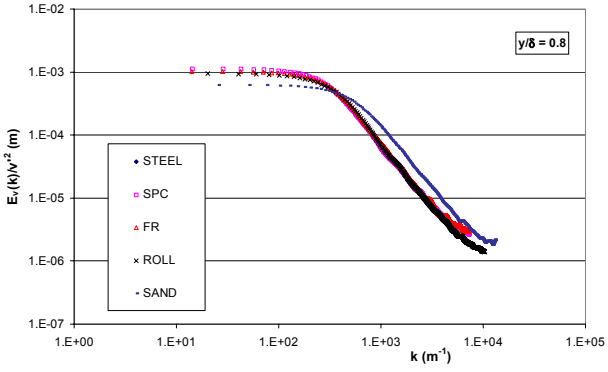

Figure D.97. Comparative spectra $E_v(k)/v'^2$ for 4pos5 at y/δ = 0.8

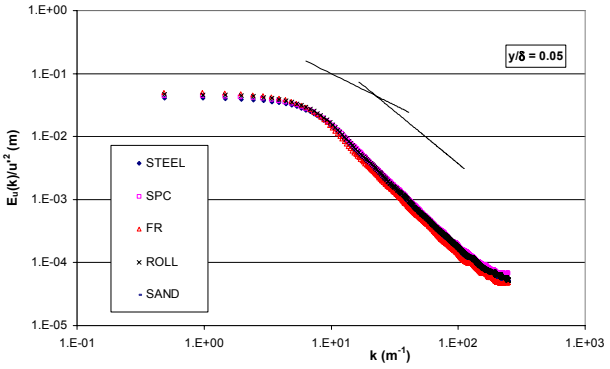

Figure D.98. Comparative spectra $E_u(k)/u'^2$ for 6pos1 at y/δ = 0.05

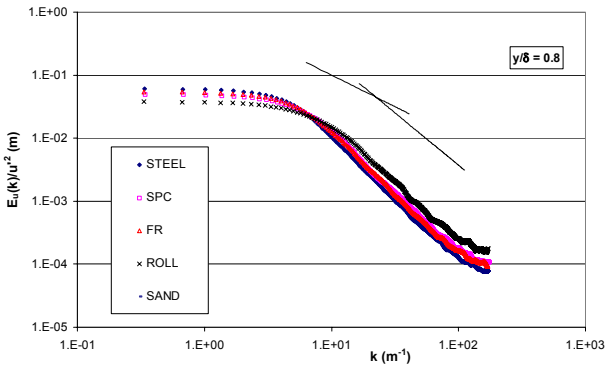

Figure D.99. Comparative spectra $E_u(k)/u'^2$ for 6pos1 at y/δ = 0.8

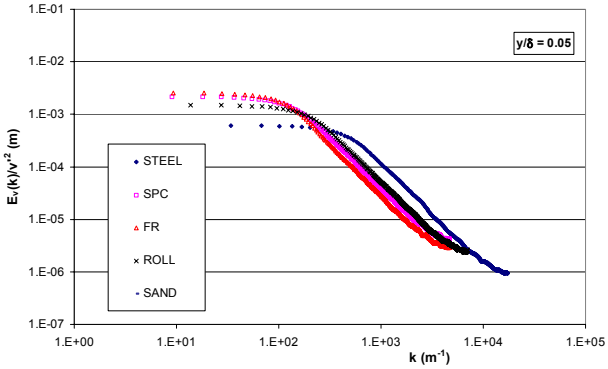

Figure D.100. Comparative spectra $E_v(k)/v'^2$ for 6pos1 at y/δ = 0.05

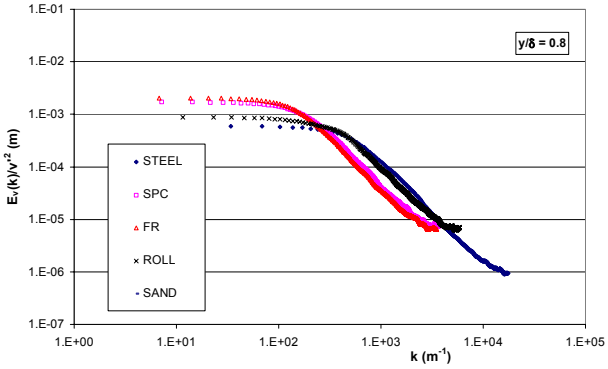

Figure D.101. Comparative spectra $E_v(k)/v'^2$ for 6pos1 at y/δ = 0.8

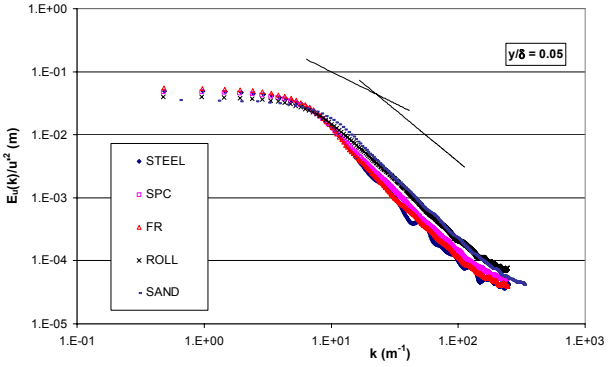

Figure D.102. Comparative spectra $E_u(k)/u'^2$ for 6pos3 at y/δ = 0.05

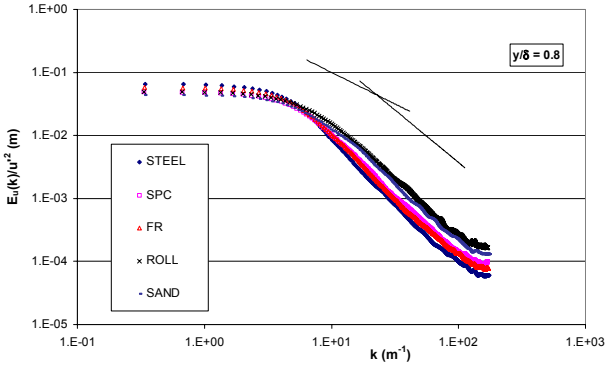

Figure D.103. Comparative spectra $E_u(k)/u'^2$ for 6pos3 at y/δ = 0.8

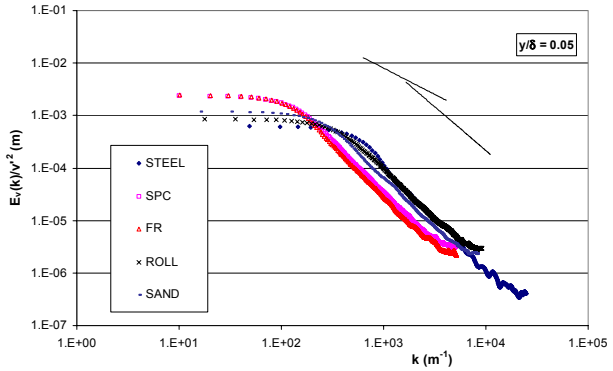

Figure D.104. Comparative spectra $E_v(k)/v'^2$ for 6pos3 at y/δ = 0.05

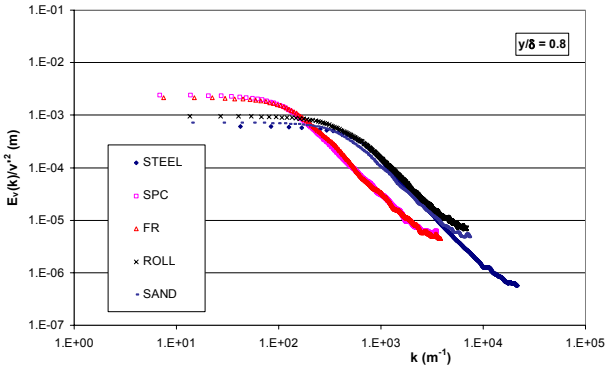

Figure D.105. Comparative spectra $E_v(k)/v'^2$ for 6pos3 at y/δ = 0.8

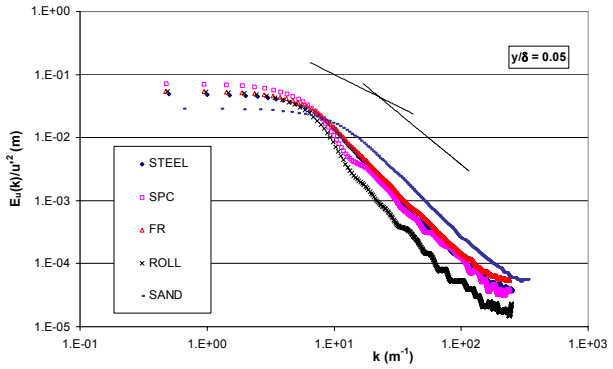

Figure D.106. Comparative spectra $E_u(k)/u'^2$ for 6pos5 at y/δ = 0.05

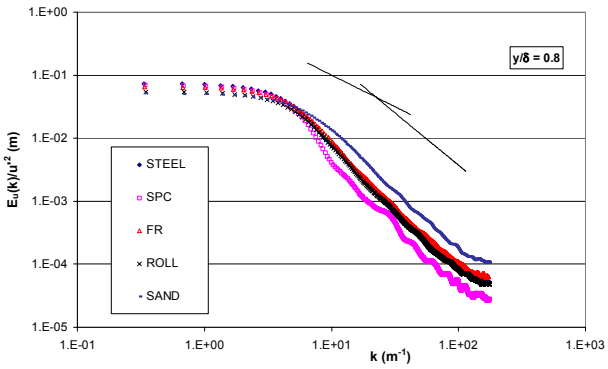

Figure D.107. Comparative spectra $E_u(k)/u'^2$ for 6pos5 at y/δ = 0.8

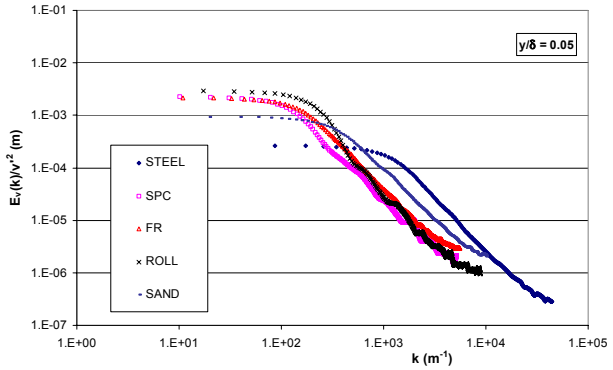

Figure D.108. Comparative spectra $E_v(k)/v'^2$ for 6pos5 at y/δ = 0.05

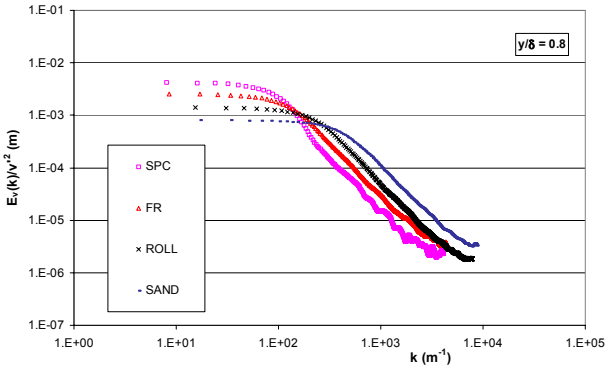

Figure D.109. Comparative spectra $E_v(k)/v'^2$ for 6pos5 at y/δ = 0.8

Appendix E. Roughness definitions and profiles

This Appendix to Chapter 6 presents in Section E.1 the definitions of the roughness parameters calculated by the UBM analysis software. The only one of these parameters which was ultimately retained was the Fractal Dimension FD. Section E.2 contains details on the analysis of the roughness characteristics with the UBM software provided with the optical measurement system, while Section E.3 graphically presents the roughness profiles of the analysed surfaces described in Section 6.5.

E.1 UBM Roughness definitions

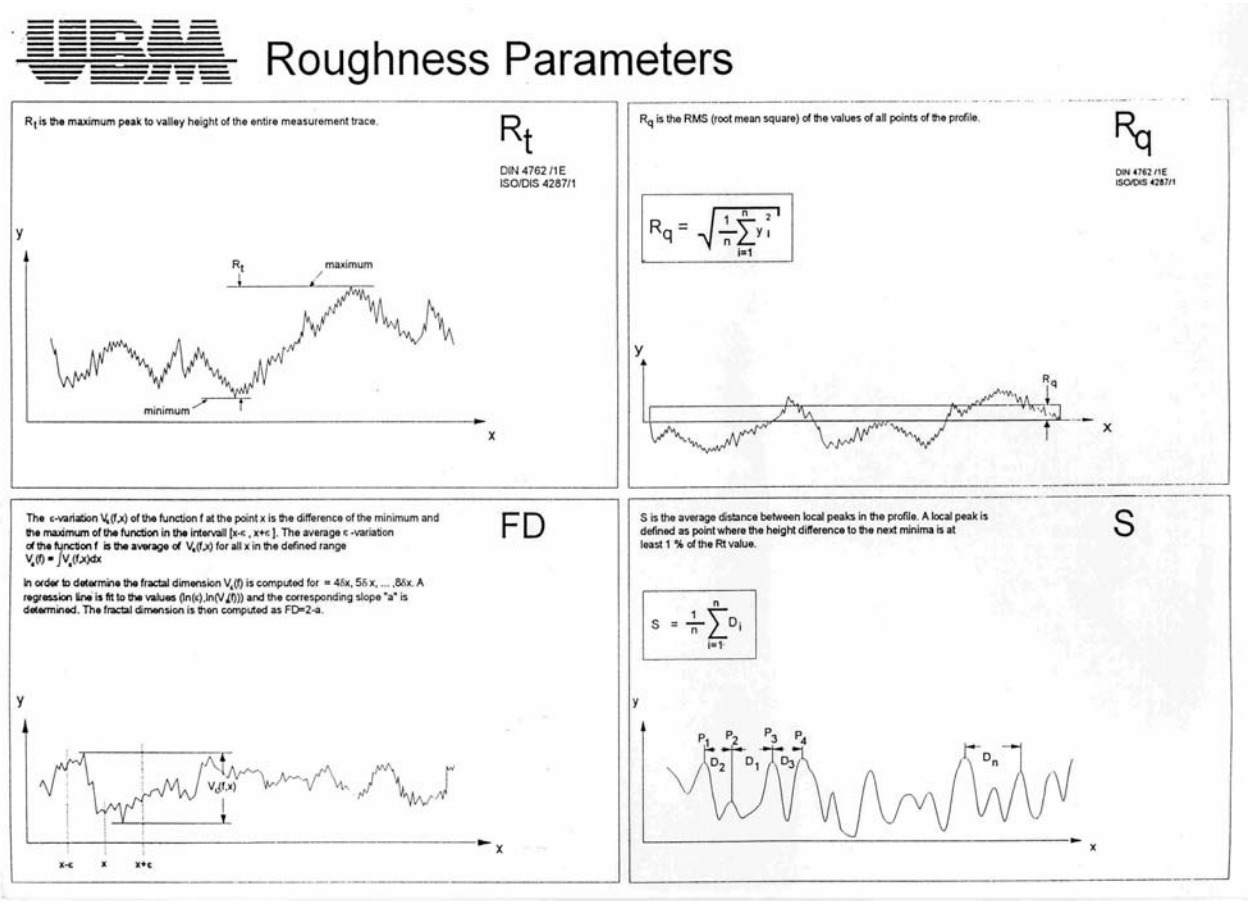

Roughness Parameters

R_p is the maximum distance between the highest profile point and the mean line of the profile after the profile has been filtered according to DIN 4768.

R_{pm} is the arithmetic average of the R_p values of 5 consecutive sections each of length lc of the entire measurement trace.

$$R_{pm} = \frac{1}{5}\sum_{i=1}^{5} R_{pi}$$

R_p

DIN 4762 /1E
ISO 4287 /1

R_{pm}

DIN 4762 /1E
ISO 4287 /1

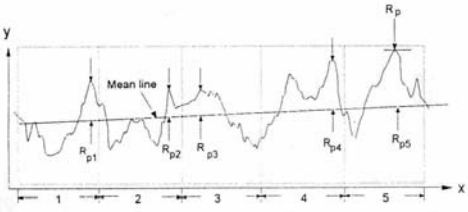

R_{3z} is the arithmetic average of the 5 single roughness depths R_{3z1} to R_{3z5} while R_{3zi} is the average of the third highest peak to the third deepest valley in each evaluation section, i , of length lc

R_{3zm} is the largest R_{3zi} value encountered when determining R_{3z}

$$R_{3z} = \frac{1}{5}\sum_{i=1}^{5} R_{3zi}$$

R_{3z}

DB No. 31007
see also
DB No. 31110

R_{3zm}

DB No. 31007

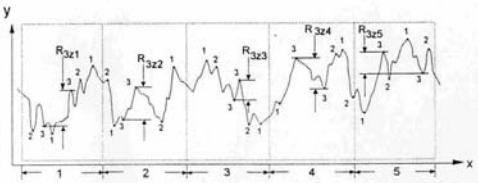

R_zISO is the maximum individual peak to valley height - and is the the arithmetic average of the 5 highest profile peaks and 5 lowest profile valleys over the entire (unfiltered) measurement trace. Peaks and valleys are defined as profile sections between two consecutive intersections with the centre line.
R_zISO is also called "ISO 10 Point Height"

$$R_z\text{ISO} = \frac{1}{5}\sum_{i=1}^{5} (\max_i + \min_i)$$

R_zISO

ISO 4287 /1

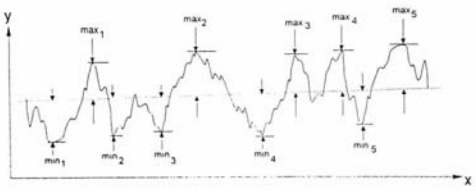

R_zDIN is the mean peak to valley height and is the arithmetic average of the maximum peak to valley height of the roughness values Y_1 to Y_5 of 5 consecutive sampling sections over the filtered profile. R_zDIN is also known as R_{tm}

R_{max} is the maximum individual roughness depth encountered as determining R_zDIN.

$$R_z\text{DIN} = \frac{1}{5}\sum_{i=1}^{5} Y_i$$

R_zDIN

DIN 4768 /1

R_{max}

DIN 4768 /1

R_{tm}

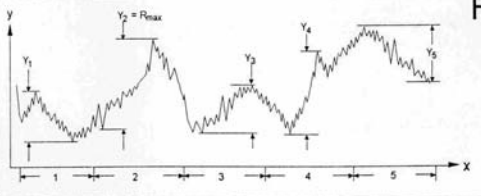

Roughness Parameters

S_k is the amplitude distribution skew - the skewness is 0 when the amplitude distribution is symetrical. If the skewness is not "0" the profile amplitudes as well as the amplitude density curve are assymetric, e.g. profile curves with "plateaus" and single deep valleys have a negative skew, profile curves with very intense peaks have a positive skew.

$$S_K = \frac{1}{n}\sum_{i=1}^{n} z_i^3 / R_q^3$$

S_k

DIN 4762 /1E
ISO/DIS 4287/1

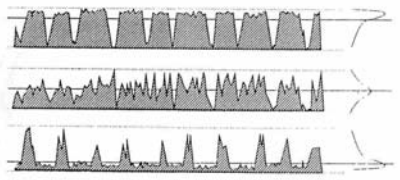

The curtosis is the comparison of the profile curve with a Gaussian amplitude and characterises the density as "smooth" or "with peaks". The Gaussian amplitude density curve has a curtosis of K = 3, smoother profile curves have K < 3, steeper curves have K > 3.

$$K = \frac{1}{n}\sum_{i=1}^{n} z_i^4 / R_q^4$$

K

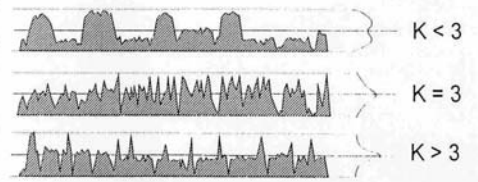

s-St is the arithmetic average of the profile slope distribution.

$$s\text{-}St = \frac{1}{n-2}\sum_{i=2}^{n-1}\left(\frac{z_{i+1} - z_{i-1}}{2\delta x} \cdot \frac{z_n - z_1}{(n-1)\delta x}\right)^2$$

s - St

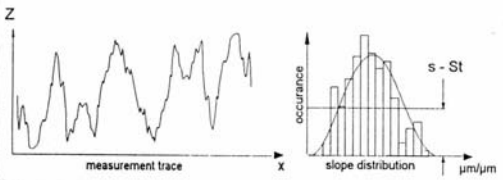

W_t is the maximum height between the peaks and valleys of the low-pass filtered profile.

P_t is the maximum profile depth - distance between two parallel lines in which the un-filtered (but levelled) profile line fits.

W_t

DIN 4774

P_t

DIN 4771

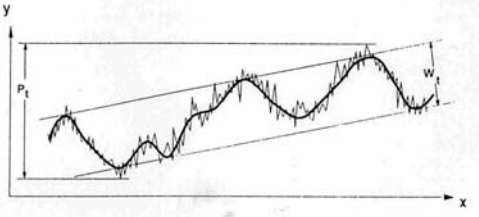

Roughness Parameters

S_m

DIN 4762 /1E
ISO 4287 /1

S_m is the arithmetic average spacing between the falling flanks of peaks on the mean line, over the asessment length. The profile peaks must exceed a defined threshold to be recognised.

$$S_m = \frac{1}{n}\sum_{i=1}^{n} S_i$$

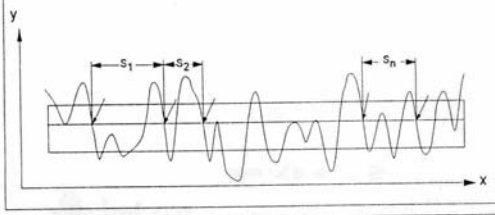

R_a

DIN 4768 /1
ISO/DIS 4287 /1

Y_{mean}

R_a is the arithmetic average of the absolute values of all points of the profile and can be understood as the height of the rectangle with the same length and surface as the profile encloses with the centre line. R_a is also known as CLA (centre line average height) or AA (arithmetical average).
Y mean is the arithmetic average of all points in the roughness filtered profile.

$$R_a = \frac{1}{n}\sum_{i=1}^{n} |y_i| \qquad Y_{mean} = \frac{1}{n}\sum_{i=1}^{n} y_i$$

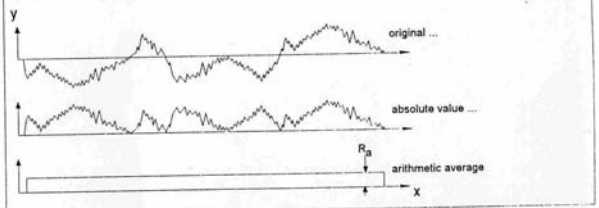

D

DIN 4762 /1E
ISO / DIS 4287 /1

N_r

D is the profile peak density, that is the number of profile peaks which cut two user defined tolerance lines parallel to the mean line once. C_1 is the upper, C_2 the lower counting limit.

N_r is the standarized peak count with the same criteria as for D except that the profile length is standarised to 10 mm.

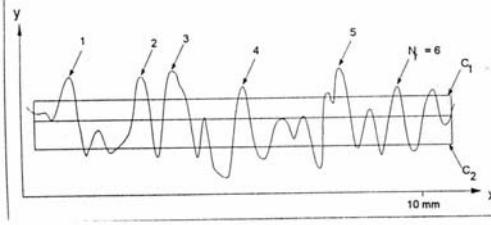

L_o

l_r

DIN 4762/1E
ISO/DIS 4287/1
(Lo is also known as lmo - and lr is known as lo)

L_o is the length of the of the profile after levelling all peaks and valleys of the measurement trace to a straight line.

l_r is the relation of the "stretched" length of the profile L_o to the actual length L_m

$$l_r = \frac{L_o}{L_m}$$

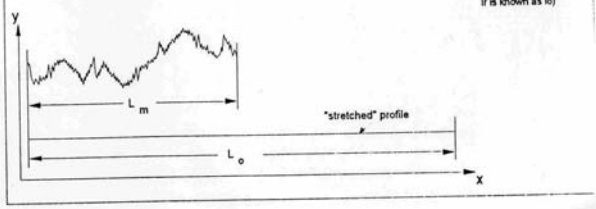

E.2 (Pre-)Analysis with the UBM software

This Section presents details on the analysis carried out with the UBM software provided with the optical measurement system prior to the analysis methodology described in Section 6.4. This analysis was only carried out for the STEEL, SPC, FR, ROLL, SPFR and SPSPC surfaces (cf. Section 6.3.2). Carrying out the analysis with the UBM software was potentially time-saving since measurement, filtering and analysis could be conducted uninterrupted and at the same PC. However, it turned out that additional parameters were required to compare the results with published data (cf. Section 6.5.4) so that a different analysis methodology (cf Section 6.4) was employed for the results given in Section 6.5.

E.2.1 Procedure

As described in Section 6.3.3, 6 measurements were taken for each surface. The results were then filtered (explained below) and the roughness parameters were calculated by the software. It was observed that the software put the cut-off length L_c at $1/7^{th}$ of the selected evaluation length L. In order to allow direct comparison with published data (i.e. Medhurst, 1989 and Dey, 1989), the cut-off length would have to be 50, 25, 10, 5 or 2.5mm (of these, Whitehouse (1994) notes that only 2.5mm is a British Standard sampling interval). The maximum evaluation length of the optical measurement system is 100mm, thus evaluation lengths of 70, 35 and 17.5 mm were selected for further analysis.

The sample interval is equal to half the short wavelength cut-off length and, has a direct influence on the parameters (cf. Section 6.4). In order to compare with the published data, a sampling interval of 50μm (or 20 samples/mm) was taken. In order to investigate the influence of the sampling interval, measurements with a sampling interval of 20 and 100μm were also taken. Initially measurements were also taken at sampling intervals of 10 and 5μm, but these were not retained for further analysis.

Since it was not possible to select the cut-off length independently from the evaluation length, 36 measurements (18 longitudinally followed by 18 transversally) were thus carried out for each surface. In the analysis methodology described in Section 6.4, the roughness parameters can be calculated for several cut-off lengths from a single digitally stored roughness profile. As mentioned in Section 6.3.3, the measurements were characterised by specifying the cut-off length in mm and the sampling interval in μm respectively, e.g. 5/50.

When the optical measurement system had finished the measurements over the traverse length, a typical plot like Figure E.1 would be displayed. Figure E.1 shows that the mean level is not zero, but varies over the traverse length, indicating either curvature of the plate or change in thickness of the coating. With the UBM software it is possible to select an unspecified filter, a polynomial of chosen order or a best-fit least-squares regression line. A polynomial of the 16th degree was initially selected to approximate the mean level. Figure E.2 shows the resulting roughness profile after levelling out, and the calculated roughness height parameters.

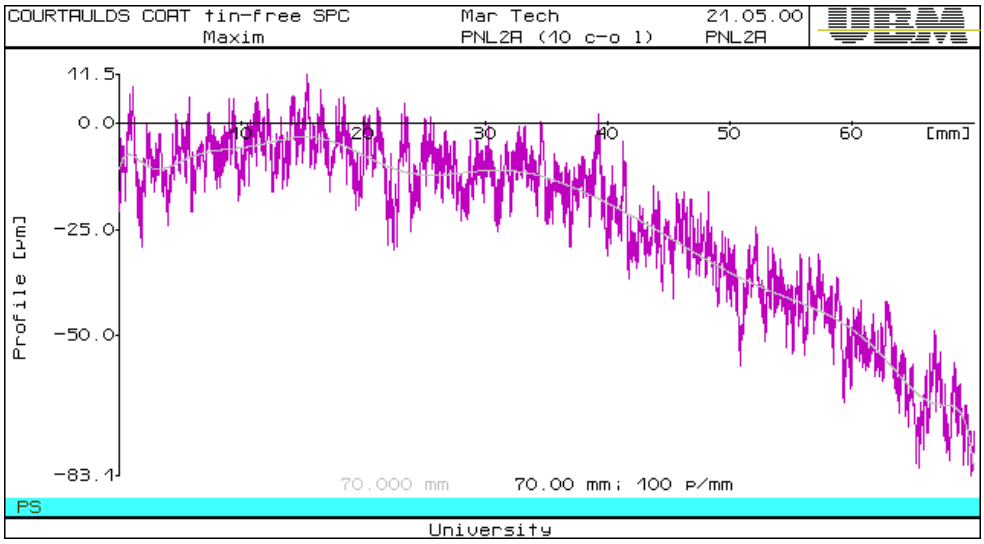

Figure E.1. Typical measured roughness profile (SPC surface), unlevelled, levelling polynomial shown.

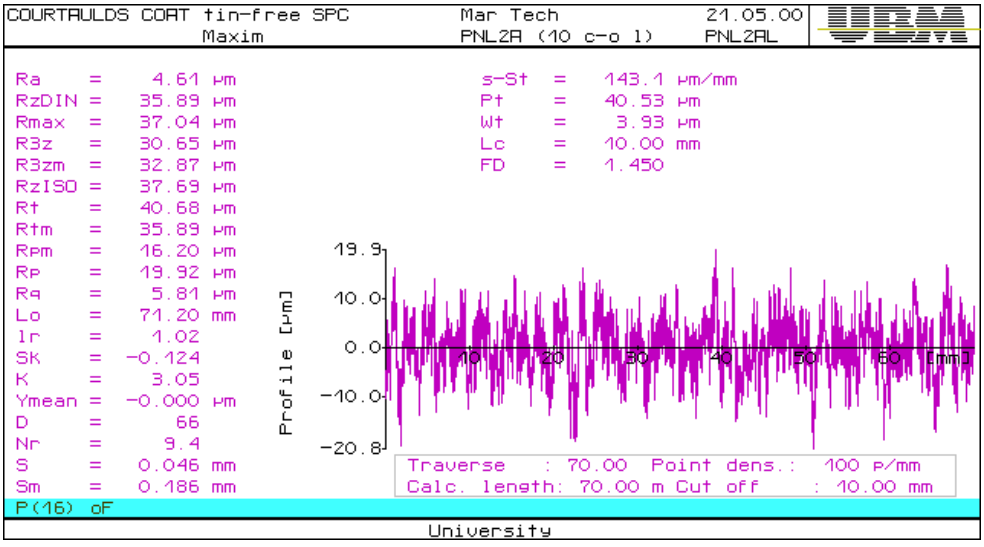

Figure E.2. Typical levelled roughness profile and displayed parameters (SPC surface).

A polynomial of 16th order seems extravagant. Whitehouse (1994, p. 25) points out that the polynomial should be made to match the geometry of the profile. On the other hand,

Bendat and Piersol (2000) recommend that the order of the polynomial for trend removal should be equal to or less than 3, in order to prevent loss of information on low frequency information, i.e. a polynomial of higher order would tend to filter out long-wavelength characteristics. Polynomials of various orders were therefore tried, including one of first order which is a least-squares regresssion line. In some cases, clearly unrealistic results were obtained with a simple regression line. Analysis of the sample STEEL surface indicated that the sample plate exhibited curvature, so that a regression line that only considers a tilt between the optical instrument and the sample plate, does not give satisfactory results. Even a second order polynomial did not always seem to model the curvature adequately, nor did a third order polynomial. It was found that a polynomial of order 4 was in general satisfactory for the STEEL surface, whereas for the SPC an order of 8 to 9 seemed appropriate. A higher order seems logical if on top of the waviness of the plate, a variation of the coating thickness is superimposed. The Foul Release surface seemed to require a still higher order and therefore an order of 16 was initially selected for all surfaces. However, such a high order seems uncommon in literature and a temporary, but unsatisfactory, choice was to apply a best-fit least-squares regression line.

Figure E.2 also shows the roughness parameters that were calculated by the software. One notices immediately that certain parameters mentioned in Section 6.2 are missing. For spectral analysis, a different software subroutine had to be employed that calculated the power spectrum using a Fast-Fourier Transform (FFT). Unfortunately, as Figure E.3 demonstrates, the power spectrum was then only displayed graphically and no further parameters, such as the important spectral moments, were returned. Once the power spectrum was calculated, the software could also compute the ACF, which would be displayed graphically along with the correlation length, $\tau_{0.1}$, as shown in Figure E.4.

A comparison was made for the roughness parameters for the longitudinal measurements using a regression line and a second-order polynomial respectively. Except for Sa, De and FD (and related parameters), all parameters changed significantly. The amplitude parameters decreased, Dz considerably increased and the height distribution became considerably more leptokurtic (i.e. exhibiting higher kurtosis).

The UBM software also provided an additional filter for the roughness parameters, but it was not specified in the manual. Comparison with a 16^{th} order polynomial showed good agreement but it is not clear whether the filter incorporated in the software was a higher-order polynomial or for example a moving average.

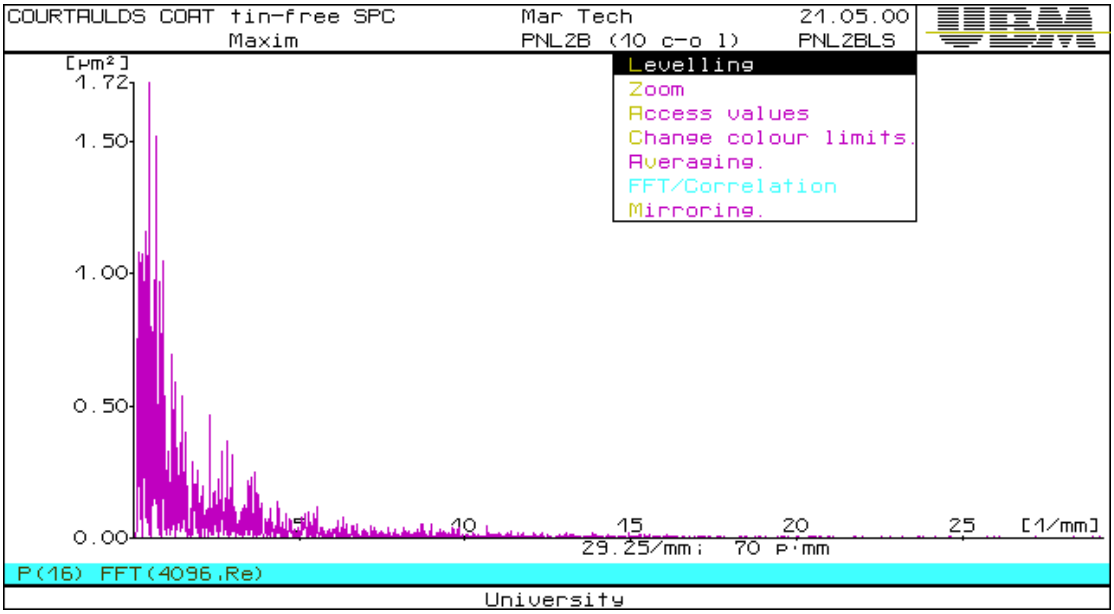

Figure E.3. Typical power spectrum for the SPC surface.

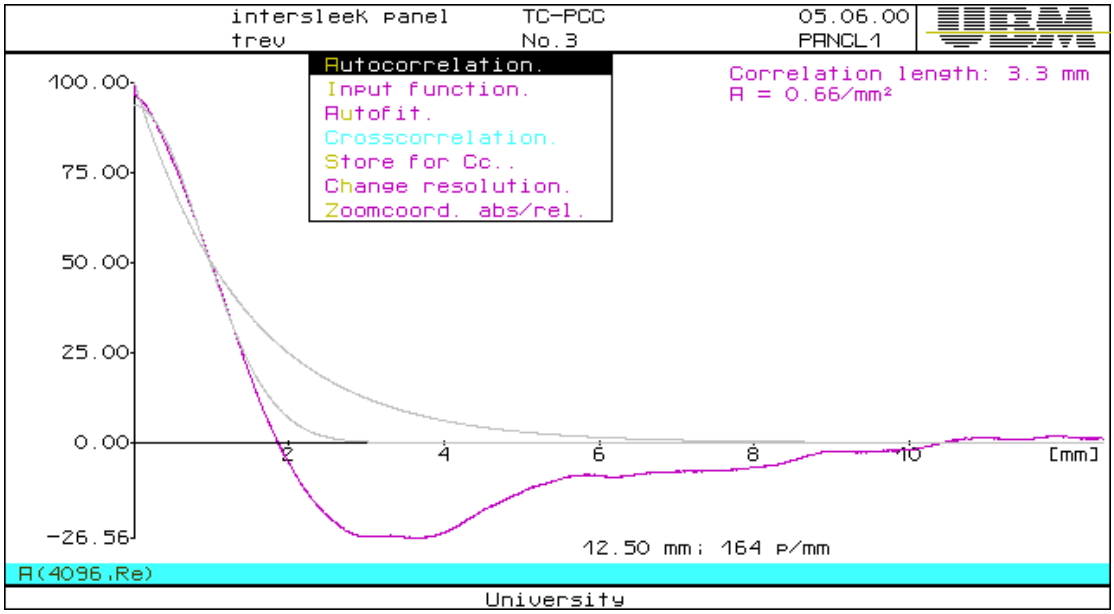

Figure E.4. Typical autocorrelation function and correlation length for the Foul Release surface.

E.2.2 Evaluation of the parameters as calculated by the UBM software

The information provided with the UBM software is minimal (cf Section E.1) and quite a lot of time was spent on verifying the calculated parameters by manually repeating the calculations.

After the results had been stored on disk, the digital roughness profiles were saved in ASCII format for further reference. The stored roughness parameters obtained with the UBM

software were put in a spreadsheet where averages over the 6 measurements were taken for each of the six sets of bandwidth limits.

A number of additional parameters were calculated in spreadsheets from the parameters calculated by the UBM software: Sq, De and Dz. *s –St*, as calculated by the software, is the arithmetic average of the profile slope distribution (in μm/mm), and Sq (in degrees) was calculated as $\tan^{-1}((s\text{-}St)/1000)$ multiplied by $180/\pi$.

With the UBM software, it was not possible to calculate the bandwidth parameter α via the spectral moments. Therefore the relationship established by Longuet-Higgins (1957) which uses the peak and zero-crossings densities: $\alpha(1) = (De/Dz)^2$ was employed. In addition, α, denoted by $\alpha(2)$, was calculated using the fractal approach with the values of FD, ω_L and ω_h (cf. Equation 6.12).

Tables E-1 to E-4 present the average roughness parameters for each of the different surfaces. In italics are the actual averages of the individual values of $\alpha(1)$. As $\alpha(1)$ is very sensitive to the small values of Dz that occur on the Foul Release surfaces, α can get very large (of order 10^4) which obviously makes the averages and standard deviations very large. In normal font $\alpha(1) = (De_{AV}/Dz_{AV})^2$ is listed.

The computations of the software were checked with calculations made in separate spreadsheet in which the formulae used by Medhurst (1989) and Dey (1989) were incorporated and it was found that there was a serious disagreement with the parameters calculated by the UBM software. The cut-off length L_c turned out to be equal to the traverse length L. For example, Rt was simply the maximum minus the minimum over the entire evaluation length. This implied that all measurements were effectively carried out for the cut –off lengths of 70, 35 and 17.5mm. It is not clear why the software insists on printing the cut-off length as $1/7^{th}$ of the traverse length. The matter was not further investigated (i.e. by contacting the manufacturers) since it quickly became clear that a different analysis would be required in order to be able to compare the results with the data collected by Dey (1989).

The formulae used by the software were correct (for a cut-off length equal to the traverse length) for the parameters Ra, Rq, Rt, s-St and Sq. The formulae for Sk and Ku differed slightly from Dey's but were comparable. Dz had to be multiplied by two, and De was smaller in value because of the definition of *local peaks* (cf. Section E.1). Rz was not calculated manually. An estimation of FD using the method described by Stemp and Stemp (2000) indicated that the values seem accurate.

Table E-1. Average roughness parameters of the mild steel surface (STEEL)

	70/50	35/50	17.5/50	35/100	70/20	17.5/20
Ra	6.77	1.97	1.32	1.97	6.76	1.34
Rq	7.93	2.49	1.72	2.42	7.94	1.76
Rt	40.79	21.12	14.34	16.12	38.35	15.88
Rz	32.97	14.22	9.34	11.86	34.25	10.91
Sk	-0.07	0.33	0.28	-0.01	-0.08	0.41
Ku	2.24	7.35	8.35	3.85	2.23	9.93
s-St	22.62	22.71	22.79	10.95	50.91	52.34
Sq	1.30	1.30	1.31	0.63	2.91	3.00
S	0.15	0.15	0.16	0.31	0.06	0.06
De	6.52	6.52	6.19	3.25	15.55	15.51
D	47.00	90.17	69.17	47.00	99.50	151.17
Dz	1.34	5.15	7.90	2.69	2.84	17.28
$\alpha(1)$	47.99	2.42	0.62	2.37	52.15	0.81
FD	1.66	1.66	1.68	1.68	1.64	1.65
$\alpha(2)$	17.91	11.06	6.75	6.76	36.64	13.07
$\tau_{0.1}$	15.10	0.95	0.09	-	0.09	0.04

Table E-2. Average roughness parameters of the SPC surface (SPC)

	70/50	35/50	17.5/50	35/100	70/20	17.5/20
Ra	11.16	7.45	5.14	7.43	11.19	5.21
Rq	13.50	9.10	6.35	9.08	13.54	6.44
Rt	73.21	47.96	34.32	44.71	76.03	38.44
Rz	64.46	42.64	28.75	39.66	69.37	31.71
Sk	0.13	-0.13	-0.16	-0.13	0.14	-0.11
Ku	3.07	2.65	2.85	2.62	3.11	2.97
s-St	47.02	47.11	45.40	27.98	83.65	82.96
Sq	2.69	2.70	2.60	1.60	4.78	4.74
S	0.18	0.18	0.18	0.35	0.08	0.08
De	5.47	5.53	5.63	2.89	12.11	12.02
D	57.50	41.17	29.50	26.00	89.83	48.00
Dz	1.64	2.35	3.37	1.49	2.57	5.49
$\alpha(1)$	16.21	8.65	3.55	4.49	38.76	5.92
FD	1.58	1.60	1.60	1.65	1.51	1.53
$\alpha(2)$	24.34	13.06	7.43	6.94	78.28	19.31
$\tau_{0.1}$	14.53	6.87	2.32	7.08	13.75	3.57

Table E-3. Average roughness parameters of the Foul Release surface (FR)

	70/50	35/50	17.5/50	35/100	70/20	17.5/20
Ra	6.37	5.13	2.93	5.11	6.40	2.95
Rq	7.75	6.19	3.58	6.17	7.86	3.60
Rt	34.35	26.05	15.93	25.27	35.59	17.58
Rz	32.67	24.22	13.92	22.43	34.37	15.10
Sk	0.02	0.13	-0.20	0.12	0.03	-0.17
Ku	2.54	2.69	2.90	2.64	2.55	2.92
s-St	6.33	6.12	6.49	4.20	14.75	15.30
Sq	0.36	0.35	0.37	0.24	0.85	0.88
S	0.17	0.17	0.17	0.42	0.06	0.06
De	6.00	6.03	5.90	2.44	16.05	16.26
D	15.83	10.83	6.83	6.67	40.00	15.00
Dz	0.45	0.62	0.78	0.38	1.14	1.71
$\alpha(1)$	177.78	94.59	57.21	41.23	198.22	90.42
	270.45	*409.76*	*179.03*	*185.40*	*335.79*	*268.07*
FD	1.29	1.29	1.31	1.20	1.50	1.51
$\alpha(2)$	62.78	23.19	8.33	6.19	82.51	20.61
$\tau_{0.1}$	13.55	8.25	4.48	8.25	12.78	5.50

Table E-4. Average roughness parameters of the rollered Foul Release surface (ROLL)

	70/50	35/50	17.5/50	35/100	70/20	17.5/20
Ra	8.89	7.42	5.39	7.44	8.88	5.40
Rq	11.71	9.77	6.90	9.78	11.69	6.88
Rt	81.56	56.11	33.82	54.52	85.03	34.47
Rz	56.64	40.80	25.84	36.80	64.19	29.12
Sk	0.49	0.22	0.09	0.21	0.51	0.03
Ku	212.15	3.99	6.53	3.91	6.77	6.23
s-St	16.01	14.69	13.02	11.15	25.68	23.24
Sq	0.92	0.84	0.75	0.64	1.47	1.33
S	0.19	0.20	0.19	0.53	0.06	0.06
De	5.30	5.08	5.49	1.97	15.65	15.78
D	14.83	7.50	6.17	5.33	30.83	12.83
Dz	0.42	0.43	0.70	0.30	0.88	1.47
$\alpha(1)$	159.24	139.57	61.51	43.12	316.27	115.23
	241.47	*615.72*	*485.28*	*360.70*	*447.16*	*565.35*
FD	1.16	1.18	1.21	1.13	1.34	1.40
$\alpha(2)$	58.09	18.70	6.93	4.48	194.96	25.20
$\tau_{0.1}$	9.13	5.73	14.53	5.75	7.47	4.22

Table E-5. Average roughness parameters of the SPSPC surface

	70/50	35/50	17.5/50	35/100	70/20
Ra	6.79±0.69	5.69±0.58	4.62±0.31	5.59±0.54	6.82±0.71
Rq	8.45±0.78	7.07±0.74	5.77±0.36	6.97±0.72	8.51±0.81
Rt	50.00±4.78	40.91±4.42	33.61±3.75	40.38±3.79	56.11±10.12
Rz	45.65±3.51	36.32±3.40	27.73±1.23	33.79±3.55	49.48±4.61
Sk	0.00±0.32	-0.09±0.16	0.07±0.10	-0.10±0.16	0.01±0.34
Ku	2.86±0.27	2.82±0.18	2.89±0.26	2.88±0.17	2.96±0.36
s-St	56.49±0.73	55.81±2.01	55.38±1.64	34.14±1.89	99.84±3.97
Sa	3.23±0.04	3.19±0.11	3.17±0.09	1.96±0.11	5.70±0.22
S	0.19±0.00	0.18±0.00	0.19±0.01	0.31±0.13	0.08±0.00
De	5.27±0.13	5.42±0.11	5.28±0.18	5.73±7.19	12.27±0.26
D	112.17±15.17	64.17±7.57	38.33±5.82	44.17±5.27	180.00±21.84
Dz	3.20±0.43	3.67±0.43	4.38±0.67	2.52±0.30	5.14±0.62
α(1)	2.84±0.85	2.29±0.73	1.54±0.46	12.07±26.37	5.91±1.44
FD	1.57±0.02	1.57±0.03	1.57±0.02	1.64±0.02	1.48±0.01
α(2)	24.94±2.04	13.92±1.10	7.64±0.15	7.02±0.14	93.74±3.56

Table E-6. Average roughness parameters of the SPFR surface

	70/50	35/50	17.5/50	35/100	70/20
Ra	8.77±2.75	3.62±1.24	2.00±0.65	3.64±1.22	8.81±2.74
Rq	10.14±3.14	4.34±1.24	2.29±0.70	4.35±1.22	10.18±3.14
Rt	37.31±11.58	19.59±4.90	9.49±2.71	16.57±5.88	40.08±9.98
Rz	35.58±11.62	17.20±4.34	8.21±2.09	14.84±3.47	36.95±11.66
Sk	0.31±0.28	0.18±0.74	0.24±0.34	0.17±0.74	0.33±0.27
Ku	1.98±0.24	2.80±1.22	2.10±0.73	2.73±1.24	2.04±0.30
s-St	6.18±1.30	5.96±2.34	5.20±1.14	2.85±0.62	15.09±4.38
Sa	0.35±0.07	0.34±0.13	0.30±0.07	0.16±0.04	0.86±0.25
S	0.15±0.00	0.16±0.00	0.15±0.00	0.33±0.03	0.06±0.00
De	6.48±0.20	6.40±0.19	6.50±0.18	3.00±0.24	16.44±0.32
D	8.00±5.37	10.83±7.28	5.33±3.67	5.17±4.02	17.17±10.68
Dz	0.23±0.15	0.62±0.42	0.61±0.42	0.30±0.23	0.49±0.31
α(1)	803.15 *10051±21132*	106.93 *661±1230*	113.89 *290±263*	263.44 *645±1068*	1123.96 *4785±7580*
FD	1.39±0.04	1.41±0.04	1.42±0.07	1.24±0.04	1.55±0.02
α(2)	49.34±6.12	20.46±1.35	8.79±0.32	8.10±0.79	62.81±7.03

Because of the differences in bandwidth limits, filtering techniques and calculation methods, the data shown in Tables 6-1 to 6-4 could not be used for comparison with the surfaces analysed by Dey (1989) for which re-analysis of the data was required.

However, as explained in Section 6.4.1, by using a moving average filter in Section 6.4, only bandwidth limits 5/50 and 2.5/50 could be retained. For this reason, the opportunity was

taken to use the data of Tables 6-1 to 6-4 to investigate the influence of the bandwidth limits on the roughness parameters.

E.2.3 Influence of the bandwidth limits

One immediate observation from Tables E-1 to E-4, is that the longer the cut-off length L_c, the larger the height parameters. This is one property of self-affine fractals, which implies that that the numerical value of any parameter which depends on the amplitude of the profile, is dominated by the longest wavelengths present (Thomas, 1999, p. 117). Thomas (1999, p. 125) states that the parameters often increase with the square root of the cut-off length. If one takes into account, that the cut-off lengths differ by a factor 2, one notices indeed that most of the height parameters increase by a factor 1.41. For quick-reference, one can check whether the values at 70/50 are approximately twice the values at 17.5/50. All surfaces follow this increase quite well, except the steel surface which exhibits a higher increase when the cut-off length increases from 35 to 70mm.

The influence of the sampling interval on the height parameters is (as can be expected) restricted to the extreme-value parameters Rt and Rz, and is marginal.

Sk and Ku vary with the cut-off length, but do not seem to vary with the sampling length. Spurious peak values can have a large influence because the average is taken over a relatively small amount of values.

In contrast, s-St and thus Sq, do not vary significantly with the cut-off length, but with the sampling interval as is expected and mentioned in Section 6.2.2.2.

The same observations are made for S and thus De, but the rate of increase, which again seems inversely proportional to the sampling length for the aluminium surface, is higher for the other surfaces. Dz varies both with the cut-off length and the sampling interval. Quite logically, the number of crossings with the mean level increases as the cut-off length increases and the sampling length decreases.

$\alpha(1) = (De/Dz)^2$ varies with both sampling and cut-off length in such a way that there is no clear trend. FD does not vary significantly with the cut-off length. Interestingly, the fractal dimension of the SPC surface increases moderately as the sampling length increases, but decreases for the Foul Release surfaces, and does not change for the steel surface. $\alpha(2)$ increases as the L_c increases and the sampling length decreases.

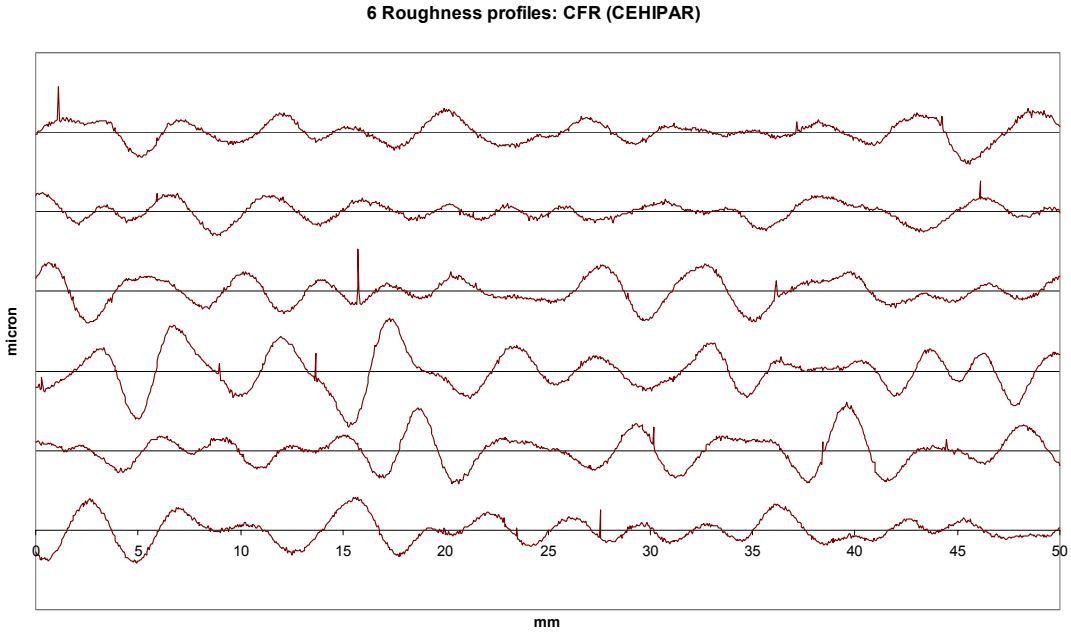

Figure E.7. CFR profiles

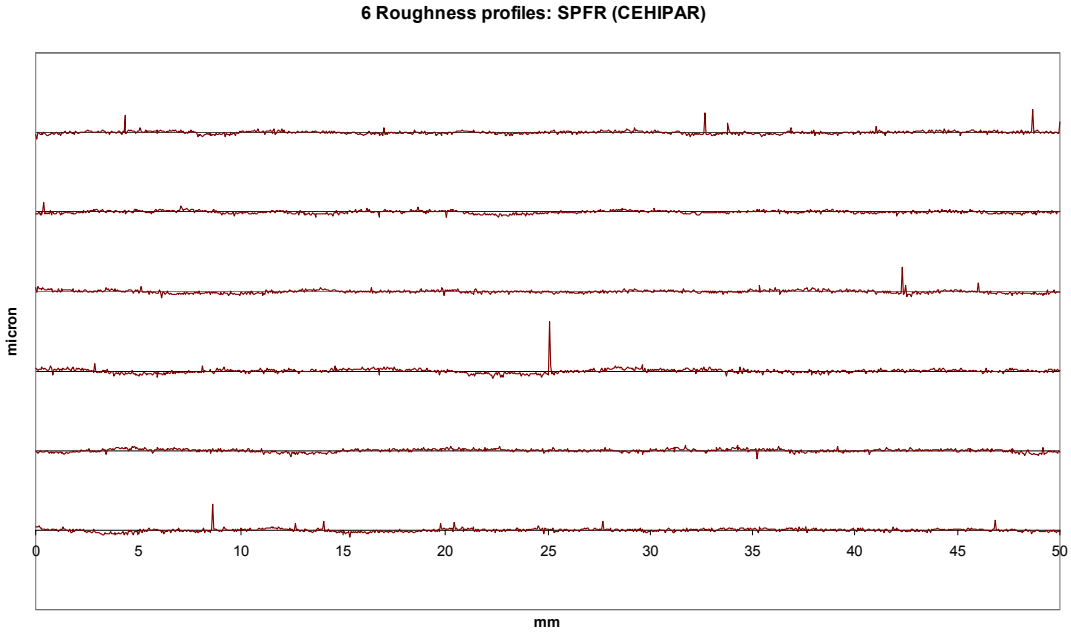

Figure E.8. SPFR profiles

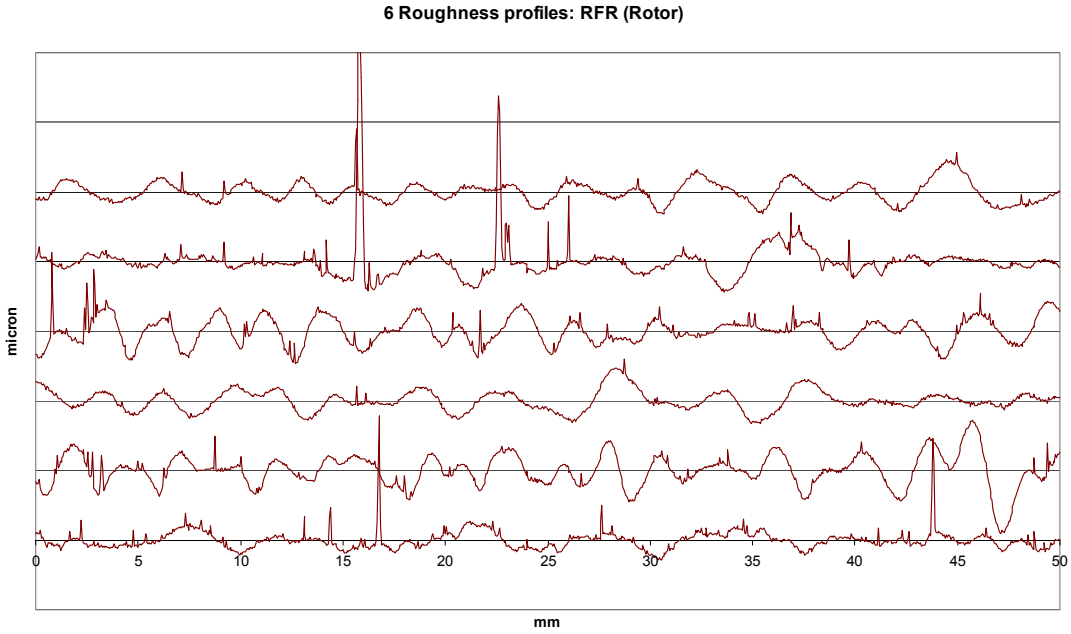

Figure E.9. RFR profiles

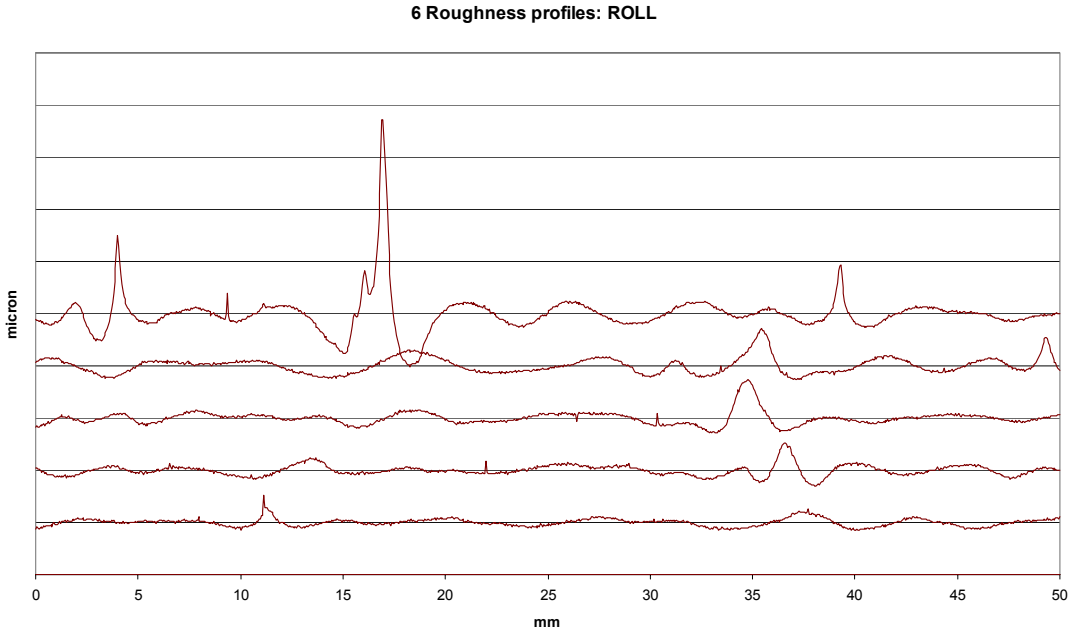

Figure E.10. ROLL profiles

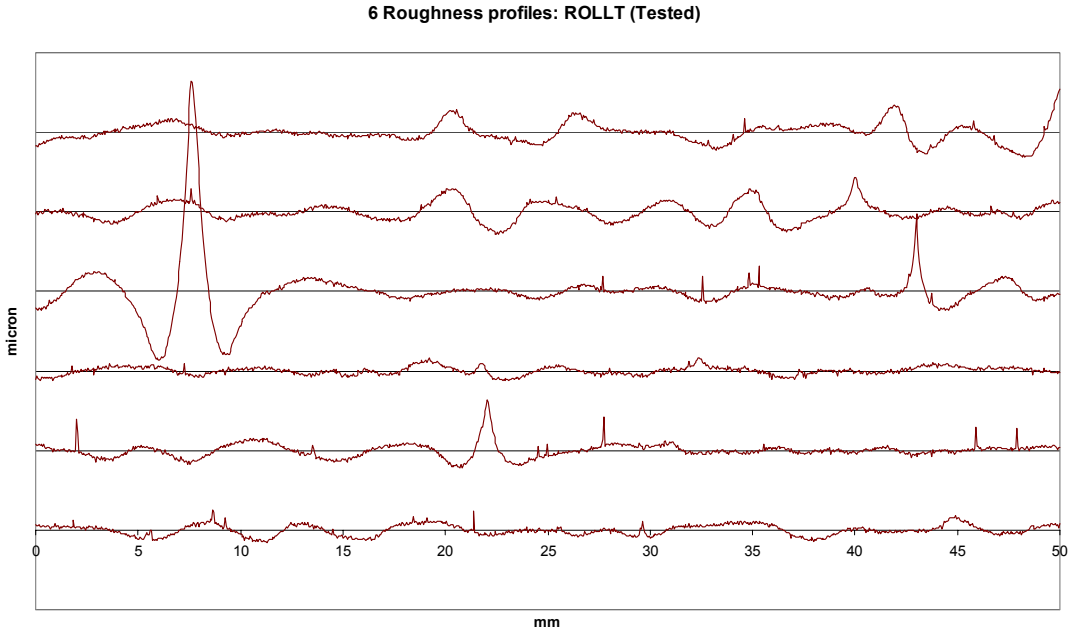

Figure E.11. ROLLT profiles

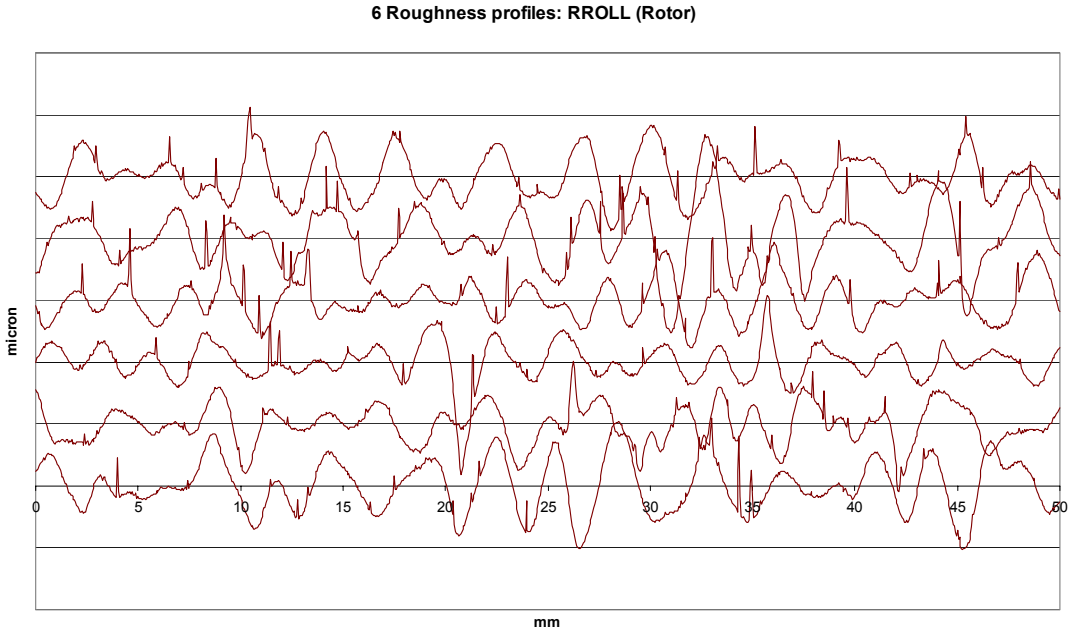

Figure E.12. RROLL profiles

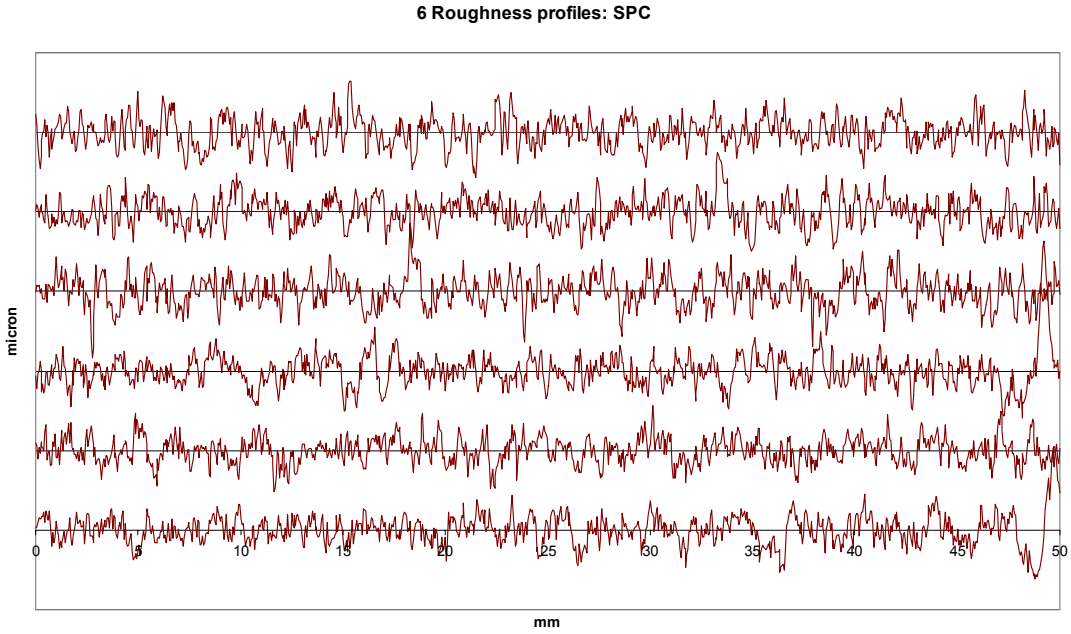

Figure E.13. SPC profiles

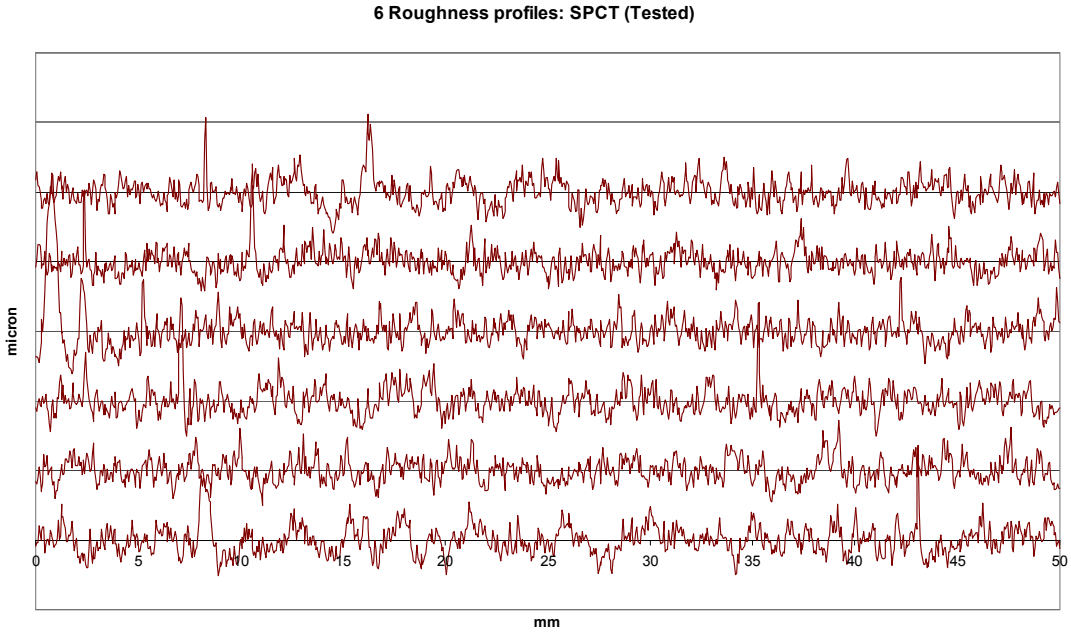

Figure E.14. SPCT profiles

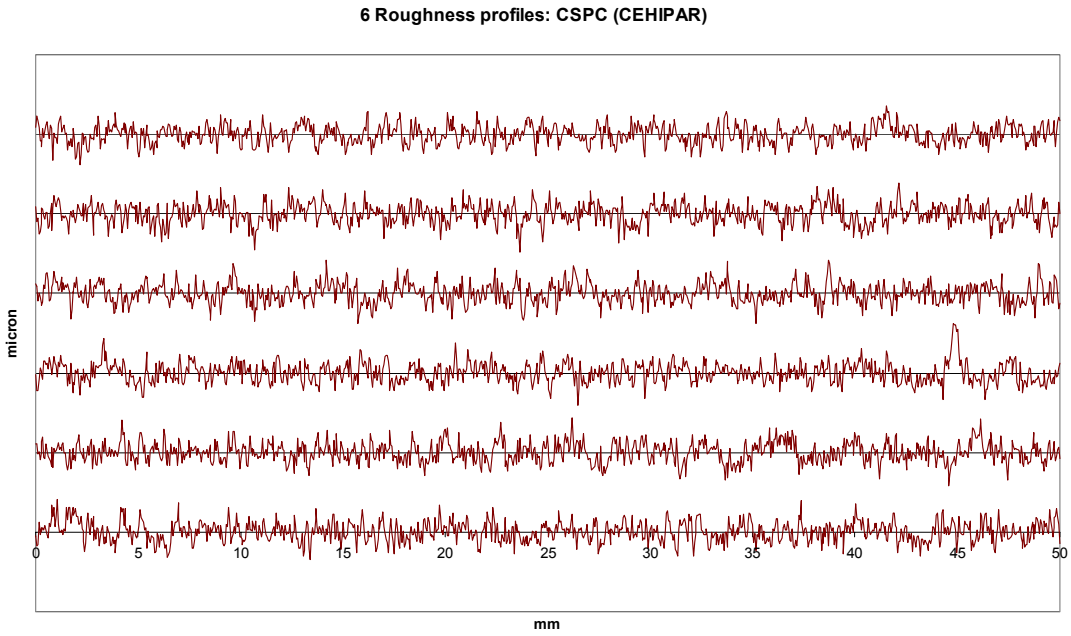

Figure E.15. CSPC profiles

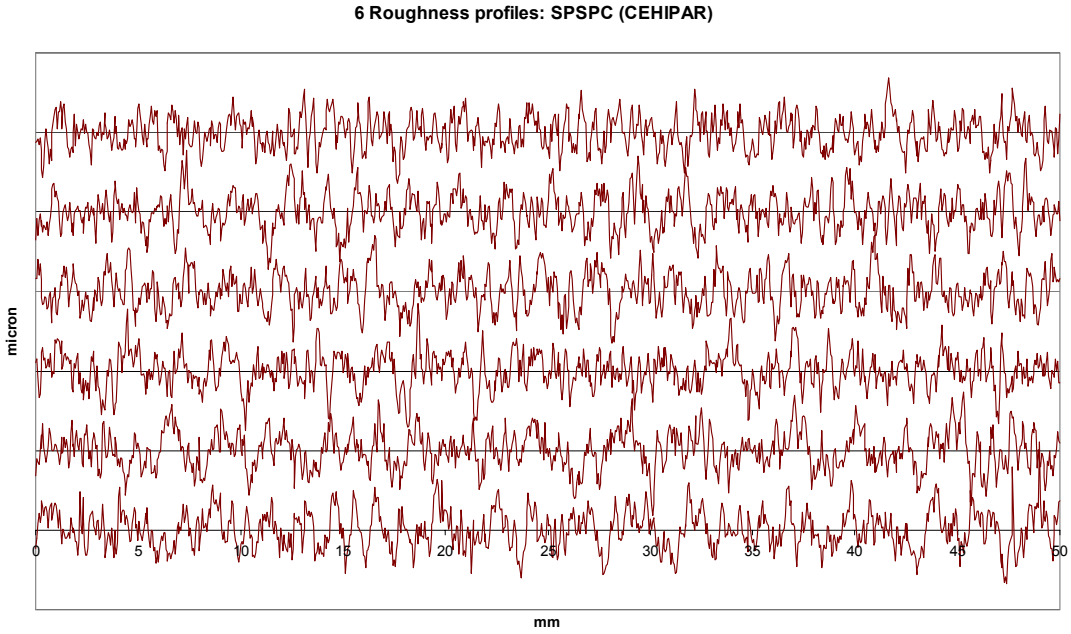

Figure E.16. SPSPC profiles

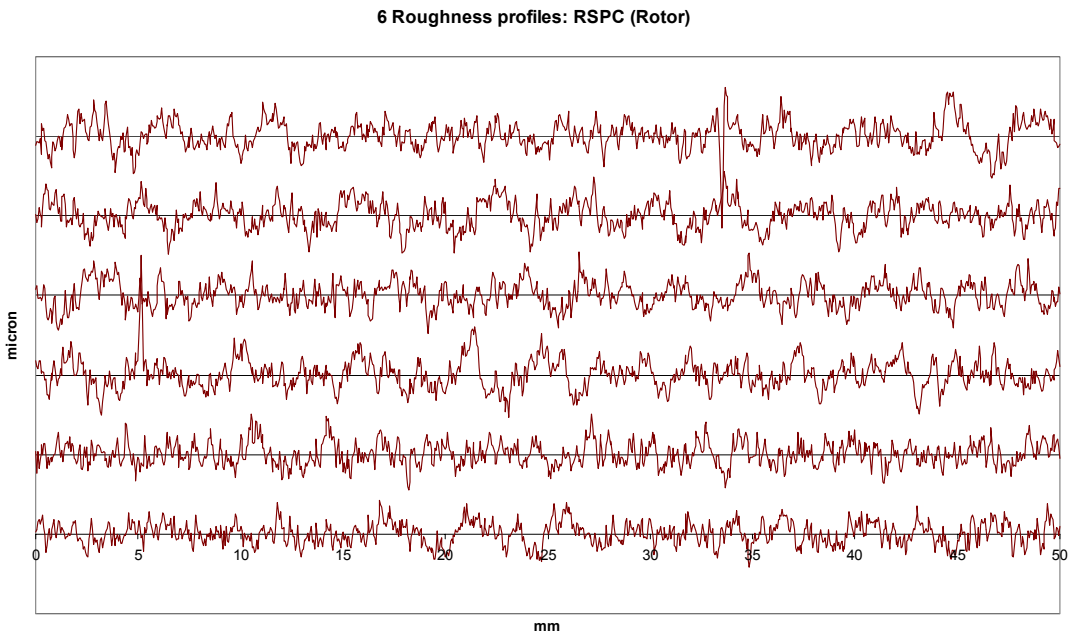

Figure E.17. RSPC profiles.

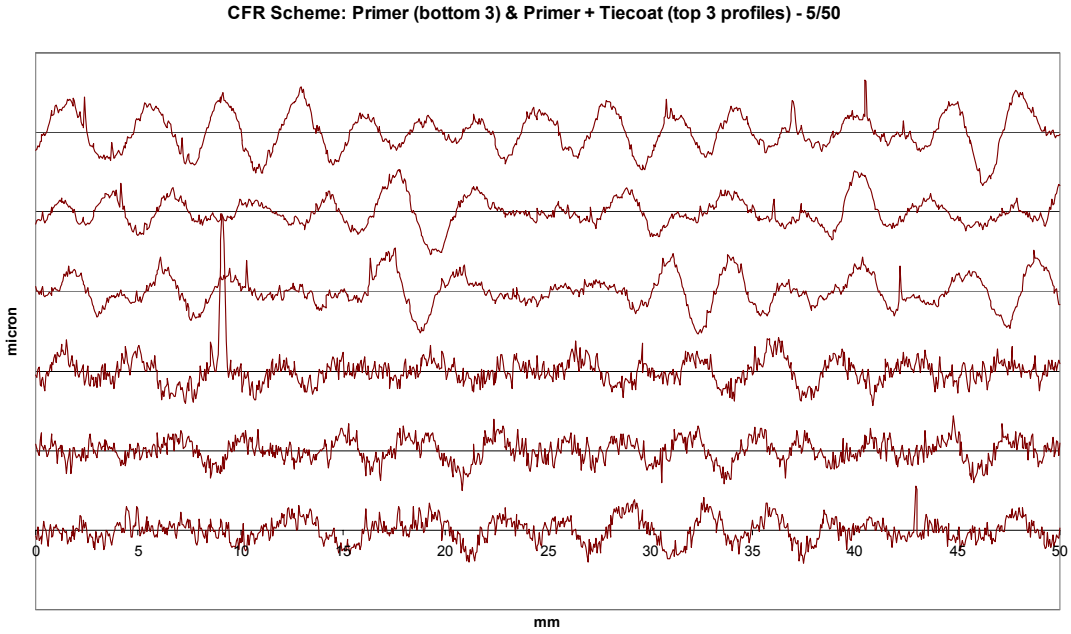

Figure E.18. Roughness profiles of the CFR scheme.

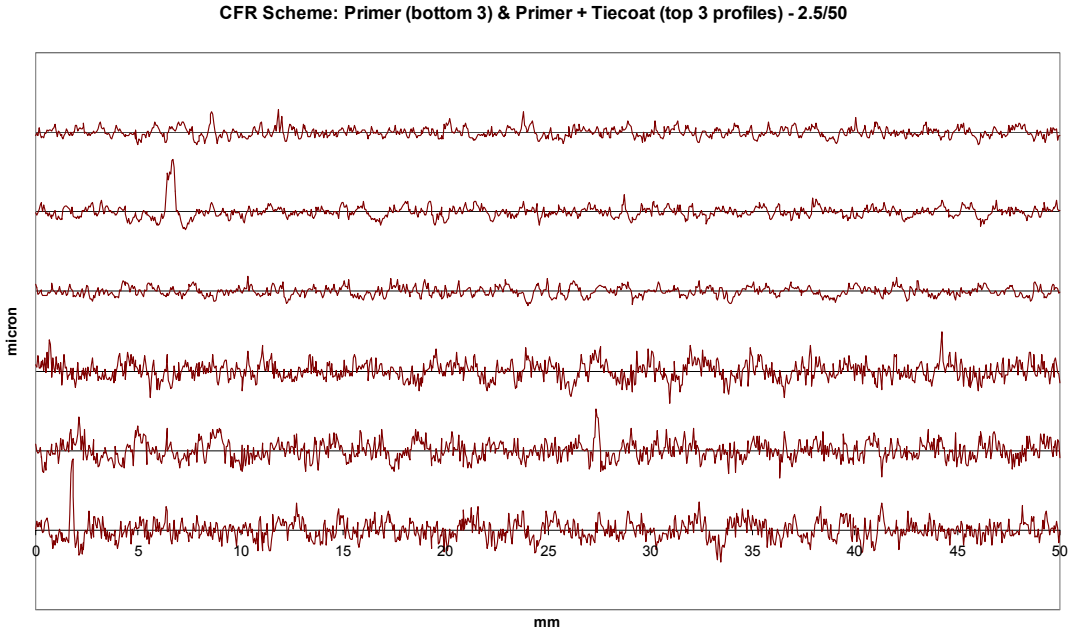

Figure E.19. Roughness profiles of the CSPC scheme.